Universidade de São Paulo
Instituto de Física

# Controles ambientais sobre a convecção isolada na Amazônia: um estudo observacional e de modelagem numérica

Leandro Alex Moreira Viscardi

Orientador: Prof. Dr. Henrique de Melo Jorge Barbosa

Tese de doutorado apresentada ao Instituto de Física da Universidade de São Paulo, como requisito parcial para a obtenção do título de Doutor em Ciências.

Banca Examinadora:

Prof. Dr. Henrique de Melo Jorge Barbosa - Orientador (IF-USP)
Prof. Dr. Alexandre Lima Correia (IF-USP)
Profa. Dra. Maria Assunção Faus da Silva Dias (IAG-USP)
Prof. Dr. Alan James Peixoto Calheiros (INPE)
Prof. Dr. Enver Manuel Amador Ramirez Gutierrez (INPE)

Henrique Barbosa

Digitally signed by Henrique Barbosa
Reason: I have reviewed this document
Location: Sao Paulo
Date: 2023.08.19 11:44:56 -04'00'

São Paulo
2023

# FICHA CATALOGRÁFICA
## Preparada pelo Serviço de Biblioteca e Informação do Instituto de Física da Universidade de São Paulo

Viscardi, Leandro Alex Moreira

Controles ambientais sobre a convecção isolada na Amazônia: um estudo observacional e de modelagem numérica. São Paulo, 2023.

Tese (Doutorado) - Universidade de São Paulo. Instituto de Física. Depto. Física Aplicada

Orientador: Prof. Dr. Henrique de Melo Jorge Barbosa

Área de Concentração: Física.

Unitermos: 1. Convecção tropical; 2. Transição da convecção rasa para profunda; 3. Controles ambientais; 4. Experimento GoAmazon2014/5; 5. Simulações de alta resolução.

USP/IF/SBI-052/2023

University of São Paulo
Institute of Physics

# Environmental controls on isolated convection in the Amazon: an observational and numerical modeling study

Leandro Alex Moreira Viscardi

Supervisor: Prof. Dr. Henrique de Melo Jorge Barbosa

Thesis submitted to the Institute of Physics of the University of São Paulo in partial fulfillment of the requirements for the degree of Doctor of Science.

Examining Committee:

Prof. Dr. Henrique de Melo Jorge Barbosa - Supervisor (IF-USP)
Prof. Dr. Alexandre Lima Correia (IF-USP)
Prof. Dr. Maria Assunção Faus da Silva Dias (IAG-USP)
Prof. Dr. Alan James Peixoto Calheiros (INPE)
Prof. Dr. Enver Manuel Amador Ramirez Gutierrez (INPE)

São Paulo
2023

# ACKNOWLEDGEMENTS

With immense gratitude, I acknowledge the University of São Paulo, Brazil, notably the São Carlos Institute of Physics and the Institute of Physics, where I dedicated a decade to pursuing my academic journey. During this time, I achieved a BSc in Physics (2016), an MSc in Physics (2019), and have now been granted a Ph.D. in Physics (2023). The professors and friends who accompanied me through this critical period of my life hold a special place in my heart. Their unwavering support, guidance, and companionship have left an indelible mark on my heart, and their influence continues to shape the person I am becoming.

I acknowledge the Brazilian National Council for Scientific and Technological Development (CNPq) for providing me with a graduate fellowship (grant number 148652/2019-0) that supported my doctoral studies at the University of São Paulo, Brazil.

I also acknowledge the Coordination for the Improvement of Higher Education Personnel (CAPES) fellowship (grant number 88887.571091/2020-00) provided under the Institutional Program for Internationalization (CAPES-PrInt). This esteemed fellowship supported my six-month sandwich doctorate at the University of Hawai’i at Mãnoa, United States, profoundly influencing the development of this project.

I want to convey my heartfelt appreciation to my supervisor, Dr. Henrique de Melo Jorge Barbosa, for having faith in my work and being the initial visionary behind this project, including the sandwich doctorate. While the course of scientific exploration often involves adapting and exploring multiple possibilities to approach each problem, my supervisor’s contribution remains indispensable. I am grateful for our regular meetings and the wealth of insightful discussions shared with Dr. Giuseppe Torri, which was an invaluable source of inspiration.

I would like to extend my profound gratitude to Dr. Giuseppe Torri, for his unforeseen and unwavering support for this project. Our bond grew stronger during my time in Hawaii, where I pursued my sandwich doctorate at the University of Hawai‘i at Mānoa under his guidance. Despite my return to Brazil, our collaboration has continued. Dr. Torri’s invaluable contributions have elevated the quality of this project and provided crucial support for its successful completion. It is worth highlighting that the modeling studies conducted were made possible by utilizing the computational resources of the University of Hawai‘i.

I want to express my gratitude to Dr. David K. Adams for his exceptional support and impactful suggestions that have greatly influenced this work. It is important to note that this research has been significantly inspired by his previous contributions on convection in the Amazon.

I also thank all my research colleagues who have engaged in numerous enriching conversations during my doctoral journey, both in person and virtually. I am grateful for the valuable interactions with colleagues from the University of São Paulo, the University of Hawaiʻi at Mãnoa, and the University of Maryland Baltimore County.

The technical support and advanced computing resources from University of Hawaiʻi Information Technology Services – Cyberinfrastructure, funded in part by the National Science Foundation CC* awards # 2201428 and # 2232862 are gratefully acknowledged.

This research also recognizes the data from the Atmospheric Radiation Measurement (ARM) Program sponsored by the U.S. Department of Energy, Office of Science, Office of Biological and Environmental Research, Climate and Environmental Sciences Division.

I also thank Marat Khairoutdinov for providing access to the System for Atmospheric Modeling (SAM) code and offering valuable assistance with the Surface Land Model.

Lastly, but certainly not least, I express my gratitude to my family for their unconditional support.

# ABSTRACT

VISCARDI, L. A. M. **Environmental controls on isolated convection in the Amazon: an observational and numerical modeling study**. 2023. 145p. Thesis (Doctor in Science) - Institute of Physics, University of São Paulo, São Paulo, 2023.

The Amazon rainforest is a vital component of the global climate system, playing a significant role in the hydrological and energy cycles. The intense convection in this region influences atmospheric circulation on a global scale and drives large-scale transports of energy and moisture, with implications for potential climate change pathways. Despite its importance, understanding and simulating the shallow-to-deep (STD) convective transition in this region has been a long-standing challenge. This is partially due to the wide range of spatial and temporal scales involved and the complexity of cloud physical processes and biosphere-atmosphere interactions. In this study, we combined recent observations and high-resolution simulations to evaluate the triggering mechanisms and assess the relative importance of different environmental controls on locally-driven convection in the Amazon.

Observationally, we evaluated the environmental conditions associated with shallow, congestus, and isolated deep convection days during the wet season (December to April), employing data from the GoAmazon (2014-2015) experiment. The deep regime is characterized by moister conditions in low levels during the morning and strong moisture convergence in the afternoon. In contrast, shallow and congestus days are drier and dominated by moisture divergence in the morning. The peak of precipitation associated with the STD transition occurs around 16-17 local standard time. Afternoon precipitation, on average, increases with integrated column water vapor, low-level wind shear, and convective available potential energy; but relatively higher values of these parameters do not necessarily guarantee that the STD transition will occur.

Numerically, we conducted simulations during the period of December 2014, utilizing large-scale forcing specifically developed for the GoAmazon2014/5 experiment. The model consistently reproduced the observations for precipitation, moisture, and surface fluxes of radiation, latent and sensible heat. Through sensitivity experiments, we examined the relative importance of moisture and vertical wind shear in controlling the STD convective transition. We found that deep convection in the Amazon region is highly sensitive to low-level environmental conditions. Notably, early morning low-level preconditioning is vital to daytime convection and precipitation. Only unrealistically dry conditions in the free troposphere effectively inhibit the development of deep convection. The large-scale field of vertical moisture advection strongly impacts the development of convection, which is indirectly linked to water vapor convergence. Low-level wind shear facilitates the STD transition under moderate strength, although it can still occur even in the absence of wind shear or under strong wind shear conditions. The upper-level wind shear negatively impacts high cloud formation, but this impact is relatively minor compared to that associated with low-level wind shear.

The synergy between observations and high-resolution simulations provided a comprehensive analysis with crucial quantitative information on the environmental controls of isolated convection. Our findings contribute to advancing our comprehension of tropical convection and provide valuable guidance for future research aimed at enhancing weather and climate models.

**Keywords**: Tropical convection. Shallow-to-deep convective transition. Environmental controls. GoAmazon2014/5 experiment. High-resolution simulations.

# RESUMO

VISCARDI, L. A. M. **Controles ambientais sobre a convecção isolada na Amazônia: um estudo observacional e de modelagem numérica**. 2023. 145p. Tese (Doutorado em Ciências) - Instituto de Física, Universidade de São Paulo, São Paulo, 2023.

A Floresta Amazônica é um componente vital do sistema climático global, desempenhando um papel significativo nos ciclos hidrológico e energético. A intensa convecção nesta região influencia a circulação atmosférica em escala global e impulsiona o transporte em grande escala de energia e umidade, com implicações para possíveis trajetórias de mudanças climáticas. Apesar de sua importância, entender e simular a transição da convecção rasa para profunda (STD, do inglês *shallow-to-deep*) nessa região tem sido um desafio de longa data. Isso se deve, em parte, à ampla variedade de escalas espaciais e temporais envolvidas e à complexidade dos processos físicos de nuvens e das interações entre a biosfera e a atmosfera. Neste estudo, combinamos observações recentes e simulações de alta resolução para avaliar os mecanismos desencadeadores e avaliar a importância relativa de diferentes controles ambientais na convecção que se desenvolve localmente na Amazônia.

Observacionalmente, avaliamos as condições ambientais associadas aos dias de convecção rasa, congestus e profunda isolada durante a estação chuvosa (dezembro a abril), utilizando dados do experimento GoAmazon (2014-2015). O regime de convecção profunda é caracterizado por condições mais úmidas em níveis baixos durante a manhã e forte convergência de umidade durante a tarde. Em contraste, os dias de convecção rasa e congestus são mais secos e dominados por divergência de umidade pela manhã. O pico de precipitação associado à transição STD ocorre em torno das 16-17 horas no horário local. A precipitação durante a tarde, em média, aumenta com o conteúdo de umidade integrada na coluna atmosférica, cisalhamento do vento em baixos níveis e energia potencial convectiva disponível; no entanto, valores relativamente mais altos dessas variáveis não necessariamente garantem que a transição STD ocorrerá.

Numericamente, realizamos simulações durante o período de dezembro de 2014, utilizando forçamento de grande escala desenvolvido especificamente para o experimento GoAmazon2014/5. O modelo reproduziu consistentemente as observações de precipitação, umidade e fluxos de radiação, calor latente e calor sensível na superfície. Através de experimentos de sensitividade, examinamos a importância relativa da umidade e do cisalhamento vertical do vento no controle da transição STD. Descobrimos que a convecção profunda na região da Amazônia é altamente sensível às condições ambientais de baixos níveis. Notavelmente, o precondicionamento de baixos níveis durante a manhã é fundamental para a convecção e a precipitação durante o dia. Apenas condições irrealisticamente secas na troposfera livre efetivamente inibem o desenvolvimento de convecção profunda. O campo de grande escala de advecção vertical de umidade tem um forte impacto no desenvolvimento da convecção, o que está indiretamente relacionado à convergência de vapor de água. O cisalhamento do vento em baixos níveis favorece o desenvolvimento da convecção durante a tarde em condições de intensidade moderada; no entanto, a transição STD pode ocorrer mesmo na ausência de cisalhamento do vento ou sob condições de forte cisalhamento do vento. O cisalhamento do vento em altos níveis afeta negativamente a formação de nuvens altas, mas esse impacto é relativamente menor em comparação com o associado ao cisalhamento do vento em baixos níveis.

A sinergia entre as observações e as simulações de alta resolução proporcionou uma análise abrangente com informações quantitativas cruciais sobre os controles ambientais da convecção isolada. Nossas descobertas contribuem para avançar nossa compreensão da convecção tropical e fornecem orientações valiosas para pesquisas futuras com o objetivo de aprimorar os modelos meteorológicos e climáticos.

**Palavras-chave**: Convecção tropical. Transição da convecção rasa para profunda. Controles ambientais. Experimento GoAmazon2014/5. Simulações de alta resolução.

# LIST OF FIGURES

# LIST OF TABLES

# LIST OF ABBREVIATIONS AND ACRONYMS

| | |
|---|---|
| AOSMET | Aerosol Observing System Surface Meteorology |
| ARM | Atmospheric Radiation Measurement |
| BBA | Biomass burning aerosol |
| CAM3 | Community Atmosphere Model version 3 |
| CAPE | Convective available potential energy |
| CEIL | Ceilometer |
| CIN | Convective inhibition |
| CIRSAN | Circulation in Santarém |
| Cong | Congestus |
| CRM | Cloud-resolving model |
| CTT | Cloud top temperature |
| CWV | Column water vapor |
| DOE | Department of Energy |
| ECMWF | European Centre for Medium-Range Weather Forecasts |
| ECOR | Eddy Correlation |
| GCM | General circulation model |
| GLDAS | Global Land Data Assimilation System |
| GNDRAD | Ground Radiometers |
| GNSS | Global Navigation Satellite System |
| GoAmazon | Green Ocean Amazon |
| INPA | National Institute of Amazonian Research |
| IOP | Intensive Operating Periods |
| LAI | Leaf area index |
| LBA | Large Scale Biosphere-Atmosphere |

| | |
|---|---|
| LCL | Lifting condensation level |
| LES | Large-eddy simulations |
| LFC | Level of free convection |
| LST | Local standard time |
| LWP | Liquid water path |
| MCS | Mesoscale convective system |
| MET | Surface Meteorology System |
| MLCAPE | Mixed-layer convective available potential energy |
| MLCIN | Mixed-layer convective inhibition |
| MODIS | Moderate Resolution Imaging Spectroradiometer |
| MPL | Micropulse lidar |
| MSE | Moist static energy |
| P3 | Predicted Particle Properties |
| PBL | Planetary boundary layer |
| QCECOR | Quality Controlled Eddy Correlation |
| RH | Relative humidity |
| RRTM | Rapid Radiative Transfer Model |
| RWP | Radar wind profiler |
| SAM | System for Atmospheric Modeling |
| SGS | Subgrid-scale |
| ShCu | Shallow cumulus |
| SIPAM | Amazon Protection System |
| SKYRAD | Sky Radiometers |
| SLM | Surface Land Model |
| SONDE | Balloon-borne sounding system |
| STD | Shallow-to-deep |

| | |
|---|---|
| TKE | Turbulence kinetic energy |
| TRMM | Tropical Rainfall Measuring Mission |
| VAP | Value-added product |
| VARANAL | Variational analysis |
| WACR | W-band ARM Cloud Radar |
| WETAMC | Wet Season Atmospheric Mesoscale Campaign |

# CONTENTS

# 1 INTRODUCTION

The Amazon forests play a critical role in regulating regional and global climate. The abundant precipitation wets the forests, which in turn produce intense evapotranspiration, releasing latent heat into the atmosphere while cooling the vegetation below (SILVA DIAS *et al.*, 2002). Clouds transport the latent heat vertically, warming the middle and upper troposphere, from where the heat is then redistributed to distant regions (ARAKAWA, 2004). Through these processes, forest and convection work together, serving as a cooling mechanism for the Amazon region while simultaneously acting as a potent heat source within the troposphere, influencing global atmospheric circulation (NOBRE *et al.*, 2009) and contributing to the large-scale transport of energy and moisture (ARRAUT *et al.*, 2012).

The intricate interplay between the atmosphere and the biosphere within the Amazon basin carries significant implications for potential climate change pathways, both on a global and local scale. Within this context, land management practices intended to expand agricultural land and pastures, coupled with growing urbanization, have led to significant deforestation, particularly in southeast Amazonia (ARTAXO *et al.*, 2013; STEEGE *et al.*, 2013). Biomass burning aerosol (BBA) emissions are highest in areas experiencing rapid deforestation and lowest in the tropical forests of central Amazonia, where the dense forest canopy and larger amounts of moisture generally prevent fires (DEFRIES *et al.*, 2008; REDDINGTON *et al.*, 2015). BBA absorbs and scatter radiation, thereby affecting the surface energy balance (LIU *et al.*, 2020). BBA emissions also elevate the concentration of cloud condensation nuclei, influencing the formation and lifetime of clouds (KOREN *et al.*, 2008; SENA; ARTAXO; CORREIA, 2013; KOCH; GENIO, 2010). These effects of BBA on convection can lead to alterations in precipitation patterns (GONÇALVES; MACHADO; KIRSTETTER, 2015), consequently affecting hydrological processes (KOREN *et al.*, 2004; LIU *et al.*, 2020). Specifically, the hydrological cycle in Amazonia has experienced intensified patterns in recent decades (GLOOR *et al.*, 2013). Notably, this intensification is exemplified by significant events like the occurrence of two strong droughts in 2005 and 2010 (MARENGO *et al.*, 2008; MARENGO *et al.*, 2011).

Despite the critical role of convection in the climate system, comprehending and simulating the convective processes is a formidable challenge due to the wide range of spatial and temporal scales involved (MAPES; MILLIFF; MORZEL, 2009; MONCRIEFF *et al.*, 2012; ZHANG *et al.*, 2013). In just a few hours, shallow cumulus convection, a small-scale phenomenon lasting tens of minutes and covering spatial scales of kilometers, has the ability to develop into congestus cumulus clouds, potentially accompanied by precipitation. This progression may further lead to a transition into deep convective clouds covering tens of kilometers within typical time scales of 2 to 4 hours. This phenomenon is known in the literature as the shallow-to-deep (STD) convective transition (WU; STEVENS; ARAKAWA, 01 Jun. 2009; HOHENEGGER; STEVENS, 2013; ADAMS *et al.*, 2013). Moreover, deep convection frequently becomes organized and experiences upscale growth into mesoscale convective systems with lifetimes spanning hours to a day and ranging in horizontal scale from 100 km to 1000 km. Likewise, complex physical processes from cloud microphysics (from micrometers to centimeters) to the generation of gravity waves (from a few kilometers to even thousands of kilometers) are intrinsically tied to deep convection (WALLACE; HOBBS, 2006; MAPES *et al.*, 2006; MAPES; NEALE, 2011).

General circulation models (GCMs), such as climate models, rely on parameterizations of convective processes and struggle to reproduce the STD convective transition over continental regions, a problem even more challenging in tropical rainforests due to the complex biosphere-atmosphere interactions already mentioned (BETTS, 2002; BETTS; JAKOB, 2002; BECHTOLD *et al.*, 2004; GRABOWSKI *et al.*, 2006). Their simulated precipitation peaks much earlier than observed (LIN; RANDALL; FOWLER, 2000; BETTS, 2002; COLLIER; BOWMAN, 2004; DAI; TRENBERTH, 2004), being an important source of bias and uncertainty to this day (SHERWOOD; BONY; DUFRESNE, 2014; STEVENS; BONY, 2013; ITTERLY; TAYLOR; DODSON, 2018; MAHER *et al.*, 2018; FREITAS *et al.*, 2020).

To circumvent the inherent challenges posed by parameterizations in GCMs, cloud-resolving models (CRMs), which explicitly resolve the up and downdrafts in clouds, have been used to study convective processes over both continental and oceanic regions. For example, KHAIROUTDINOV; RANDALL (2006) conducted high-resolution numerical simulations to investigate an idealized case over the Amazon. The findings highlighted the importance of cold pools in developing deep convection, while the impact of vertical wind shear and free tropospheric preconditioning were relatively minor. WU; STEVENS; ARAKAWA (01 Jun. 2009) used the same large-scale forcing as KHAIROUTDINOV; RANDALL (2006) but conducted their simulations using a different CRM. They observed that the STD convective transition occurs when shallow clouds, on average, become buoyant. WAITE; KHOUIDER (2010) conducted idealized high-resolution numerical simulations over the tropical Atlantic Ocean. Here, the authors emphasize the importance of congestus preconditioning, which reduces the impact of entrainment on cloud buoyancy, ultimately leading to the STD transition. In contrast, HOHENEGGER; STEVENS (2013) suggests that the significance of congestus preconditioning is exaggerated. Their results indicated that the transition from congestus to deep convection occurs relatively quickly, within 2 hours over land and 4 hours over the ocean. However, they found that it takes around 10 hours for congestus clouds to sufficiently moisten the atmosphere. This implies that dynamic factors play a more substantial role in driving convection. While CRM studies offer valuable insights into physical convective processes, they still require validation through high-resolution observations, which have been predominantly lacking for tropical rainforests until recently.

In the Amazon, important but often limited field campaigns have explored different aspects of convection. ADAMS *et al.* (2013) used data from the Amazon Dense Global Navigational Satellite System (GNSS) Meteorological Network, between July 2008 and December 2011, to evaluate the water vapor convergence associated with the STD transition. They found a weak and quasi-linear convergence timescale of approximately 8 hours, followed by a robust and non-linear convergence timescale of approximately 4 hours leading to the STD transition.

Recently, the Green Ocean Amazon (GOAmazon) 2014/5 Experiment (MARTIN *et al.*, 2016; MARTIN *et al.*, 2017) was held from 2014 to 2015 in the central Amazon, proving to be the most comprehensive observations of clouds and aerosols in the Amazon to-date. Analyzing this dataset, GHATE; KOLLIAS (2016) noted that the locally-driven precipitating days present an excess of water vapor above 2 km since the early morning during the dry season (defined by the authors as June-September). ZHUANG *et al.* (2017) observed that deep convective days are relatively moister in the low troposphere (0 to 6 km) since the early morning regardless of the season. SCHIRO *et al.* (2016) evaluated the conditionally average precipitation as a function of column water vapor (CWV) and found a robust relationship between precipitation and CWV, in both the central Amazon and tropical western Pacific. Previous studies are not conclusive about the relative importance of vertical wind shear in the Amazon. For example, ZHUANG *et al.* (2017) suggested that more intense low-level and deep-layer bulk wind shear facilitates the STD transition only during the dry season (defined by the authors as June-September). In contrast, CHAKRABORTY *et al.* (2018) suggested that a more intense low-level shear could inhibit deep convection during the transition season (defined by the authors as August–November), especially if it increases the entrainment of dry air. TIAN *et al.* (2021) also investigated wind shear, using the vertical derivative of the large-scale zonal wind as a metric. The authors suggested that vertical wind shear in the mid-troposphere could limit the vertical extent of convection regardless of the season.

Despite employing a combination of observations and numerical simulations to explore different aspects of convection, the aforementioned observational and modeling studies did not converge on a consensus regarding the triggering mechanisms of convection or which variables are most strongly associated with convective activity in tropical regions. Hence, there is an opportunity to further explore these issues and contribute to the ongoing discussion.

Here, we study the STD transition in the Amazon through observational analysis and numerical simulations. The observations are based on the GoAmazon2014/5 experiment. For the simulations, we apply the System for Atmospheric Modeling (SAM, Version

6.11.8), a CRM model (KHAIROUTDINOV; RANDALL, 2003), coupled with a simplified Surface Land Model (LEE; KHAIROUTDINOV, 2015). The thesis is organized as follows: Chapter 2 states the objectives. Chapter 3 provides a comprehensive review of convection and precipitation in the Amazon. Chapter 4 describes the general material and methods used in the observational and modeling studies, which includes an overview of the study region, the GoAmazon2014/5 experiment, large-scale fields, SAM model, and computational resources. Chapter 5 shows the observational study, and Chapter 6 addresses the modeling study. Chapter 7 shows the conclusions and future directions. Chapter 8 provides the data availability.

# 2 OBJECTIVE

The main goal of this thesis is to further our understanding of the mechanisms responsible for the shallow-to-deep (STD) convection transition in the Amazon through the synergy between observations and high-resolution numerical simulations. We focus mainly on the roles of moisture and vertical wind shear in triggering the STD transition during the wet season (December to April), which has received less attention than the dry and transition seasons.

For the observational study, we employ data from the GoAmazon2014/5 campaign. We separate the GoAmazon2014/5 days into three convective cloud regimes (shallow cumulus, congestus, and deep convection) and then assess the relative importance of moisture, convective instability, surface properties, and vertical wind shear in promoting the STD convection transition and enhancing precipitation.

For the modeling study, we apply the System for Atmospheric Modeling (SAM, Version 6.11.8), coupled with a simplified Surface Land Model (SLM), which provides a fair idealization of the land-atmosphere interactions responsible for the locally-driven STD convection transition. We use the GoAmazon2014/5 observations to validate the model results. Subsequently, we conduct sensitivity experiments where moisture or wind profiles are perturbed to evaluate their relative importance to the development of convection and precipitation.

# 3 LITERATURE REVIEW

This chapter reviews the convection and precipitation properties in the Amazon, discussing both observational and modeling studies. Special attention is given to the shallow-to-deep (STD) convective transition. Since it is not feasible to describe all the previous studies in the literature, we only intend to summarize the representative research on each topic.

## 3.1 Early LBA Campains in Southern Amazon

In the Amazon, crucial but often limited field campaigns have explored different aspects of convection. For example, the Tropical Rainfall Measuring Mission - Large Scale Biosphere-Atmosphere (TRMM-LBA) Experiment was held in the southwest Amazon basin in the Brazilian state of Rondônia from 1 November 1998 to 28 February 1999 (SILVA DIAS *et al.*, 2002). The experiment was an essential component of the NASA TRMM ground validation program and concentrated on the dynamical, microphysical, electrical, and diabatic heating characteristics of tropical convection in the Amazon.

KHAIROUTDINOV; RANDALL (2006) applied the SAM model to study an idealized case during the TRMM-LBA on 23 February 1999. The simulation lasted only 6 hours, starting at 07:30 Local Standard Time (LST). As the clouds grow, they produce more precipitation that, through the cold pool dynamics, creates larger boundary layer thermals that sustain the development of deep convection. When the evaporation of precipitation is switched off, the simulation only shows shallow convection with a few congestus clouds (see Figure 3.1). Hence, the authors conclude that cold pools are essential to the STD transition. In the same study, two additional experiments are conducted. First, they replace the initial condition of water vapor in the free troposphere with the corresponding condition at the end of the control case (free troposphere preconditioning). Second, they remove the vertical wind shear (horizontal wind set up to zero at all levels). Both experiments show little impact on convection and precipitation, suggesting a minor contribution of the early morning free tropospheric moisture and vertical wind shear to the STD transition in the Amazon.

Focusing on the Wet Season Atmospheric Mesoscale Campaign (WETAMC), which is a component of the LBA that took place in January and February 1999, HERDIES (2002) showed that the low-level wind presents a bimodal pattern with consecutive periods of easterlies and westerlies regimes, where RICKENBACH; LAURENT (2002, 2002) observed that these wind regimes are associated with changes in cloud features. During the westerly regime, Mesoscale Convective Systems (MCSs) were twice as extensive as those observed during periods of the easterly regime. Despite this, these MCSs produced

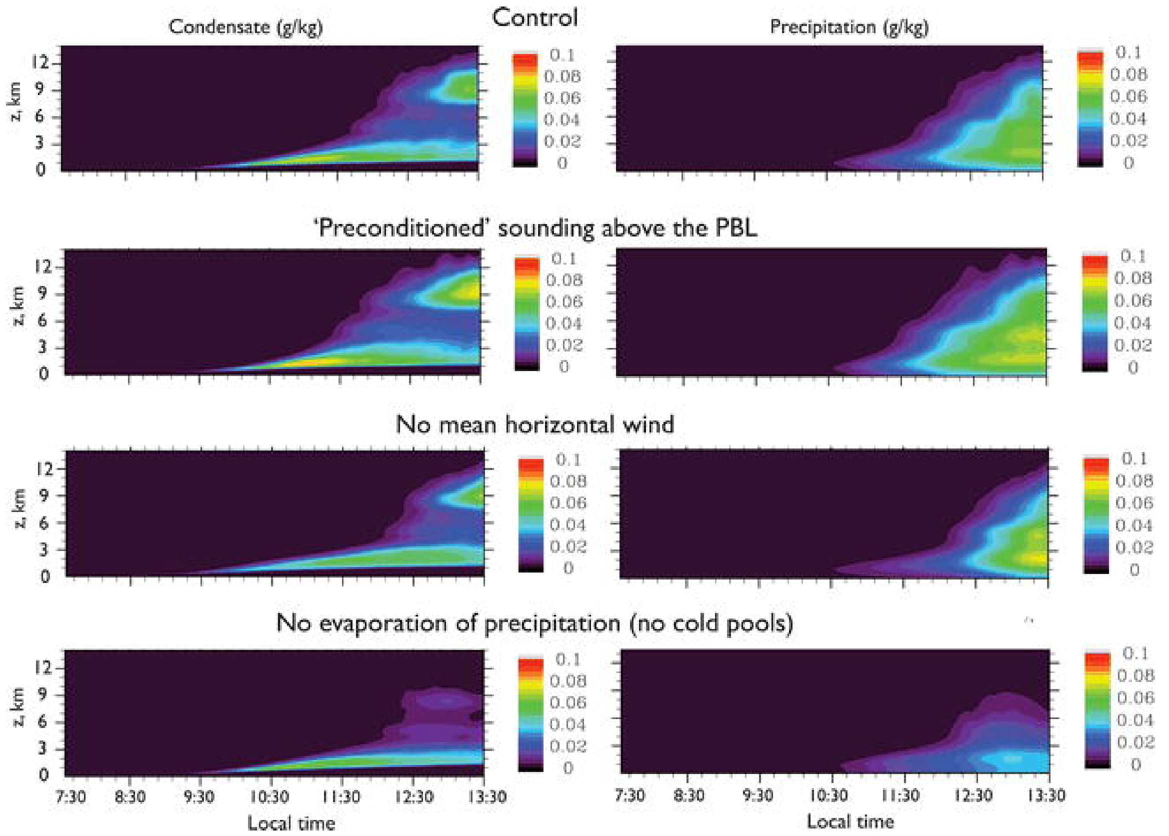

Figure 3.1 – Sensitivity experiments. Evolution of mean vertical profiles of (left) non-precipitating cloud mixing ratio (liquid+ice) and (right) precipitating water for the (top) control case and (bottom) three sensitivity runs. Adapted from KHAIROUTDINOV; RANDALL (2006), page 3434. Copyright 2006 American Meteorological Society. Used with permission.

approximately 1/4 less rainfall, mainly due to weaker convective rain intensity, and exhibited weaker updrafts in the upper troposphere. While both MCSs and isolated convective systems showed disorganized propagation during the westerly regime, the convective systems primarily propagated in alignment with the mid-level mean flow during the easterly regime. The study by BETTS (2002) focused on the diurnal cycle of surface properties. During the westerly regime, the downward solar radiation and the sensible and latent heat fluxes are lower, while the water vapor mixing ratio is greater. During the easterly regime, the water vapor shows a maximum in the early morning which drops to a minimum in the late afternoon as the cumulus clouds mix water vapor up and out of the subcloud layer in a higher rate than the surface evaporation can replenish it. TOTA *et al.* (2000) observed two main modes of precipitation: through isolated convection, which peaks in the afternoon at 16 LST, and organized convection associated with MCS, which shows a maximum during nighttime at 04 LST. In addition to precipitation, MACHADO (2002) also observed that the highest cloud cover occurs during the night. Typically, convective clouds exhibit minimum and maximum areas a few hours before and after the peak of precipitation.

## 3.2 Effects of River Breezes and Local Circulations

In addition to the environmental conditions, the land properties in a given region may also significantly affect the convection properties, particularly the spatial and temporal distribution of clouds and precipitation. For example, NEGRI (2002) analyzed a more extensive area covering the Amazon Basin and investigated the effects of geography (rivers, lakes, coasts) and topography on the diurnal cycle. They observed that the Amazon River, downstream of Manaus, enhances early morning precipitation and inhibits afternoon convection.

The intensive field campaign Circulation in Santarém/LBA (CIRSAN/LBA) was held around the confluence of the Tapajos River with the Amazon River in the Amazon Basin near Santarém (see Figure 3.2a), Brazil, in the dry season period from July to August 2001 (SILVA DIAS *et al.*, 2012). The objective of CIRSAN was to study the local circulation in the region around the confluence of two major Amazonian rivers. Boundary layer and upper air measurements were conducted from five local stations at varying frequencies.

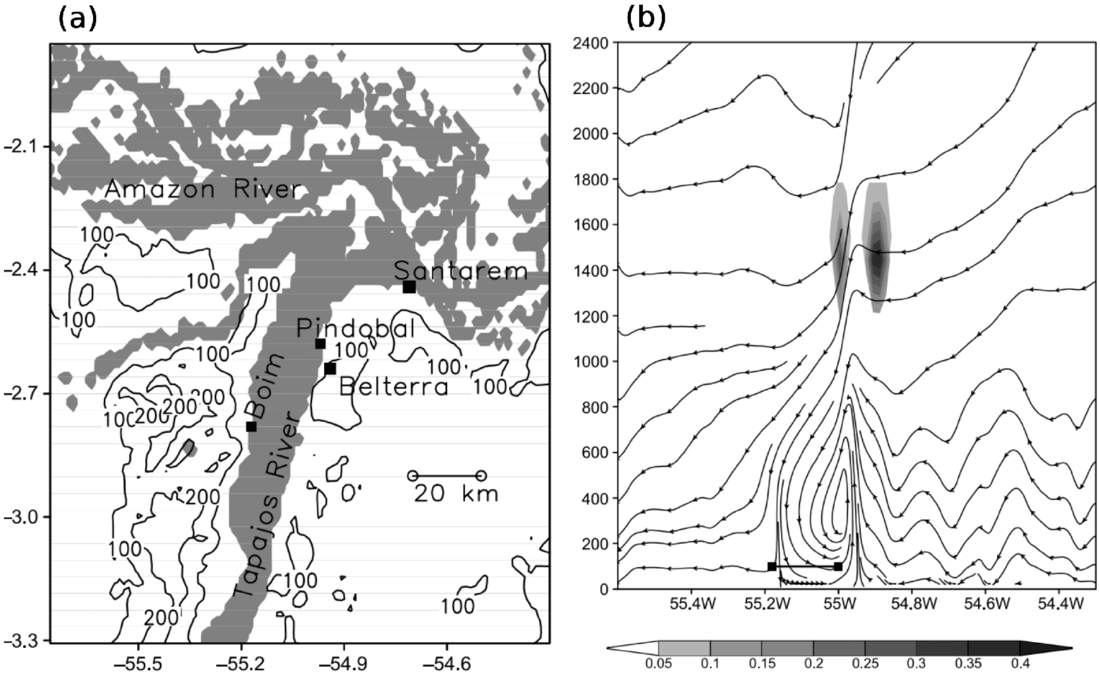

Figure 3.2 – CIRSAN/LBA Campaign. (a) Topography contours (in meters). The Tapajós River (north-south direction) and Amazon River (east-west direction) are shaded. The black-filled squares show the location of the stations (two at Belterra and one at the others). (b) Numerical simulation for a vertical cross-section at 2.7°S, at 17 LST on 28 July 2001. Streamlines indicate u and w while shaded areas show liquid water content in g $kg^{-1}$. The slab illustrates the position of the River Tapajós. Adapted from SILVA DIAS *et al.* (2004), (a) page 112 and (b) page 118. Copyright 2004 Springer-Verlag/Wien. Used with permission (Licence number: 5487790695023).

SILVA DIAS *et al.* (2004) used the CIRSAN/LBA observations and high-resolution simulations to investigate the river breeze circulation in the Amazon. For periods with weak (northeasterly) trade winds, the Tapajós River breeze induces a westerly flow at the eastern margin with an associated line of shallow cumulus. In the opposite western margin, clear sky conditions predominate. The numerical simulations suggest that a single cell forms during the late morning over the Tapajós River and evolves into the afternoon with ascending motion in the eastern margin and descending motion in the western margin suppressing cloud development (see Figure 3.2b). During the night, the formation of the land breeze at night produces convergence along the center of the Tapajós River. Sensitivity experiments indicated that river temperatures affect the breeze intensity. Higher temperatures in the Tapajós River induce a weaker breeze circulation during the diurnal cycle and a stronger land breeze at nighttime than the colder Amazon River. The wind direction with respect to the rivers also affects convection. The low-level trade wind is roughly perpendicular to the Tabajós and parallel to the Amazon River. While clouds are observed in the eastern margin of Tabajós and clear sky condition predominates on the opposite side, the Amazon River shows clouds in both margins.

FITZJARRALD *et al.* (2008) also studied the region around the confluence of the Tapajós River with the Amazon River, focusing on the spatial and temporal rainfall variability. They deployed a mesoscale network of weather stations near Santarém as part of the LBA-Ecological (LBA-ECO) Component (KELLER *et al.*, 2004). Using precipitation data collected by 38 rain gauges during the period 1998-2006 and satellite-based microwave sensor rain estimates, the authors also observed that the regions near the large rivers miss the afternoon convective rain, probably associated with subsidence motions promoted by the river breeze. However, this deficiency is more than compensated by enhanced nocturnal precipitation. This effect is local since nocturnal squall lines contribute less than half of total precipitation for areas only a few kilometers inland from the rivers. In most regions, the daily precipitation pattern shows one peak at about 03 LST and another at 15 LST in both the dry and wet seasons. The most significant fraction of nocturnal precipitation is observed in the Amazon River (see Figure 3.3, right panel), with the maximum accumulated precipitation occurring around the confluence of the Tabajós and Amazon Rivers (see Figure 3.3, left panel). Although further investigations are necessary, the importance of the Tapajós breeze on precipitation seems to extend only a few kilometers inland.

.

## 3.3 Recent Campaigns in Central Amazon

From July 2008 to December 2011, a dense Global Navigation Satellite System (GNSS) meteorological network in the Central Amazon conducted long-term observations

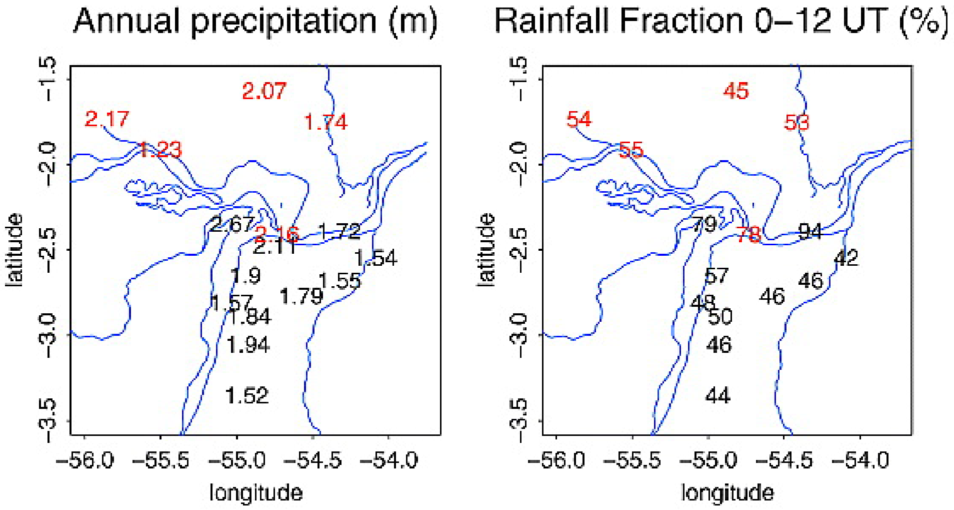

Figure 3.3 – Precipitation properties around the confluence of the Tapajós River with the Amazon River (based on the LBA-ECO Component). (left) Annual accumulated precipitation (meters) for stations that conduct hourly observations. (right) Nocturnal rainfall fraction (%). See the text and reference for more detail. Adapted from FITZJARRALD *et al.* (2008), page 14. Copyright 2008 American Geophysical Union. No need to request permission.

of column water vapor (CWV[1]) and surface meteorology (ADAMS *et al.*, 2013). The campaign was part of the National Oceanic and Atmospheric Administration/Earth System Research Laboratory (NOAA/ESRL) Ground-Based Global Positioning System (GPS) Meteorological Network located at the National Institute of Amazonian Research/LBA (INPA/LBA) Experiment in Manaus, Brazil. A GNSS ground-based meteorology provides “relatively inexpensive” (about $10,000), high frequency (5–30 min), all-weather, CWV data with 1-2 mm accuracy relative to radiosondes (temporal frequency is $\sim$ 6 hours) and radiometers (only works for fair-weather conditions) (MATTIOLI *et al.*, 2007; LEBLANC *et al.*, 2011). An obvious counterpoint of GNSS is that CWV is an integrated measurement of water vapor, which does not provide any detail of its vertical distribution. Despite that, it is valuable as some studies have indicated, for example, that CWV shows a surprisingly empirical solid relationship with precipitation (ZENG, 1999; BRETHERTON; PETERS; BACK, 2004). Besides, most previous studies were conducted over oceanic regions, suggesting a new opportunity to check whether their results would apply to a tropical forest.

ADAMS *et al.* (2013) used the 3.5 years of data from the INPA/LBA Campaign and (GOES-10/12) satellite observations of brightness temperature to analyze the water vapor convergence timescale associated with the STD transition. They identified deep convection as events showing a step decay of the cloud top temperature (CTT), which corresponds to the brightness temperature for cloud pixels, with a concomitant increase in CWV and surface meteorology indicating either precipitation or changes in temperature

---

[1] Other terms are used indistinguishably in the literature, such as Precipitable Water Vapor (PWV) and Integrated Precipitable Water (IPW). In this thesis, we chose the term CWV.

and wind gust. Changes in CTT are associated with cloud growth. Thus, a maximum threshold of 235 K for CTT is defined to identify the high cloud. A time range of 2 hours is also defined to verify if the shallow stage evolves into the deep clouds in the characteristic convective cloud lifetime. The presence of precipitation or wind gust is necessary to exclude high clouds such as cirrus or stratiform clouds. Using this criteria for the 3.5 years of data, the authors classified 320 convective events, which were further investigated through the composite time series centered at $t = 0$, the time of maximum CWV associated with the STD transition (see Figure 3.4). Two characteristic timescales for water vapor convergence were identified. First, a slow, quasi-linear timescale of approximately 8 hours. Here, the authors argue to be mainly associated with diurnal surface evaporation. The second is a rapid nonlinear ramp-up of approximately 4 hours associated with the STD transition. The 4 hours water vapor timescale is particularly robust, regardless of convective intensity, seasonality, or nocturnal versus daytime convection. The authors emphasized that was still an open question to what extent environmental stability, tropospheric humidity, and cloud condensate advection, among other external factors, contribute to the water vapor convergence in the STD transition and mesoscale organization. In fact, this is still true today.

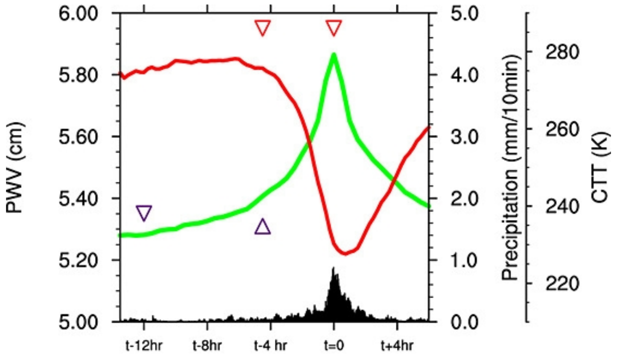

Figure 3.4 – Water vapor convergence. The $t = 0$ corresponds to the peak time of CWV (PWV in the reference notation). The green line shows CWV, the red line shows CTT, and the black bar indicates the precipitation rate. The blue and red triangles represent the weaker and stronger water vapor timescales, respectively. Adapted from ADAMS *et al.* (2013), page 2821. Copyright 2013 American Geophysical Union. No need to request permission.

.

As the INPA GNSS station was operating during the INPA/LBA Experiment, the implementation of more GNSS stations in the Central Amazon was planned to continue long-term studies of the STD transition, mesoscale organization, and the interaction with water vapor fields (ADAMS *et al.*, 2011). The Amazon Dense GNSS Meteorological Network (ADGMN) originated from these new GNSS installations in the Central Amazon (ADAMS *et al.*, 2015). The ADGMN promoted two mesoscale ($\sim$ 100x100 km$^2$) intensive campaigns in the Amazon: (1) 1-year experiment from April 2011 to April 2012 with 20 GNSS meteorological sites in and around Manaus and (2) 6-week (June to July 2011) experiment with 15 GNSS meteorological sites in and around Belém, the latter in collaboration with the Cloud Processes of the Main Precipitation Systems in Brazil: A Contribution to Cloud-Resolving Modeling and to the Global Precipitation Measurement (called as CHUVA) Project in Brazil.

Using CWV data from the ADGMN Campaign supplemented with surface meteorology and satellite (GOES-12) observations, ADAMS *et al.* (2015) first identified the days into convective and non-convective. The diurnal cycle of convective days shows greater CWV after 10 LST, with its time rate $\Delta$CWV/$\Delta$t being more than 50% higher than the observed for non-convective days. The seasonal variation of the CWV diurnal cycle is mainly associated with water vapor convergence, which is earlier in the day and usually less intense during the wet season. In ADAMS; BARBOSA; RíOS (2017), the authors used the same observations to derive a metric for the spatiotemporal water vapor–deep convection correlation. This work is essentially an extension from ADAMS *et al.* (2013). The authors identified 67 events fulfilling the deep convective criteria for the ADGMN data. They noted that the spatial correlation of PWV shows a fair linear decay with the station distances (correlation($t$) = 1 - slope($t$) distance). Furthermore, the linear coefficient of the spatial correlation continually decreases from 6 hours before the event until the transition time (Figure 3.5a). Notably, the linear slopes show a remarkable exponential behavior with time (see Figure 3.5b), where they estimated that the correlation decay timescale is about 3.5 hours. The authors argue that this corresponds to a metric from the deep tropics that numerical models could replicate. However, it is still missing further investigation of this metric in the literature.

From 2014 to 2015, the deployment of the first Atmospheric Radiation Measurement (ARM) Mobile Facility (AMF-1) in the context of the Green Ocean Amazon (GOAmazon) 2014/5 field campaign (MARTIN *et al.*, 2016; MARTIN *et al.*, 2017) provided comprehensive measurements of surface, cloud, precipitation, radiation, and thermodynamic properties in the Amazon region. Nine ground sites and two aircraft were used to survey the environs of Manaus, Brazil. The GoAmazon2014/5 observations have been used in several studies in the recent years, including atmospheric chemistry, boundary layer, and atmospheric convection to name a few areas.

One of these studies, by GHATE; KOLLIAS (2016), observed a bimodal distribution of precipitation during the dry season (June–September), where the nighttime precipitation peak is associated with large propagating systems (non-local effects) and the daytime precipitation peak is mainly related to the local land-atmosphere interactions. This result agrees with previous studies in southern Amazon (TOTA *et al.*, 2000; MACHADO, 2002; FITZJARRALD *et al.*, 2008; ADAMS *et al.*, 2013), GHATE; KOL-

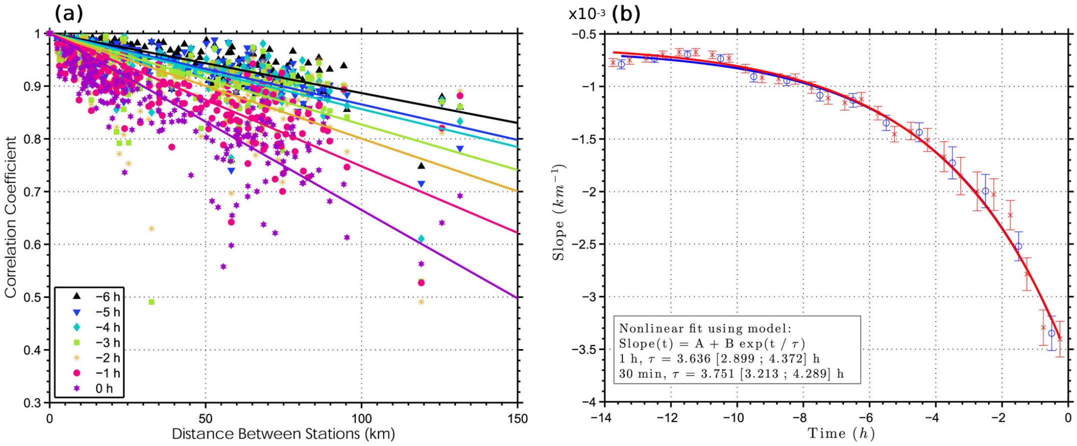

Figure 3.5 – Spatiotemporal water vapor–deep convection correlation. (a) Scatterplot of correlation *versus* separation distance as a function of STD transition time for the 67 convective events. The correlation is computed in hourly bins. (b) Temporal evolution of correlation *versus* separation distance slope with the exponential fit and error bars. It is shown the hourly (blue lines and circles) and 30-minute (red line and x symbols) time bins for comparison purposes. The estimated decay timescale, $\tau$, is shown in the legend. See the text and reference for more detail. Adapted from ADAMS; BARBOSA; RíOS (2017), page 283. Copyright 2017 American Meteorological Society. Used with permission.

LIAS (2016). Since the early morning, the precipitating days show an excess in water vapor above 2 km, possibly lowering the lifting condensation level and reducing convective inhibition and entrainment to trigger the STD transition. Using the European Centre for Medium-Range Weather Forecasts (ECMWF) Reanalysis data, they also noted that the horizontal advection of moisture above the boundary layer is slightly positive during precipitating days and weakly negative for non-precipitating days, suggesting a possible relationship between the large-scale water vapor convergence and diurnal precipitation.

SCHIRO *et al.* (2016) evaluated the correlation between CWV and precipitation using data from several sources in the tropics. This included GNSS measurements during the INPA/LBA Experiment, data from the microwave radiometer, radiosondes, and acoustic gauge during the GoAmazon2014/5 Campaign. In addition, satellite measurements of precipitation (TRMM 3B42 version 7) and in-situ measurements of radiosondes and rain gauges were also used over the Tropical Western Pacific at Nauru and Manus Island. They found a robust relationship between CWV and precipitation across various instruments and locations. Specifically for the GoAmazon2014/5, the results are shown in Figure 3.6. The precipitation probability is approximately zero for CWV $<$ 5.0 cm, and increases exponentially above this threshold. However, for significantly high values in CWV, around 7.0 cm, the probability of precipitation tends to decrease. This basic form of the CWV-Precipitation relationship applies to all the analyzed data, including tropical land and ocean regions, time of the day (nighttime and daytime), and particularly for time averages and spatial scales up to 3 hours and 2.5° (domain ~ 200x200 km$^2$).

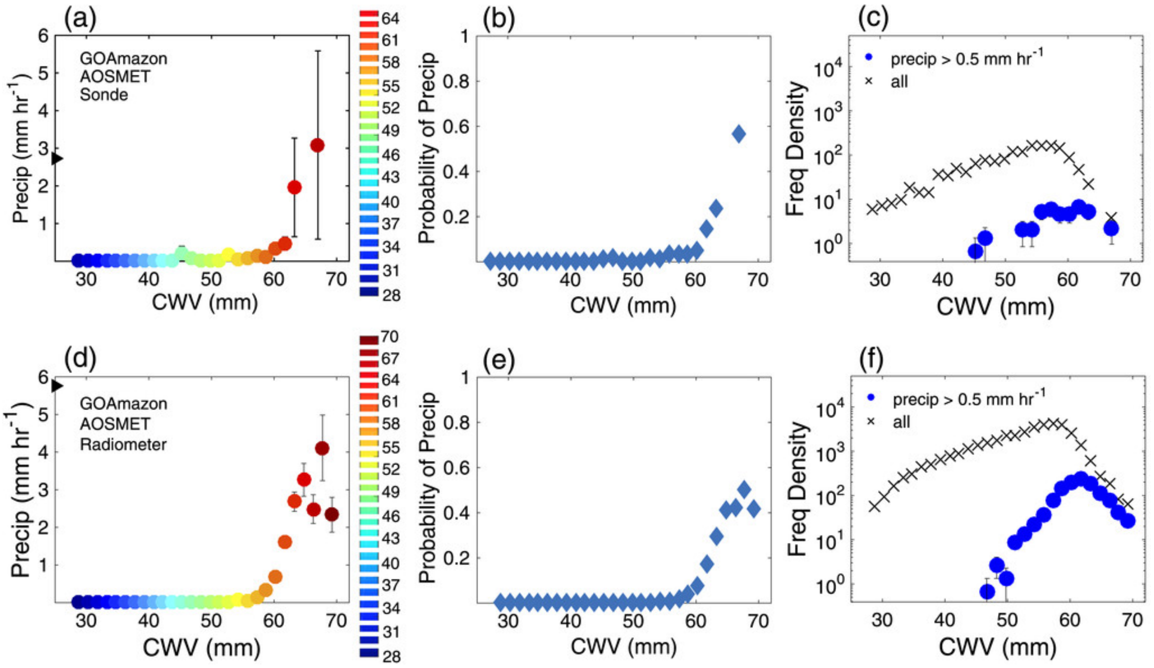

Figure 3.6 – The relationship between CWV and precipitation. Results for the GoAmazon2014/5 observations. (a) The 1-h-average precipitation (mm h$^{-1}$) centered at the time of radiosonde launch conditionally averaged on CWV (mm). The mean of precipitating points greater than 0.1 mm h$^{-1}$ is 2.72 mm h$^{-1}$, given by the black triangle on the y-axis, and the error bars represent one standard error. (b) The fraction of observations per CWV bin with rain rates greater than 0.5 mm h$^{-1}$, for radiosonde CWV. (c) The frequency density of all points and precipitating points with rain rates greater than 0.5 mm h$^{-1}$, for radiosonde CWV. Error bars are the square root of the counts in each CWV bin normalized by the bin width. (d)–(f) As in (a)–(c), respectively, except using 15-min-average CWV from microwave radiometer. The CWV bins for each analysis set are given by their respective color bars. The highest bin for the radiosonde analysis has a width of 6 mm and a range from 64 to 70 mm, differing slightly from the radiometer data. See the text and reference for more detail. Adapted from SCHIRO *et al.* (2016), page 4047. Copyright 2016 American Meteorological Society. Used with permission.

Following a similar approach, SCHIRO *et al.* (2018) evaluated the role of vertical velocity and buoyancy for local deep convection and mesoscale organization. They used the vertical velocity from the radar wind profiler (RWP), and computed the mass flux as $m = \rho\sigma w$, where $\rho$ is the mean density profile, $w$ is the mean vertical velocity, and $\sigma$ depends on the updraft properties (see reference for details). Both vertical velocity and mass flux increase nearly linearly with height in the lower troposphere up to 3.5 km. Their profile is also comparable in isolated deep convection and mesoscale system. The authors also computed the layer-mean (over 1000-200 hPa levels) buoyancy using deep-inflow assumptions described in HOLLOWAY; NEELIN (2009). The probability of precipitation and conditionally averaged precipitation tends to increase with the layer-mean buoyancy (see Figure 3.7). The buoyancy-precipitation relationship is comparable and even more robust than the observed between CWV and precipitation (see Figure 3.6). Besides, it is remarkably similar between local deep convection and mesoscale organization, regardless of the deep-inflow mixing. Note that the onset of precipitation occurs at negative values of lower-troposphere layer-mean buoyancy. The authors suggest that this could be due to sampling mismatches between precipitation and the thermodynamic fields. Alternatively, it might indicate the influence of other effects that were not accounted for in the formulation of buoyancy within their study. For example, the authors mention the mechanism of air rapidly recirculating in and out of a cloudy updraft, which could introduce a positive term to buoyancy (YEO; ROMPS, 2013).

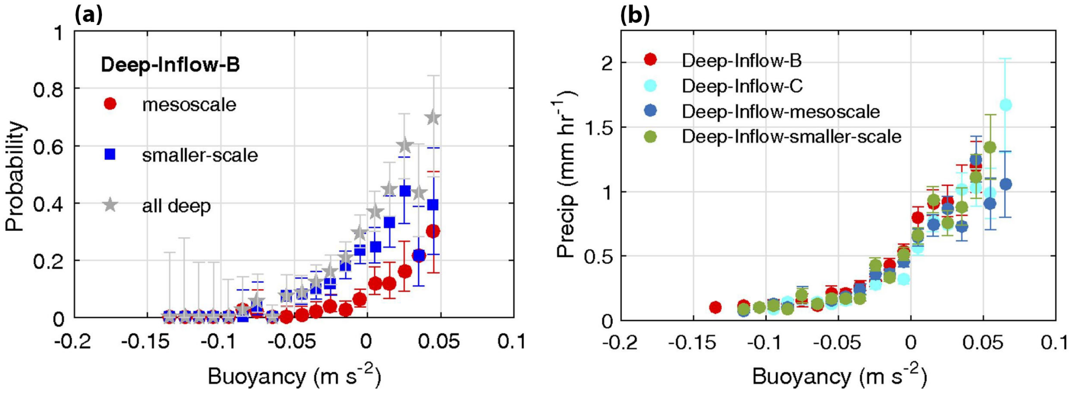

Figure 3.7 – The relationship between buoyancy and precipitation. (a) Probability of observing deep convection within 1-h of radiosonde launch as a function of the layer-mean buoyancy computed with Deep-Inflow-B mixing. Probability is shown for mesoscale and smaller scale (local deep) convection. Error bars are 5th- to 95th-percentile Wilson score intervals. (b) Precipitation rate (average from the S-band radar) within 1-h of radiosonde launch conditionally averaged to the layer-mean buoyancy using the four variants of deep-inflow mixing. See the text and reference for more detail. Adapted from SCHIRO *et al.* (2018), page 4580. Copyright 2018 National Academy of Sciences. Used with permission.

ZHUANG *et al.* (2017) assessed the environmental conditions that control the STD transition in the Amazon, giving special attention to its seasonal differences. They found that humidity plays a crucial role, with deep convection occurring under moister conditions in all seasons (see Figure 3.8), particularly during early morning in the low and mid-levels (below 6 km). The water vapor anomaly, computed as the difference between the deep and shallow-congestus days, is weaker and shallower during the wet season (January–May) compared to the dry (June–September) and transition (October–December) seasons, when it reaches up to 6 km. As the day progresses, the water vapor tends to decrease in the low levels and increase in the free troposphere. At the end of the diurnal cycle, around 2 km, the deep days can show drier conditions than shallow-congestus days during the wet and transition seasons. The authors also assessed the vertical wind shear using the bulk approach for the 0-3 and 0-6 km. The bulk shear takes the wind speed difference between the top and bottom layers. The low-level shear is stronger on deep days for all seasons, while the mid-level shear is more significant on shallow-congestus days in the wet and transition seasons. Thus, the authors suggest that vertical wind shear possibly plays a more prominent role in the STD transition only during the dry season, when the deep convection shows stronger shear intensity in both the low- and mid-levels.

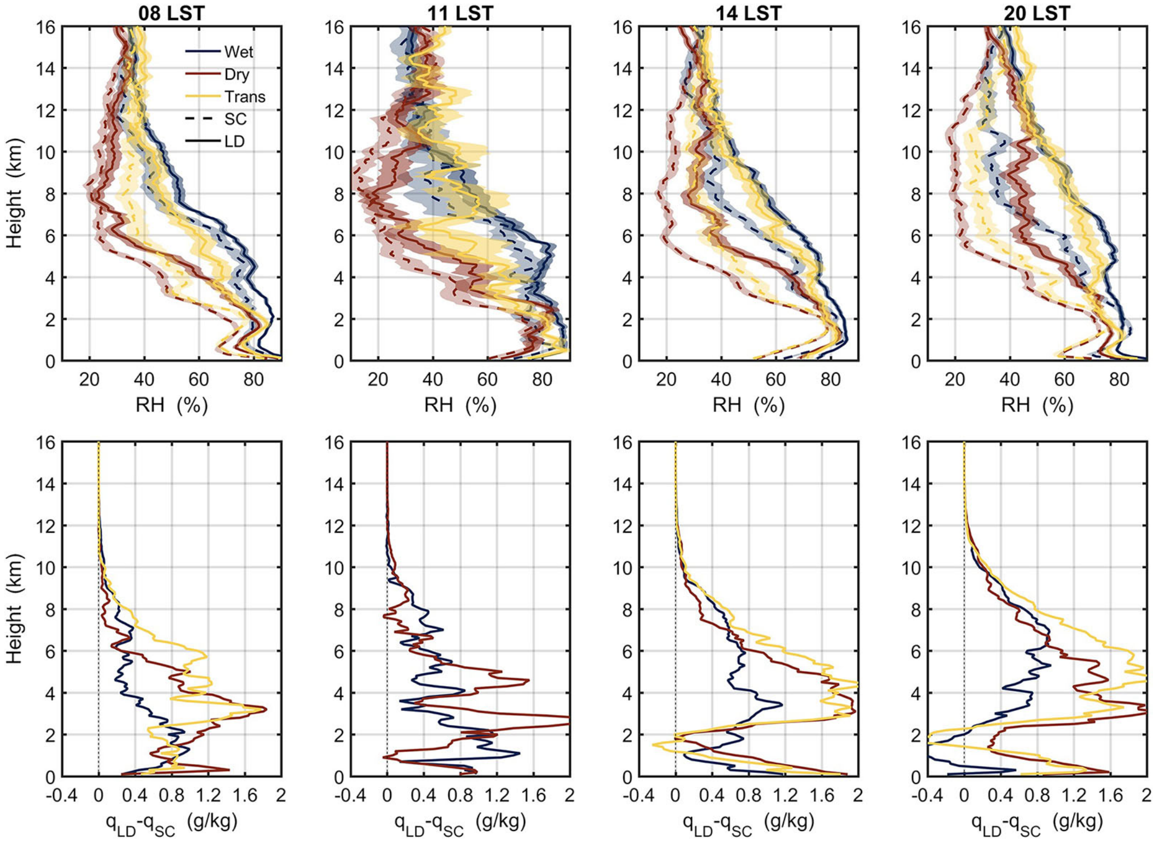

Figure 3.8 – Moisture environmental condition in shallow-congestus (SC) and local deep (LD) convective days. Composite RH profiles in SC/LD days and (bottom row) specific humidity difference profiles between LD and SC days at 08, 11, 14, and 20 LST in the wet ($N_{wet,LD}$ = 116 events, $N_{wet,SC}$ = 47 events), dry ($N_{dry,LD}$ = 56 events, $N_{dry,SC}$ = 113 events), and transition ($N_{tra,LD}$ = 40 events, $N_{tra,SC}$ = 50 events) seasons. Shaded regions (top row) represent one standard error. Adapted from ZHUANG *et al.* (2017), page 2659. Copyright 2017 American Geophysical Union. No need to request permission.

CHAKRABORTY *et al.* (2018) analyzed the environmental conditions leading to the STD transition in the Amazon during the dry-to-wet season transition period (August–November). In contrast to shallow convection, significant moister conditions in the free troposphere and boundary layer are observed prior to the STD transition. Using a simplified entraining plume model, they noted that free tropospheric humidity is crucial to increase the plume's buoyancy. The authors also assessed the role of vertical wind shear. They defined the low-level vertical wind shear as the difference in wind speed between the 937 and 737 hPa pressure levels. The deep-level shear considers the layer between

887 hPa and 287 hPa. In opposition to ZHUANG *et al.* (2017), which relates stronger shear to deep convection, CHAKRABORTY *et al.* (2018) shows that shallow convection is associated with strong low-level and weak deep-level shear intensity. They suggest that vertical wind shear could play a more vital role in limiting the development of deep convection, particularly if the cloud entrainment of dry air increases under more intense low-level vertical wind shear conditions. However, the low-level shear intensity could be simply a non-causal effect if shallow convection leads to greater low-level shear.

In the more recent work, TIAN *et al.* (2021) analyzed the vertical wind shear through the vertical derivative of the zonal wind. Moreover, they used the large-scale wind from variational analysis (TANG *et al.*, 2016) instead of local observations associated with radiosonde or radar wind profiler as in ZHUANG *et al.*; CHAKRABORTY *et al.* (2017, 2018). Here they noted a relevant difference in the vertical wind shear in the mid-troposphere among congestus and deep convection days (see Figure 3.9), suggesting that wind shear may limit the vertical extent of convection regardless of the season. In the low levels, between 850-900 hPa, the shear intensity is greater in the shallow regime than the deep regime. This result is the opposite as observed in (ZHUANG *et al.*, 2017), where deep convection is associated with stronger low-level shear in all seasons. Thus, the relative contribution of vertical wind shear to deep convection in the Amazon is still unclear, and further investigations are necessary. The authors also investigated the diurnal cycle of precipitation. During non-local deep days, which were defined by the presence of nighttime convection, cold-pools, or mesoscale systems within the analyzed area (100x100 km$^2$), precipitation usually shows a peak in phase with the surface daytime heating (around noon). In the case of isolated deep convection, one additional peak is also observed around 16-17 LST associated with the late afternoon STD transition as reported by (TOTA *et al.*, 2000). Using a simplified plume model with thermodynamic and dynamical constraints, the authors inferred that the initial vertical velocity at the cloud base and buoyancy is essential in helping parcels ascend to the level of free convection. After that, the entrainment of dry air and lower free troposphere humidity become crucial to vertical cloud development.

HENKES *et al.* (2021) investigated the morning boundary conditions related to the subsequent daytime cloud development during the IOP2 (15 August-15 October 2014), in the dry season. They selected three shallow and three deep convective days with significant cloud and thermodynamic observations. Although a composite analysis based on three events provides limited statistics, the authors still found relevant results summarized in a conceptual model shown in Figure 3.10. The boundary layer grows under moister and colder conditions during deep convective days. The transition from the stable layer to the convective boundary layer is also faster under moister and more intense shear conditions. Humidity lowers the lifting condensation level and contributes to the balance between radiative cooling and turbulent mixing during nighttime, providing more sensible heat

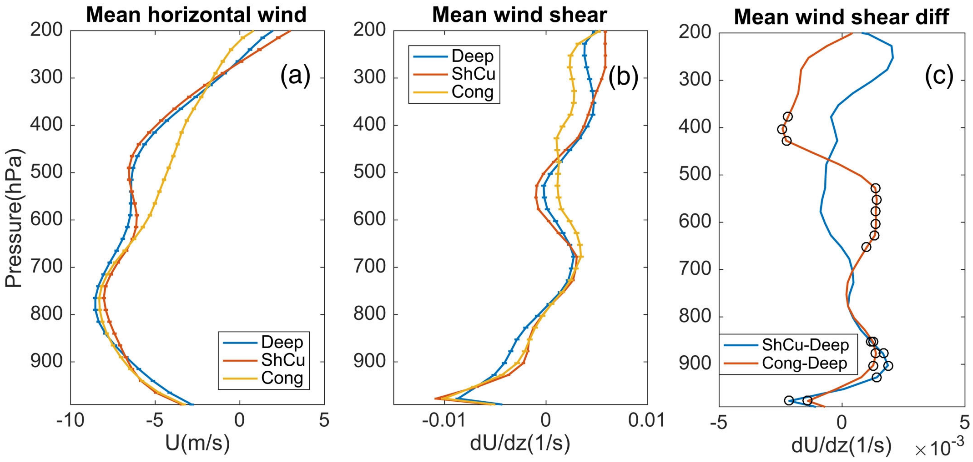

Figure 3.9 – Vertical wind shear. (a) Mean horizontal wind for the shallow cumulus (ShCu, 65 events), congestus (Cong, 46 events), and Deep (126 events) days between 08:00 and 11:00 LST. (b) Mean wind shear as calculated by $dU/dz$. (c) Wind shear difference between ShCu and Deep and between Cong and Deep. The error bars in (a and b) represent one standard error, and the black dots in (c) denote the vertical levels with statistically significant differences at 0.05 significance level. Adapted from TIAN *et al.* (2021), page 13. Copyright 2021 American Geophysical Union. No need to request permission.

flux in the early morning. The sensible heat flux favors the rapid growth stage of the convective boundary layer that begins around 08:00 LST. The duration of the transition of the nocturnal to convective boundary layer impacts the subsequent convective strength and formation of convective clouds.

Still based on the GoAmazon2014/5 Experiment, EISSNER *et al.* (2021) used cloud top height measurements to constrain an entraining plume model to estimate bulk entrainment rates (see Figure 3.11). The authors identified 469 cloud events with available thermodynamic profiles (based on radiosonde and microwave radiometer data) to evaluate the entrainment rate. The results indicate an entrainment rate ranging from 0.16-2.8 km$^{-1}$ with an average of 0.58 ± 0.10 km$^{-1}$. Using the coefficient of determination ($R^2$), they found that the entrainment rate shows a relatively higher correlation with cloud thickness ($R^2 = 0.28$), maximum buoyancy in the lowest 5 km ($R^2 = 0.27$), and cloud size ($R^2 = 0.21$). Although these variables showed a more significant relative contribution to the entrainment in shallow and congestus clouds, the coefficient of determination is still under 0.3 in all cases, which does not explain the dominant factor in less developed convective clouds, and nothing is said about the deep clouds. In that case, some fundamental observational challenges exist to estimate the entrainment rate for deep convection. First, high clouds usually extend above 8 km. The vertical profile from microwave radiometers ranges up to 10 km and is also limited to fair weather conditions. Besides, radiosonde profiles are generally taken every 6 hours, a poor temporal resolution to assess deep convection evolution. Inaccuracy in cloud top height measurements is also a rele-

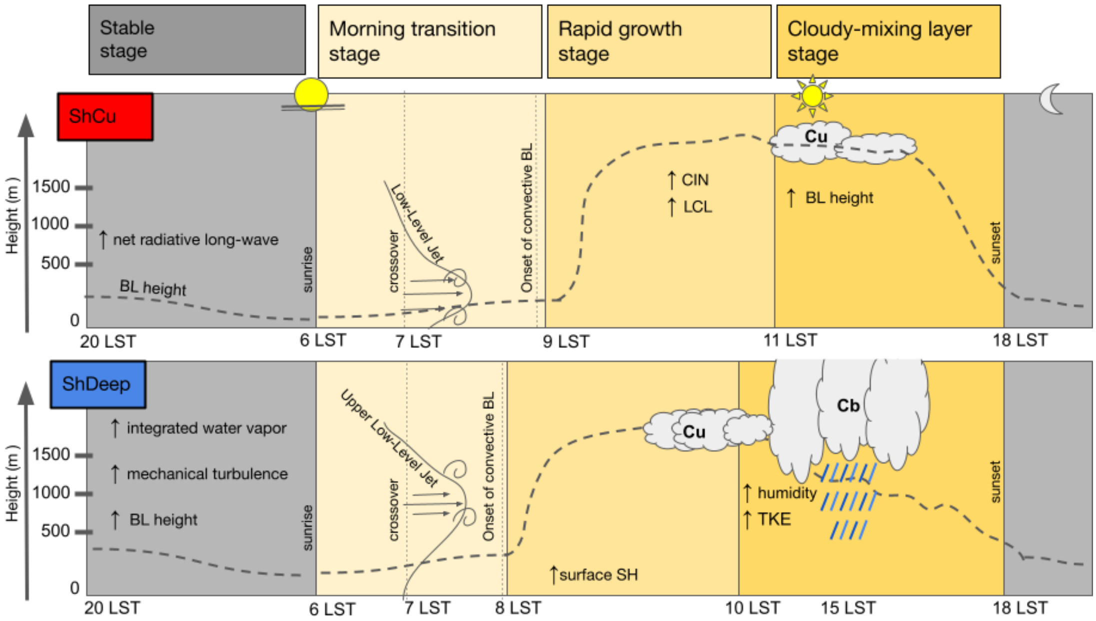

Figure 3.10 – Conceptual model of Boundary Layer processes on shallow (ShCu, top) and deep convective (ShDeep, bottom) days illustrating the cloudy boundary layer stages. The dashed curves represent the boundary layer height for both regimes. BL, SH, CIN, LCL, and TKE stand for the boundary layer, sensible heat flux, convective inhibition, lifting condensation level, and turbulent kinetic energy, respectively. See the text and reference for more detail. Adapted from HENKES *et al.* (2021), page 13221. Copyright 2021 Authors. The work is distributed under the Creative Commons Attribution 4.0 License.

vant factor of entrainment uncertainty. Finally, the entraining plume model is also hugely simplified. Therefore, new observations and more comprehensive methods are necessary to characterize the entrainment and how it affects the STD transition.

## 3.4 Main Points

All these studies show evidence of the highly non-trivial characteristics that can affect the STD transition. The evaporation of precipitation contributes to cold pool formation, which may organize convection and enhance precipitation. The river breeze inhibits convection near the river margin in the afternoon. However, the strength of the river breeze depends on the river temperature, and its impact also depends on the direction of the large-scale wind. Both precipitation probability and intensity show a significant correlation with column water vapor and layer-mean buoyancy.

While the importance of moisture for convection is unquestionable, there are still unresolved questions that need to be addressed. For example, ZHUANG *et al.*; TIAN *et al.* (2017, 2021) reported that deep convective days exhibit a moister profile from the surface up to mid-levels since early morning. On the other hand, GHATE; KOLLIAS (2016) suggested that locally-driven precipitating days show an excess of water vapor only above

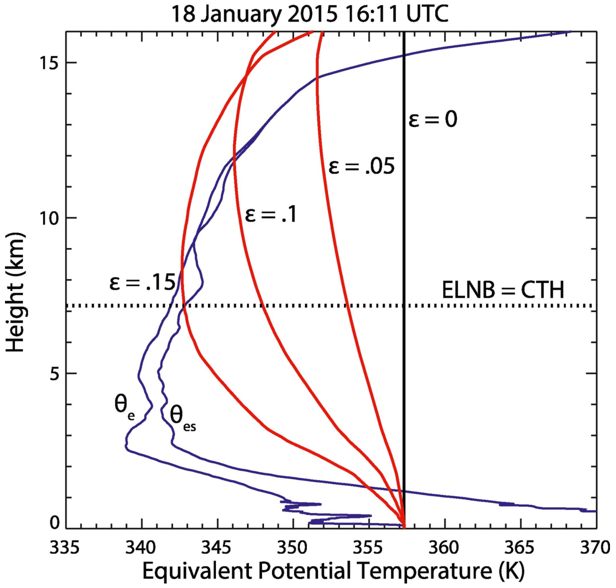

Figure 3.11 – Entraining plume model applied to estimate the bulk entrainment rates. The blue lines represent the environmental equivalent potential temperature ($\theta_e$) and saturation equivalent potential temperature ($\theta_{es}$). The black line is the undiluted parcel $\theta_e$, and the red lines are the $\theta_e$ for parcels experiencing different entrainment amounts. Here, the entrainment rate is 0.15 km$^{-1}$ since that is the rate at which the cloud top height (CTH) equals the entraining level of neutral buoyancy (ELNB). Adapted from EISSNER *et al.* (2021), page 3. Copyright 2021 American Geophysical Union. No need to request permission.

2 km. In this case, KHAIROUTDINOV; RANDALL (2006) showed that free troposphere preconditioning plays a minor role in convection, which does not support the anomaly observed by GHATE; KOLLIAS (2016). The work by ADAMS *et al.* (2013) indicated that moisture convergence could potentially be more important than preconditioning in developing convection and precipitation, although it is unclear whether the water vapor convergence is a cause or effect of convection.

The role of vertical wind shear in the STD transition is also somewhat unclear. For example, while ZHUANG *et al.* (2017) suggested that more substantial low- and mid-level shear favors the STD transition, CHAKRABORTY *et al.* (2018) indicated that a more intense low-level shear could inhibit deep convection. As described in the literature, the magnitude and orientation of vertical wind shear can either suppress or enhance convection (COTTON; BRYAN; HEEVER, 2011; HOUZE Jr., 2014). For example, wind shear can tilt the updrafts and downdrafts within a convective cloud. The updrafts are warm, moist air rising due to buoyancy, while downdrafts are cooler, drier air descending. The change in wind speed and direction with height causes the updrafts and downdrafts to be displaced from each other; hence it allows the updrafts to continue feeding the storm's development, leading to longer-lasting and more organized convective systems. Conversely, extremely high or unidirectional shear can hinder convective processes by disrupting the organization of updrafts and downdrafts. Furthermore, wind shear may also increase the entrainment of drier air into the cloud, significantly impeding its development. Thus, the wind properties in a given region play a decisive role in convection dynamics.

This project mainly focuses on the role of moisture and vertical wind shear in controlling the STD convective transition (Chapter 2). However, as discussed above, many other factors, from microphysics to large-scale dynamics, might contribute to convection and precipitation in the Amazon.

# 4 MATERIAL AND METHODS

This chapter presents the general materials and methods used in the observational and modeling studies. Firstly, we describe the study region. Second, the GoAmazon2014/5 experiment and the important instruments and large-scale fields used in our study are presented. Finally, we describe the System for Atmospheric Modeling (SAM) and the computational resources used to conduct the numerical simulations. Specific details on data and methods for the observational and modeling study are provided later in each corresponding chapter.

## 4.1 Study Region

Here, we provide an overview of the properties and climate of the Amazon Basin as a whole, which includes the central Amazon, where the GoAmazon2014/5 experiment took place. The specific domains associated with the observational (Chapter 5) and modeling (Chapter 6) studies are described in each corresponding chapter.

The Amazon is the most extensive tropical rainforest on the planet. It covers most of the Amazon Basin (see Figure 4.1), which spreads from 5°N to 18°S and 42° to 74° W, totalizing an area of about 7 million square kilometers. Of these, about 5.3 million square kilometers are covered by forests, representing 40% of the tropical forest areas in the world (LAURANCE, 2001; ARAGÃO *et al.*, 2014; WENG *et al.*, 2017). The Amazon covers nine countries in South America, where most of its location belongs to Brazil, about 60%, followed by Peru (13%), Colombia (10%), and minor contributions from Bolivia, Ecuador, French Guiana, Guyana, Suriname, and Venezuela. It contains nearly a quarter of the world's freshwater, produces roughly one-third of the global oxygen, stores around 150-200 billion tons of carbon, and is home to about 10-15% of the terrestrial biodiversity (LEWINSOHN; PRADO, 2002; MALHI *et al.*, 2006; HECKENBERGER *et al.*, 2007; HUBBELL *et al.*, 2008; SAATCHI *et al.*, 2011).

The Amazon Basin topography (Figure 4.1a) shows an extensive plan with minor changes in elevation of about 120 m in a range of 3400 km. The Basin shows significant altitudes only on its borders, with Guiana Highlands in the north ($\sim$ 1000 m), Brazilian Highlands in the south ($\sim$ 700 m), and Andes Mountains in the west ($\sim$ 5000 m). The Andes form a semicircle to the east, significantly preventing the interactions between the Amazon and Pacific Ocean and allowing more efficient communication only with the Orinoco Basin towards the northwest and the La Plata Basin towards the south. As a result, humid air is transported from the Atlantic Ocean to the Amazon through trade winds, condensing in the Basin and evaporating due to the daytime surface heating, ultimately resulting in water recycling in the region (SALATI *et al.*, 1979; NOBRE;

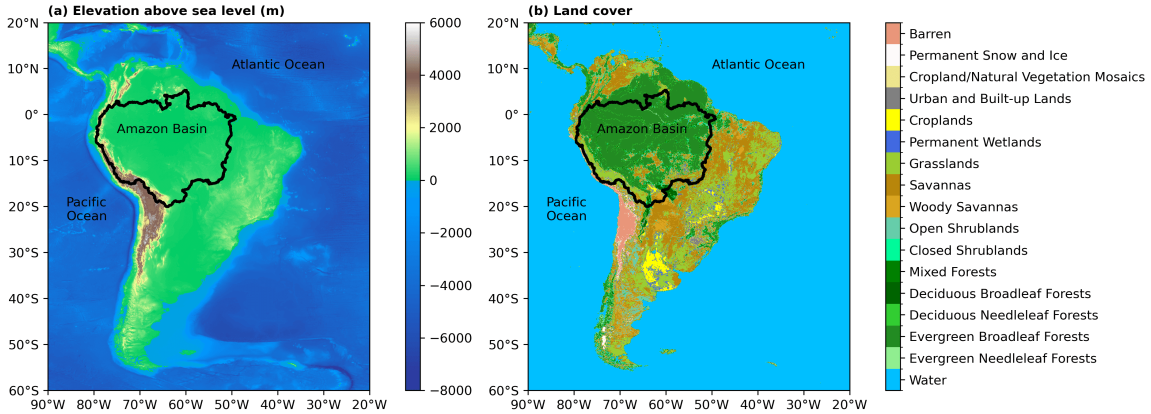

Figure 4.1 – Synoptic perspective of South America. (a) Land topography and Ocean depth (NOAA National Centers for Environmental Information, 2022). (b) Land cover for 2020 based on the Moderate Resolution Imaging Spectroradiometer (MODIS) - International Geosphere-Biosphere Programme (IGBP) land cover classification system. Amazon Basin contour is provided by MAYORGA *et al.* (2012).

MARENGO; ARTAXO, 2009). This keeps the air humid, which allows moisture to be transported outside the basin, feeding precipitation in other regions (ARRAUT *et al.*, 2012). In the Eastern Basin, the Andes cause orographic lift, resulting in precipitation throughout the year, accumulating more than 3000 mm (FIGUEROA; NOBRE, 1990; NOBRE *et al.*, 2009).

The Amazon climate also shows essential changes in space and time. The spatial variations are associated with the Amazon extension, which spreads from the South (18°) to the North (5°) Hemisphere, resulting in contrasting heating patterns and surface heterogeneity (FITZJARRALD *et al.*, 2008; BETTS *et al.*, 2009; SILVA *et al.*, 2011). The land cover (Figure 4.1b) in most of the central and northwest parts of the Amazon Basin are forests, while in the southern and eastern parts predominates deforested areas, savannas, and croplands used in agricultural activities (STEEGE *et al.*, 2013). The temporal variations are associated essentially with the sea surface temperature in the Atlantic and Pacific Oceans close to the Equator (NOBRE; MARENGO; ARTAXO, 2009; NOBRE *et al.*, 2009). The 30–60-day oscillations (also known as Madden–Julian oscillation, MO; KOUSKY; MADDEN; JULIAN 1993, 1994) provide intraseasonal variabilities, the South American monsoon system (CARVALHO *et al.*, 2010) controls the seasonality (transition between wet and dry season), and the El Niño–Southern Oscillation (RAO; CAVALCANTI; HADA, 1996; ZHANG; LIN, 1997) is associated with interannual changes. Anomalies in the sea surface temperature control the variability for longer timescales, such as the interdecadal, which is associated with the Pacific Decadal Oscillation (NEWMAN *et al.*, 2016) and the Atlantic Multidecadal Oscillation (KERR, 2000; KNIGHT; FOLLAND; SCAIFE, 2006).

## 4.2 GoAmazon2014/5 Experiment

The GoAmazon2014/5 (MARTIN *et al.*, 2016; MARTIN *et al.*, 2017) experiment was held from January 2014 to December 2015 in the central Amazon, in and around Manaus, a city surrounded by 1500 km of primarily pristine forest in all directions (Figure 4.2). It aimed at improving our knowledge about aerosols, clouds, precipitation, and their interactions over the Earth's largest tropical rainforest in the proximity of a large urban area producing air pollution. The GoAmazon2014/5 experiment is the result of international cooperation between Brazil, Germany, and the United States, which employed unprecedented surface instrumentation distributed in nine ground sites. Two aircraft were also used during the Intensive Operating Periods (IOP1 from 1 February to 31 March 2014 and IOP2 from 15 August to 15 October 2014) to survey the environs of Manaus. This study focuses on the region around the most instrumented site, T3, located 70 km downwind of Manaus, in Manacapuru (3.21°S, 60.60°W), where the ARM Mobile Facility 1 (AMF-1) and the ARM Mobile Aerosol Observing System (MAOS) were deployed. The T3 site is characterized by pasture vegetation surrounded by forest and nearby the intersection of the Solimões and Negro rivers (Figure 4.2b). In addition, we also used data from the S-band radar operated by the Amazon Protection System (Sistema de Proteção da Amazônia, SIPAM) located at the T1 site (3.15°S, 59.99°W) in Manaus. A detailed description of all sites can be found in MARTIN *et al.* (2016).

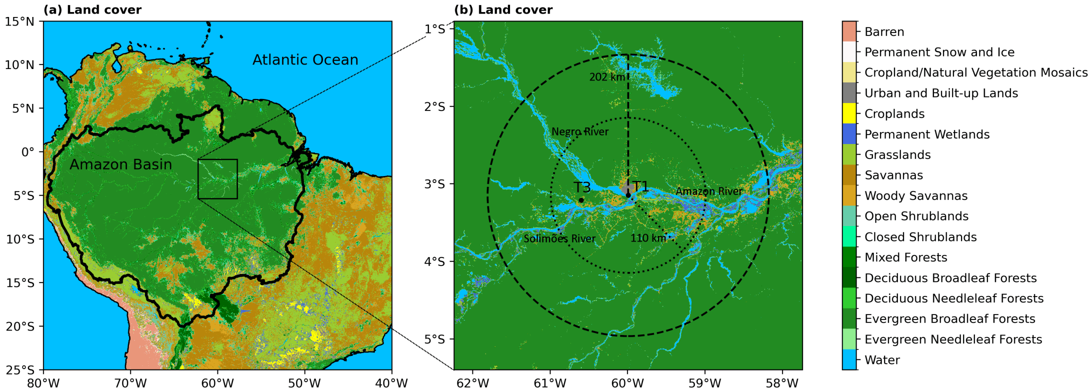

Figure 4.2 – Land cover distribution (a) in South America and (b) around the GoAmazon2014/5 sites. The dashed circle with a radius of 202 km centered at the T1 site (in Manaus) corresponds to the S-band radar domain. The dotted circle with a radius of 110 km shows the domain of the large-scale forcing developed for the GoAmazon2014/5 Experiment (TANG *et al.*, 2016). We also indicate the Amazon, Solimões, and Negro Rivers on the map. Land cover is from 2014, based on the Moderate Resolution Imaging Spectroradiometer (MODIS) - International Geosphere-Biosphere Programme (IGBP) land cover classification system. Amazon Basin contour is provided by MAYORGA *et al.* (2012).

## 4.3 Instrumentation

The observational data for the GoAmazon2014/5 experiment can be found in ARM's data discovery platform[1]. Here we describe the instrumentation associated with the data used in this project.

### 4.3.1 Cloud and Precipitation Properties

The W-band ARM Cloud Radar (WACR) systems are vertically-pointing Doppler radars that probe the extent and composition of clouds at 95.04 GHz (wavelength 3.16 mm) (ARM, 2014k). WACR is mainly used to determine the cloud boundaries, i.e., cloud base and top, for the different cloud layers in a vertical column with a temporal resolution of 2 s, a vertical resolution of 30 m, and covering altitudes up to 15 km. WACR measurements suit fair weather conditions, while the W-band signal is attenuated under rainy conditions.

The Radar Wind Profiler (RWP) operates at 1290-MHz (wavelength 23.2 cm) with a beam bandwidth resolution of 8° and temporal resolution of 6 s (ARM, 2014i). RWP operates through the wind mode or precipitation mode. We are mainly interested in the precipitation mode, which samples precipitation ranging up to 16 km. Thus, it provides measurements of the precipitation echo top, a sub-estimative of the cloud top, which is suitable during precipitation events when the WACR signal is attenuated (GIANGRANDE *et al.*, 2017).

Cloud base height is best measured by the return signal of lidars. Here we use the ceilometer (CEIL), Vaisala CL51, which operates at a wavelength of 905 nm (ARM, 2014d). This instrument measures the cloud base from up to three cloud layers with a temporal resolution of 15 s, a vertical resolution of 30 m, and covering altitudes up to 7700 m. We also use data from the micropulse lidar (MPL), which has dual polarization and operates at a wavelength of 532 nm (ARM, 2014f). The MPL is used here for real-time detection of clouds (base), but it can also provide information on the vertical profile of aerosol backscatter and distinguish the phase of hydrometeors. It has a temporal resolution of 10 s, a vertical resolution of 15 m, and covers altitudes ranging from $\sim$ 150 to 18000 m.

The Amazon Protection System in Brazil (Sistema de Proteção da Amazônia, SIPAM) operates an S-band (10 cm), Doppler, single-polarization scanning radar south of downtown Manaus. The S-band radar provides 12-minute measurements of reflectivity covering a region of 202 km in radius centered at the T1 site (Figure 4.2b). It has a horizontal resolution of 2 km and a vertical resolution of 500 m, which covers altitudes from 0.5 to 20 km (SCHUMACHER; FUNK, 2018b). The surface precipitation rate is

---

[1] Data access: https://www.arm.gov/research/campaigns/amf2014goamazon.

derived from the reflectivity of a constant altitude plan position indicator (CAPPI) at 2.5 km, calibrated with surface measurements from a Joss-Waldvogel disdrometer located at the T3 site during the wet season of early 2014 (SCHUMACHER; FUNK, 2018a).

### 4.3.2 Surface Meteorology

The ARM Surface Meteorology Systems (MET) provides 1-minute statistics of surface wind speed, wind direction, air temperature, relative humidity, pressure, and precipitation rate (ARM, 2014j). The AMF-1 sensors correspond to an RM Young 05106, which measures wind at 10 m; a Vaisala HMP45D, which measures temperature and relative humidity at 2 m; a Vaisala PTB220, which measures pressure at 1 m; and a Vaisala PWD22 and Optical Sci ORG 815, which measures surface precipitation.

In addition to the MET station, the Aerosol Observing System Surface Meteorology (AOSMET) also provides standard meteorological measurements of the ambient temperature, pressure, relative humidity, and wind speed and direction (ARM, 2013b). While the primary intent of the AOSMET data is for analyzing AOS instrument data, it can also be applied in various other analyses. In particular, for local measurements of surface precipitation rate, we use data from the AOSMET instead of the MET. The AOSMET measurements of surface precipitation are carried out using the acoustic gauge of a Vaisala WXT520. The data are provided at 1-second intervals and do not contain any quality flags.

### 4.3.3 Surface Fluxes

The evolution of the Boundary Layer, including the convective layer, is driven primarily by the surface fluxes. To characterize these fluxes, we use a combination of different instruments.

The eddy correlation (ECOR) flux measurement system provides 30-minute measurements of the surface turbulent fluxes of momentum, sensible heat, latent heat, and carbon dioxide (ARM, 2014e). The ECOR uses the eddy covariance technique, which uses the correlation between wind, temperature, and water vapor and $CO_2$ densities. The QCECOR (Quality Controlled ECOR) offers surface latent and sensible fluxes that include additional improvements (ARM, 2014h).

The Sky Radiation (SKYRAD) radiometers provide 1-minute measurements of shortwave (solar) and longwave (infrared) broadband downwelling irradiances, while the Ground Radiation (GNDRAD) radiometers provide 1-minute measurements of the upwelling components (ARM, 2013a).

### 4.3.4 Atmosphere State

The thermodynamic profile is key to understanding the environment where convection is developing, as it provides information on planetary boundary layer, atmospheric instability, and moisture availability, to mention a few key parameters.

The balloon-borne sounding system (SONDE) measures the thermodynamic state periodically every 6 hr (ARM, 2014c). Thus, a vertical profile of wind speed, wind direction, air temperature, relative humidity, and pressure is available at 02:00, 08:00, 14:00, and 20:00 Local Standard Time (LST). During the IOP1 and IOP2, one additional radiosonde launch is also available at 11:00 LST. In addition, we also use the planetary boundary layer height (PBLHT) VAP developed from the SONDE data (ARM, 2014g). The PBLHTSONDE provides four PBL estimates, one based on the method of Heffter (1980), Liu and Liang (2010), and the bulk Richardson number using a critical threshold of 0.25 or 0.50 (AMS/APCA. . . , 1980; LIU; LIANG, 2010; SØRENSEN *et al.*, 1998).

## 4.4 Soil and Land Properties

The surface-land characteristics informed by satellite measurements and in-situ measurements of soil properties are essential to configure the Surface Land Model in the modeling study (Chapter 6).

The Moderate Resolution Imaging Spectroradiometer (MODIS) provides data products of land cover type (MCD12Q1 Version 6) and leaf area index (MCD15A2H Version 6.1) (FRIEDL *et al.*, 2010). Specifically, we use the land cover product based on the International Geosphere-Biosphere Programme (IGBP) land cover classification system. Silt, clay, and sand content in the soil are based on in-situ measurements of the soil type “Terra Firme" (Terra-firma) described in Table 1 on SCHAEFER *et al.* (2017). Soil temperature and wetness are based on the NASA Global Land Data Assimilation System (GLDAS) Noah Land Surface Model L4 3 hourly 0.25 x 0.25 degree V2.1 (RODELL *et al.*, 2004).

## 4.5 Large-Scale Fields

Large-scale fields refer to meteorological data that describe the state of the atmosphere from a broad horizontal perspective, from mesoscale ($\sim$ 100 km) to synoptic scale ($\sim$ 1000 km). An illustration of this can be seen with the S-band radar, which provides precipitation over a domain of $\pi(202 \text{ km})^2$. The average precipitation across this domain represents a large-scale precipitation field. However, large-scale fields are typically obtained using an atmospheric model and data assimilation, and they are utilized in both observational (ITTERLY; TAYLOR; DODSON, 2018) and modeling studies (RANDALL *et al.*, 1996; KHAIROUTDINOV; RANDALL, 2006; GENTINE *et al.*, 2016).

The European Centre for Medium-Range Weather Forecasts (ECMWF) performs global atmospheric predictions on various timescales, leveraging an advanced data assimilation system. The ECMWF also conducts retrospective analyses, known as reanalysis, which involves using the latest version of the atmospheric model and data assimilation to reprocess past observations. Its primary objective is to faithfully reproduce measured data from past observations using a procedure consistent with the physical conservation laws governing atmospheric dynamics (DEE *et al.*, 2009).

The constrained variational analysis (VARANAL) method is described by ZHANG; LIN; ZHANG *et al.* (1997, 2001). The availability of surface pressure, sensible heat flux, latent heat flux, precipitation, wind stress, and radiative flux measurements enables the assessment of the accuracy of vertical velocity and advective tendencies through the examination of column-integrated budgets of mass, heat, moisture, and momentum. Due to the inherent uncertainties in atmospheric measurements, wind divergence calculated based on sounding measurements often fails to satisfy mass conservation. Thus, the variational analysis involves adjusting the observed variables to fulfill the vertically integrated constraints outlined below:

$$\langle \nabla \cdot \mathbf{V} \rangle = -\frac{1}{g p_s} \frac{d p_s}{dt} \,, \tag{4.1}$$

$$\frac{\partial \langle r_v \rangle}{\partial t} + \langle \nabla \cdot \mathbf{V} r_v \rangle = \mathrm{EVAP} - \mathrm{PREC} - \frac{\partial \langle r_l \rangle}{\partial t} \,, \tag{4.2}$$

$$\frac{\partial \langle s \rangle}{\partial t} + \langle \nabla \cdot \mathbf{V} s \rangle = R_{\mathrm{TOA}} - R_{\mathrm{SFC}} + L\,\mathrm{PREC} + \mathrm{H} + \frac{\partial \langle r_l \rangle}{\partial t} \,, \tag{4.3}$$

$$\frac{\partial \langle \mathbf{V} \rangle}{\partial t} + \langle \nabla \cdot \mathbf{V} \mathbf{V} \rangle - f \mathbf{k} \times \langle \mathbf{V} \rangle - \nabla \langle \phi \rangle = \tau_s \,, \tag{4.4}$$

where the bracket represents vertical integration, $\mathbf{V}$ is the wind, $r_v$ is the water vapor mixing ratio, $s = C_p T + gz$ is the dry static energy, and $p_s$ is the surface pressure. Here, $R$ is the net downward radiative flux at the top of the atmosphere (TOA) and at the surface (SFC), $\tau_s$ is the surface wind stress, PREC is the precipitation, $H$ is the sensible heat flux, EVAP is the surface evaporation, and $r_l$ is the cloud liquid water content. The adjustment is accomplished through the minimization of the cost function:

$$\iiint_{xyp} \left[ \alpha_u \left( u^* - u_o \right)^2 + \alpha_v \left( v^* - v_o \right)^2 + \alpha_s \left( s^* - s_o \right)^2 + \alpha_{r_v} \left( r_v^* - r_{vo} \right)^2 \right] dx\, dy\, dp \,, \tag{4.5}$$

where subscript $o$ represents the analysis based on the initial state, superscript * denotes the final analysis, and the $\alpha$'s refer to the prescribed weighting functions. The resulting large-scale forcing terms and evaluation fields are valuable for various applications, including observational studies, driving and evaluating single-column models, cloud-resolving models, and large-eddy simulations.

We use the large-scale fields developed by TANG *et al.* (2016), specifically for the GoAmazon2014/5 experiment using the VARANAL technique. Due to the unavailability of a suitable sounding array to capture the divergence and advection fields during the GoAmazon2014/5 campaign, data from the ECMWF ERA-Interim reanalysis (DEE *et al.*, 2011) were used by the dataset developers as a first guess of the atmospheric state. Then, they were mainly constrained by the SIPAM S-band radar precipitation rate and ARM surface fluxes through the column heat (4.3) and moisture (4.2) budget analysis. The resulting large-scale fields represent an average over the analysis domain centered at the T1 site in Manaus, with a radius of 110 km (Figure 4.2b).

## 4.6 System for Atmospheric Modeling (SAM)

We use the System for Atmospheric Modeling version 6.11.8 (SAM 6.11.8), which is a cloud-resolving model (CRM) (KHAIROUTDINOV; RANDALL, 2003). SAM solves the anelastic equations of motion and uses liquid water static energy, total nonprecipitating (vapor and cloud), and precipitating water as thermodynamic prognostic variables. The equations are solved using lateral periodic boundary conditions. A prognostic turbulent kinetic energy (TKE) 1.5-order closure scheme is used to parameterize subgrid-scale (SGS) effects. A bulk microphysics parameterization must be chosen, which includes the single-moment (MORRISON, 2003), double-moment (MORRISON; CURRY; KHVOROSTYANOV, 2005), and Predicted Particle Properties (P3) scheme (MORRISON; MILBRANDT, 2015). The radiative heating can be prescribed or calculated using a chosen radiation scheme, which includes the National Center for Atmospheric Research (NCAR) Community Atmosphere Model (CAM3) (COLLINS *et al.*, 2006) and Rapid Radiative Transfer Model (RRTM) (MLAWER *et al.*, 1997). The surface fluxes can be prescribed or calculated using the Monin-Obukhov similarity theory or a simplified Surface Land Model (SLM) (LEE; KHAIROUTDINOV, 2015), which is only compatible with the CAM3 radiation scheme for the current SAM-SLM version. The simplified SLM uses a minimalist set of parameters to solve the transport of heat, moisture, momentum, and radiation in the soil and vegetation. Consequentially, it provides a fair idealization of the land-atmosphere interactions responsible for the locally-driven STD convection transition, the topic of this project.

## 4.7 Computational Resources

We used the Mana[2] computational resources to conduct the numerical simulations in this project.

Mana is the University of Hawaiʻi (UH) high performance computing (HPC) cluster – a collection of many computers called nodes connected together with a network – that solves computational problems too large for standard computers. Mana is operated by UH Information Technology Service Cyberinfrastructure, that serves as a central university

---

[2] Mana General Information: https://datascience.hawaii.edu/hpc/.

Table 4.1 – Simulations for model validation during December 2014. Each case corresponds to a simulation designed to evaluate the model's sensitivity to changes in microphysics, horizontal resolution, or domain size. The columns show the output file sizes for model statistics (variables with domain and temporal averages) and instantaneous 2D and 3D fields, along with the real-time simulation duration. The simulations utilized 10 nodes, 400 CPUs, and approximately 10×180 GB of memory.

| Microphysics | Resolution (m) | Domain ($km^3$) | STAT (GB) | 2D (GB) | 3D (GB) | Elapsed time (hr) |
|---|---|---|---|---|---|---|
| Single-moment | 500 | 200x200x27 | 0.22 | 46.19 | 510.76 | 16.87 |
| Double-moment | 500 | 200x200x27 | 0.31 | 46.19 | 1097.23 | 24.54 |
| P3 | 500 | 200x200x27 | 0.27 | 46.19 | 1097.23 | 34.85 |
| P3 | 250 | 200x200x27 | 0.27 | 183.32 | 4388.45 | 208.55 |
| P3 | 500 | 400x400x27 | 0.27 | 183.32 | 4388.45 | 115.0 |
| Total | | | 1.32 | 505.20 | 11520.00 | 399.81 |

wide computational resource which supports data and computationally intensive research in over 90 disciplines. Mana consists of 347 nodes (8,680 cores) with a total of 58 TB of RAM, 120 GPUs and more than 1 PB of storage.

The numerical simulations for the modeling study (Chapter 6) were conducted using 10 nodes, 400 CPUs, and approximately 10×180 GB of memory. The model validation simulations cover December 2014, and their associated computational costs are detailed in Table 4.1. We conducted a series of simulations aimed at evaluating the model's sensitivity to microphysics. These assessments encompassed the single-moment, double-moment, and P3 schemes, utilizing a horizontal resolution of 500 m and a domain size of 200x200 $km^2$. The vertical resolution varies from a minimum of 50 m to a maximum of 500 m, covering 27 km and utilizing a total of 128 grid points. Additionally, we conducted a series of simulations to assess the model's sensitivity to changes in resolution and domain size. For this purpose, we employed the P3 microphysics scheme. In one scenario, we varied the resolution from 500 m to 250 m, and in another scenario, we modified the domain size from 200x200 $km^2$ to 400x400 $km^2$. The simulations addressing microphysics utilize a grid of 400x400x128 points, whereas the simulations designed to assess sensitivity to resolution or domain size employ a grid of 800x800x128 points. Since the P3 scheme is more comprehensive than the double-moment scheme, it also takes longer to simulate the same case, and the same argument also applies to the computational cost of the double- and single-moment schemes. The number of output variables also depends on the microphysics scheme, resulting in different filesizes of the statistics (STAT) and the 3D Fields depending on the scheme. However, this has a negligible impact on the total simulation time.

Note that the computational time also depends on the configuration of the nodes. The Slurm Workload Manager provides the resources for a given job only when all the

Table 4.2 – Simulations for sensitivity experiments. The rows correspond to various types of sensitivity experiments. The columns show the number of simulations conducted for each experiment, the output file sizes for model statistics and instantaneous 2D and 3D fields, along with the real-time duration for the total number of simulations. Each simulation was conducted using the P3 scheme, with a horizontal resolution of 500 m, a domain size of 200x200x27 km$^3$, and spanning a model-time period of 20 hours. The simulations utilized 10 nodes, 400 CPUs, and approximately 10×180 GB of memory.

| Experiment | cases (#) | STAT (GB) | 2D (GB) | 3D (GB) | Elapsed time (hr) |
|---|---|---|---|---|---|
| Deep control | 4 | 0.03 | 4.97 | 117.98 | 5.70 |
| ShCu control | 4 | 0.03 | 4.97 | 117.98 | 4.54 |
| Low-Level Moisture | 12 | 0.09 | 14.90 | 353.95 | 8.07 |
| Free Troposphere Moisture | 12 | 0.09 | 14.90 | 353.95 | 14.29 |
| Horizontal Advection | 8 | 0.06 | 9.93 | 235.96 | 7.56 |
| Vertical Advection | 8 | 0.06 | 9.93 | 235.96 | 7.58 |
| Jet - Deep control | 4 | 0.03 | 4.97 | 117.98 | 6.20 |
| Jet - ShCu control | 4 | 0.03 | 4.97 | 117.98 | 4.95 |
| Low-Level Jet | 32 | 0.23 | 39.73 | 943.86 | 36.84 |
| Upper-Level Jet | 16 | 0.11 | 19.87 | 471.93 | 17.97 |
| Total | 104 | 0.74 | 129.13 | 3067.54 | 113.70 |

requested resources are free to be used. However, the specific nodes used vary for each simulation, affecting the model performance. Thus, the computational time will differ even if we run two identical simulations.

Table 4.2 presents the computational cost of each sensitivity experiment. These experiments were conducted using the P3 scheme, with a horizontal resolution of 500 m and a domain size of 200x200x27 km$^3$. We conducted 104 simulations for the sensitivity experiment study, where each simulation lasted 20 hours (from 02 to 22 LST), totaling 113.70 hours of computational time. The details of each simulation are given later in Chapter 6. Since the deep (Deep) convective days use ice microphysics more extensively, their computational cost is higher than shallow cumulus (ShCu) days. Finally, while it may appear that only three weeks of computational time were utilized for this project, numerous additional simulations were performed before arriving at this definitive collection of cases. For example, we dedicated around a year to the learning process and fine-tuning of the model setup. This comprehensive effort involved addressing a few bugs in the Surface Land Model, which had been implemented by the model owner within the SAM version 6.11.8.

# 5 EVALUATING THE ENVIRONMENTAL CONTROLS ON ISOLATED CONVECTION IN THE GOAMAZON2014/5 OBSERVATIONS

This chapter presents our observational study of convection and precipitation in the central Amazon. We focus on the wet season (December to April) and employ data from the GoAmazon2014/5 campaign. Days are classified into three convective cloud regimes (shallow cumulus, congestus, and deep convection), which are contrasted to help infer the relative importance of moisture, convective instability, surface properties, and vertical wind shear in promoting the STD convection transition and enhancing precipitation.

We organize this chapter as follows: Section 5.1 describes the data and the cloud convective regime classification. A comparison of clouds and precipitation properties among the shallow, congestus, and deep days is given in section 5.2. The analysis of the diurnal cycle and the evaluation of the environmental conditions associated with each convective regime are described in section 5.3. The analysis of conditionally averaged precipitation as a function of critical factors controlling the development of convection is presented in section 5.4. Section 5.5 discusses the results. Section 5.6 gives the preliminary conclusions.

## 5.1 Observational Data and Methods

An overview of the GoAmazon2014/5 experiment (section 4.2), the essential instrumentation used in our study (section 4.3), and a summary of the large-scale fields (section 4.5) are presented in Chapter 4. The following section describes the specific experimental and large-scale data used here, the observational study, as well as the statistical procedures applied to each dataset, the additional derived variables, and the cloud convective regime classification.

### 5.1.1 Experimental and Large-Scale Data

The Merged RWP-WACR-ARSCL Cloud Mask dataset combines the Radar Wind Profiler (RWP) data with the original W-band Cloud Radar (WACR) Active Remote Sensing of Cloud (ARSCL) Value-added product (VAP). For our convective regime classification, described in the next section, we used the cloud mask time-height profiles of cloud location (GIANGRANDE *et al.*, 2017; FENG; GIANGRANDE, 2018). Three types of convective clouds are defined: shallow cumulus, with a base and cloud top below 3 km; congestus, with a base below 3 km and a top between 3-8 km; and deep convection, with a base below 3 km and a top $>$ 8 km. From the cloud mask, available every 30 s, we compute the cloud frequency profile (regardless of the cloud type) in 12 min windows to match the S-band radar data.

We use the 12-min S-band reflectivity profiles to assess rain coverage in our analysis domain, 100x100 km$^2$ centered at T3 site, calculated using a reflectivity threshold of 20 dBZ as in ZHUANG *et al.* (2017). We also use the surface precipitation rate derived from the reflectivity of a constant altitude plan position indicator (CAPPI) at 2.5 km. In the examination of precipitation properties (section 5.2), the precipitation rate is averaged across the analysis domain (100 x 100 km centered at the T3 site). Furthermore, in the study of conditionally averaged precipitation (section 5.4), an additional averaging from 14 to 20 LST is considered alongside the domain average.

Figure 5.1 shows the map of S-band precipitation averaged over the wet season (December to April) 2014-2015. The precipitation statistics indicate that some radar beams are partially blocked. We used a threshold of 4 mm day$^{-1}$ to roughly identify these problematic regions. Beam blockage only affects 7 pixels out of 2,601 in our analysis domain, corresponding to only 0.3 %, with no relevant sensitivity to the threshold choice. Although this contribution is negligible, we still removed these blocked pixels from our analysis.

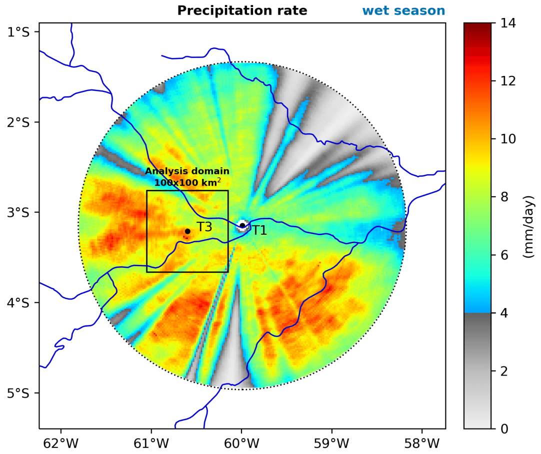

Figure 5.1 – Map of precipitation rate at 2.5 km height averaged over the wet season (December to April) 2014-2015. The square box represents the analysis domain covering an area of 100x100 km$^2$ centered at the T3 site. The dotted circle (radius of 202 km) centered over the T1 site describe the S-band radar domain with available measurements.

We use the SONDE data from the regular time launches (02, 08, 14, and 20 LST). The additional 11 LST sounding is not available during the wet season, defined here to be December-April. Moreover, we only analyze soundings that extend from the surface to at least 8 km, and we linearly interpolate the profiles to a fixed 50 m vertical grid.

Based on the SONDE data, we also use the planetary boundary layer derived from the profile of the bulk Richardson number using a critical threshold of 0.25 (PBLHTSONDE). In addition, we calculated additional variables from the thermodynamic profiles. Total CWV is determined by integrating the mixing ratio from the surface to 200 hPa. Similarly, the partially-integrated CWV was calculated for the layers 1000-700 hPa ($\sim$ 0-3 km, $\mathrm{CWV}_{\mathrm{low}}$) and 700-200 hPa ($\sim$ 3-12 km, $\mathrm{CWV}_{\mathrm{mid}}$)[1], representative of the low- and mid-troposphere, respectively. The convective instability indices of Lifting Condensation Level (LCL), Level of Free Convection (LFC), Convective Inhibition (CIN), and Convective Available Potential Energy (CAPE) are also calculated. The air parcel is lifted up dry adiabatically to the Lifting Condensation Level (LCL), then moist adiabatically from there. We use the most unstable parcel, based on the maximum equivalent potential temperature in the lowest 300-hPa layer, and the mixed-layer parcel, where we consider the layers of 100, 50, 25, and 10-hPa (STULL, 2016).

The surface meteorological conditions are analyzed through the MET station data. We use a 30-min average of temperature, relative humidity, wind speed, and wind direction. The water vapor mixing ratio is also computed.

The energy and moisture balances at the surface are characterized by a combination of different instruments. The ECOR Flux Measurement provides 30-min data of surface sensible and latent heat fluxes, although we use the hourly average from the ARM best-estimate (ARM, 2014a). SKYRAD and GNDRAD radiometers provide surface radiation fluxes, although we also use the hourly average from the ARM best-estimate (ARM, 2014b). The ground heat flux, $G$, is estimated using the following equation:

$$G = SW - LW - H - LE, \tag{5.1}$$

where, $SW$ is the net shortwave flux, $LW$ net longwave flux, $H$ the sensible heat flux, and $LE$ the latent heat flux.

The water balance analysis uses the AOSMET precipitation, ECOR latent heat flux, and SONDE CWV. For this purpose, the AOSMET and ECOR data are averaged over 6 hours to match the SONDE timescale.

We analyze the wind profile and bulk vertical wind shear using the large-scale horizontal wind based on the Constrained Variational Analysis (VARANAL) developed for the GoAmazon2014/5 experiment (TANG *et al.*, 2016).

### 5.1.2 Convective Regime Classification

We defined the wet season as the period from December to April, which matches previous studies in the Central Amazon (MACHADO *et al.*, 2004; MARENGO *et al.*, 2013). To contrast the different atmospheric conditions that lead to different convective regimes, we applied a classification criterion that identifies shallow, congestus, or deep

---

[1] While we employ the subscript “mid”, it is worth noting that water vapor is integrated from the mid to upper levels. However, as shown in Figure 5.6, the contribution of the upper levels to CWV is minimal. Hence, we adopt this simplified notation for the sake of convenience.

days. Given our interest in convection that develops in response to the daytime surface heating, days with propagating mesoscale convective systems (MCS) were excluded from our analysis.

Our regime classification is based on the criteria proposed by ZHUANG *et al.* (2017) and TIAN *et al.* (2021). Firstly, we consider the diurnal period between 10-20 LST. We then define three categories of convective regimes: shallow cumulus, congestus, and deep, based on the maximum development of convective clouds during the diurnal cycle. The cloud mask from the RWP-WACR-ARSCL is used to identify cloud development throughout each day. In addition, we also use the rain coverage from the S-band radar to estimate the cloud development based on the echo cloud top. The rain coverage is calculated as the fraction of reflectivity pixels $>$ 20 dBZ (see section 5.1.1). The echo-top is defined as the highest level where the rain coverage is greater than 2 %. The quantitative criteria are enumerated below:

i) Shallow convective days (ShCu): (1) The cloud mask does not show any congestus and deep clouds during the diurnal cycle (10-20 LST). (2) Precipitation above 3 km of altitude must be $<$ 2 % in the analysis domain (100x100 km$^2$, centered at T3).

ii) Congestus convective days (Cong): (1) The cloud mask indicates congestus clouds during the diurnal cycle, but none of them develops into deep clouds. (2) Precipitation above 8 km (between 3-8 km) of altitude must be $<$ 2 % ($>$ 2 %) in the analysis domain.

iii) Deep convective days (Deep): (1) The cloud mask indicates deep convection during the diurnal cycle. (2) Precipitation above 8 km $>$ 2 % in the analysis domain.

iv) Early morning perturbation: For the 06-10 LST period, we require that no congestus and deep clouds be observed.

v) Local convection: No convective system with a contiguous area of precipitation $>$ 10,000 km$^2$ reaches the analysis domain between 06-20 LST.

Figures 5.2 and 5.3 illustrate the classification criteria for the convective regime and convective system, respectively. The classification essentially depends on the cloud evolution during the diurnal cycle. The exclusion of any relevant early morning perturbation (06-10 LST) guarantees that nighttime MCSs do not influence the diurnal cycle. Moreover, our condition of isolated convection ensures that diurnal convection occurs on a scale much smaller than those of MCSs, typically defined by a 100 km threshold (HOUZE Jr., 2004). Note in Figure 5.2e, illustrating a day identified as a Deep regime, that convection remains shallow during the afternoon until 16 LST. It then rapidly evolves from congestus to cumulonimbus within a few minutes. The observed deepening of convection

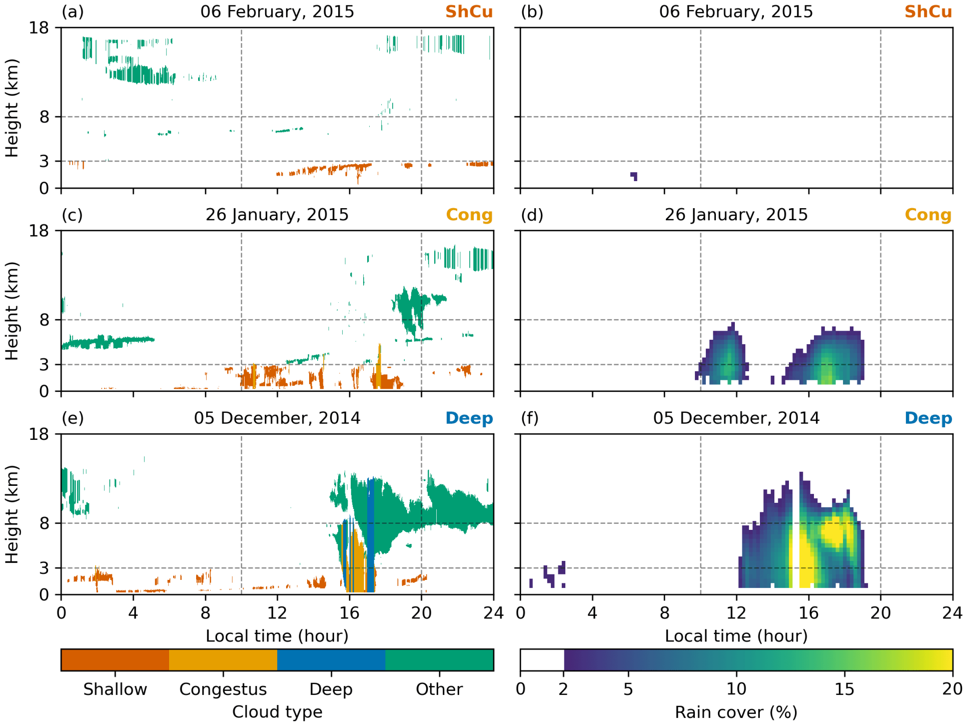

Figure 5.2 – Cloud mask (left) and precipitation coverage (right) for examples of days classified as shallow (a-b), congestus (c-d), and deep (e-f).

during the day is driven by the diurnal cycle of surface heating. Therefore, the Deep regime represents days exhibiting the STD transition in the Amazon.

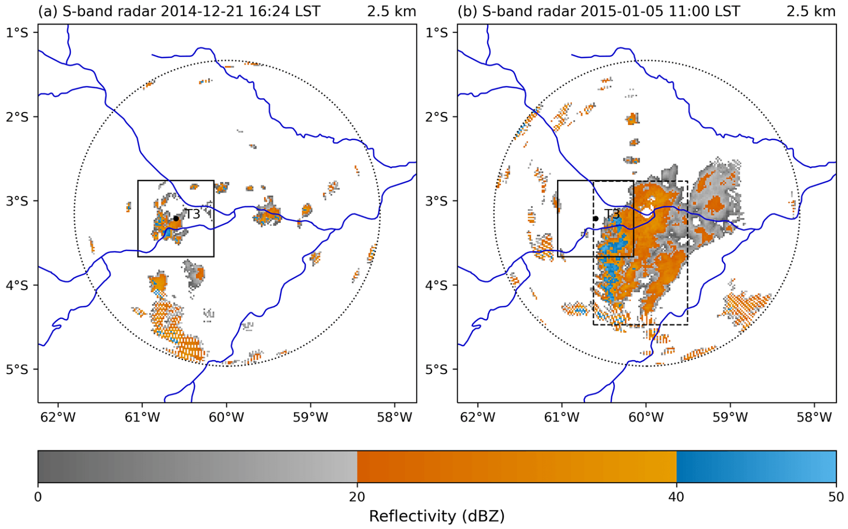

Figure 5.3 – Convective system. (a) Scattered local system. (b) Non-local propagating system. The dashed black box illustrates the region with a contiguous area of precipitation (> 20 dBZ) not fulfilling the local convection requirement.

The number of days categorized using the above criteria for the wet season (blue) and the dry season (red) is shown in Figure 5.4. Deep convection appears to be the dominant category in both seasons, although the convective systems tend to be larger during the wet season. Specifically, we identified 16 days for ShCu regime, 27 days for Cong regime, 60 days for Deep regime, and 111 days for non-local, deep convection. Here, we are interested only in the local shallow-to-deep transition mechanism during the wet season. Hence, the results presented in the next section refer only to those 103 days.

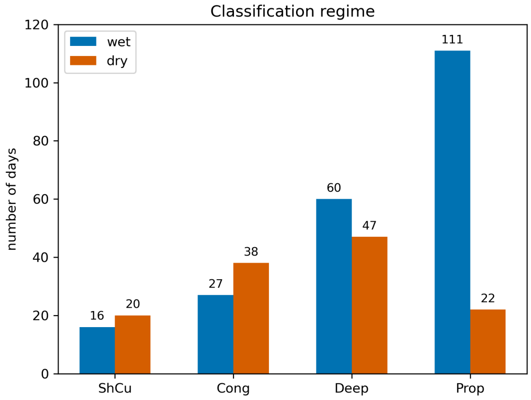

Figure 5.4 – Number of days classified in each convective regime during the wet (Dec-Apr) and the dry (Jun-Aug) seasons, from 2014 to 2015. Propagating (Prop) days refer to non-local deep convection, with the early morning perturbation condition being ignored.

## 5.2 Cloud and Precipitation Properties

The composite diurnal cycles of the vertical cloud frequency profiles and rain coverage for the different convective regimes are shown in Figure 5.5. The red line on the rain coverage panels is the precipitation rate. For all convective regimes, daytime convection is usually preceded by some cloud activity at night, with some clouds occurring at all levels.

The ShCu regime has a more scattered cloud frequency during the daytime (Figure 5.5a). Low-level clouds dominate the diurnal cycle, with a peak reaching 54% at 1.43 km around 13 LST. After 17 LST, cirrus clouds also contribute to the cloud frequency composite. There is some precipitation around 19 LST when the rain is about $\sim$ 1%. As for the other regimes, there is some stratiform precipitation from 00-04 LST during the preceding night.

The Cong regime also shows higher cloud frequency below 3 km during the diurnal cycle (Figure 5.5c). The maximum cloud cover is 50% at 1.04 km around 12 LST, earlier and lower than observed for the ShCu regime. Between 3-8 km, the cloud frequency composite has values under 5% but the rain composite shows a distinct behavior at mid-levels, with a rain coverage of 1-2% (Figure 5.5d). After the diurnal cycle, the rain coverage composite indicates that congestus clouds may evolve into a deeper phase. We identified

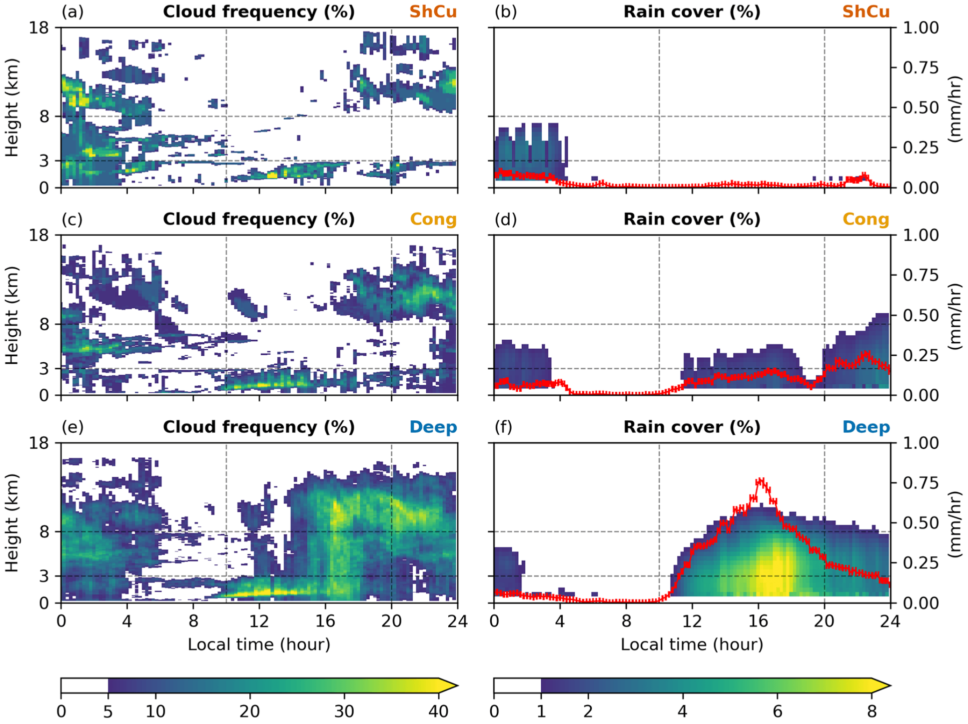

Figure 5.5 – Cloud mask (left) and precipitation (right) for the wet season (Dec-Apr) composites of days classified as shallow (a-b, N=16), congestus (c-d, N=27), and deep (e-f, N=60). The red line on the rain coverage panels is the precipitation rate (mm/hr).

7 cases (26%) in which congestus days fulfilled the Deep criteria (echo top above 8 km) after the diurnal cycle.

The Deep regime shows a more coherent cloud frequency profile, possibly associated with more extensive and longer-lived clouds during daylight hours. The maximum Deep cloud frequency is also associated with shallow clouds, being 49% at 0.92 km around 11:30 LST. Thus, the most developed convective regimes typically experience early shallow development with a lower cloud base. As the daytime progresses, the Deep cloud frequency also increases throughout the troposphere, with cloud top reaching up to 16 km. After cumulonimbus dissipation (around 18 LST), its anvil structure remains and may become a cirrus cloud formation that may contribute to the cloud cover of the next day. A substantial rain coverage is observed around 16-17 LST, with the domain average precipitation showing a maximum of 0.76 mm $\text{hr}^{-1}$ at 16 LST, being associated with the late afternoon STD transition in the Amazonian wet season.

## 5.3 Environmental Conditions

In this section, we specifically evaluate the environmental conditions that are characteristic of the STD convective transition. We analyze the local atmospheric conditions, convective instability, the surface balance of energy and moisture, and vertical wind shear conditions associated with shallow, congestus, and deep convective days. The error bars in each figure represent the standard deviation of the mean composite.

### 5.3.1 Atmospheric Conditions

Figure 5.6 shows the average vertical profiles of potential temperature (Figure 5.6a), $\theta$, and water vapor mixing ratio (Figure 5.6b), $r_v$, for each convective regime at 08 LST. The differences between the Deep and other convective regimes, $\Delta\theta$ and $\Delta r_v$, are shown in Figure 5.6c-d.

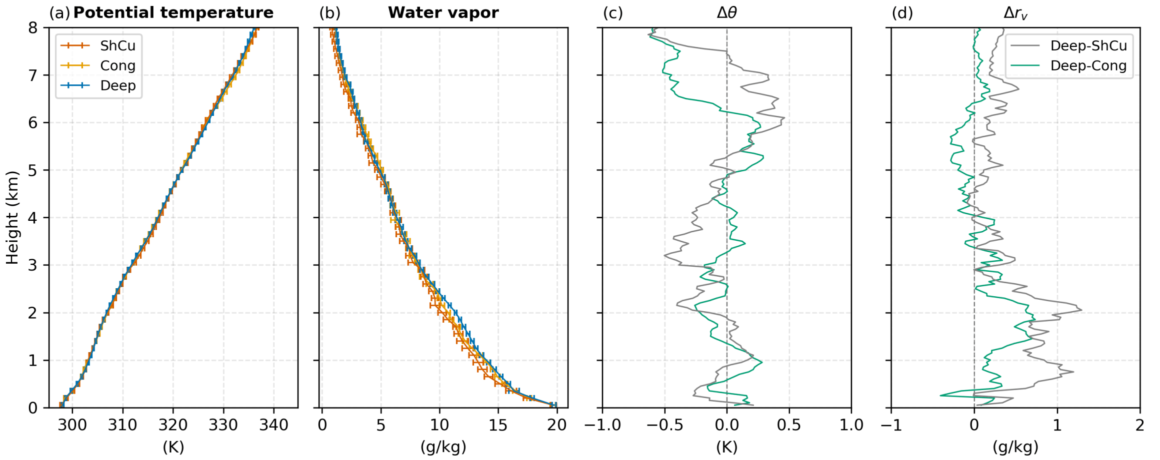

Figure 5.6 – Atmospheric conditions (a-b) and their convective regime anomalies (c-d). Results from the 08 LST radiosonde observations.

The potential temperature differences among the convective regimes are usually under 0.5 K below the 8 km level, which does not indicate a relevant relationship between daytime cloud development and the morning temperature profile. The Deep regime shows higher moisture content, particularly below 3 km. The most remarkable difference occurs around the 2 km level, with $\Delta r_v$ reaching 1.30 g kg$^{-1}$ and 0.74 g kg$^{-1}$ for Deep-ShCu and Deep-Cong, respectively. Above 3 km, the moisture profile for the Cong regime is quite similar to the Deep regime, with the Cong regime being even moister, for example, in the 5-6 km layer. The ShCu regime is only slightly drier than the Deep regime in that case. These results suggest that the importance of early morning preconditioning to the STD transition is restricted only to the lower levels.

Figure 5.7a shows the column water vapor (CWV) for each radiosonde time, while panels b-c show the partial contribution from the layers 1000-700 hPa ($\sim$ 0-3 km, CWV$_{\text{low}}$) and 700-200 hPa ($\sim$ 3-12 km, CWV$_{\text{mid}}$), representative of the low- and mid-troposphere, respectively. The ShCu regime shows the smaller CWV throughout the day for both low- and mid-levels. The Deep and ShCu difference ranges from 2.3 mm at nighttime to 5.1 mm at 14 LST. Interestingly, the CWV for Cong and Deep regimes are similar before the diurnal cycle starts, at 2 LST, but it is already greater for the Deep by 8 LST. The difference is maximum at 14 LST when it reaches 2.1 mm.

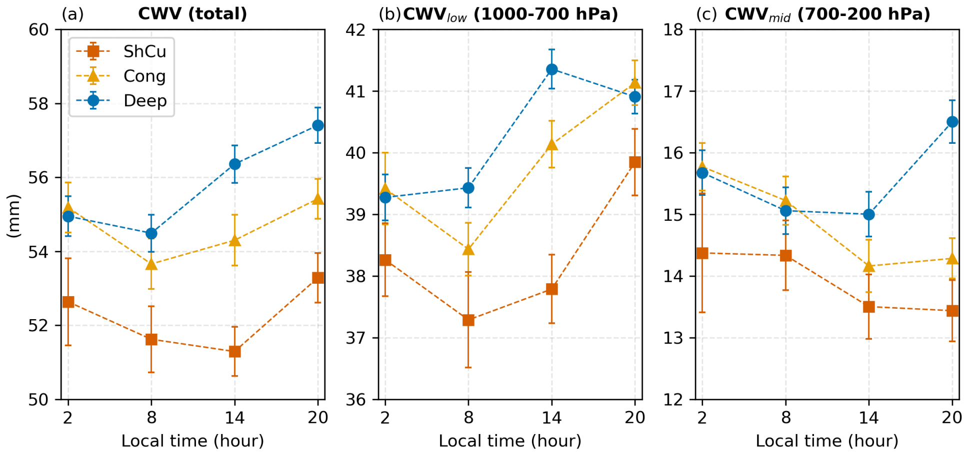

Figure 5.7 – Column water vapor: (a) total and its partial contribution in the (b) 1000-700 hPa layer and (c) 700-200 hPa layer.

The CWV$_{\text{low}}$ increases from 08 LST to 14 LST for all convective regimes, possibly due to evapotranspiration being the dominant moisture factor in that period. However, the CWV$_{\text{mid}}$ is essentially constant for the Deep regime in the 08-14 LST, while the ShCu and Cong regimes show a decrease of 0.83 and 1.06 mm, respectively. This indicates that ShCu and Cong regimes might be associated with large-scale subsidence, which would explain the drying of the mid-levels, and associated with low-level moisture divergence, which would explain the slower accumulation of moisture below 700 hPa despite slightly larger latent heat (see discussion in section 5.3.4).

### 5.3.2 Surface Meteorology

Figure 5.8 shows the surface meteorology composites. Surface meteorology exhibits a strong diurnal cycle; thus, surface temperature, moisture, and wind exhibit relevant differences for each convective regime only in the period ∼ 08-20 LST. The temperature is the same across all regimes before the start of the day (approximately 23.5 °C at 06 LT) and undergoes rapid growth as solar radiation begins to impact the surface (section 5.3.4). During the afternoon, around 13-15 LT, the surface temperature reaches its maximum, with lower values observed in more developed convective regimes (35.0 °C for ShCu regime, 33.4 °C for Cong regime, and 31.6 °C for Deep regime).

From nighttime to early morning (00-06 LST), the relative humidity (RH) is nearly 100%, while the mixing ratio ($r_v$) follows a decreasing pattern similar to the temperature curve for all convective regimes. Since $r_v$ is conserved and RH is already close to 100%, this suggests the possible formation of fog. After that, when the temperature increases due to solar heating, relative humidity drops, and eventually, fog rises and evaporates, giving place to fair weather cumuli. During the same period, the mixing ratio increases, possibly due to a combination of factors, including fog evaporation, surface evapotranspiration, and low-level convergence (see section 5.3.5). The most developed regimes exhibit higher

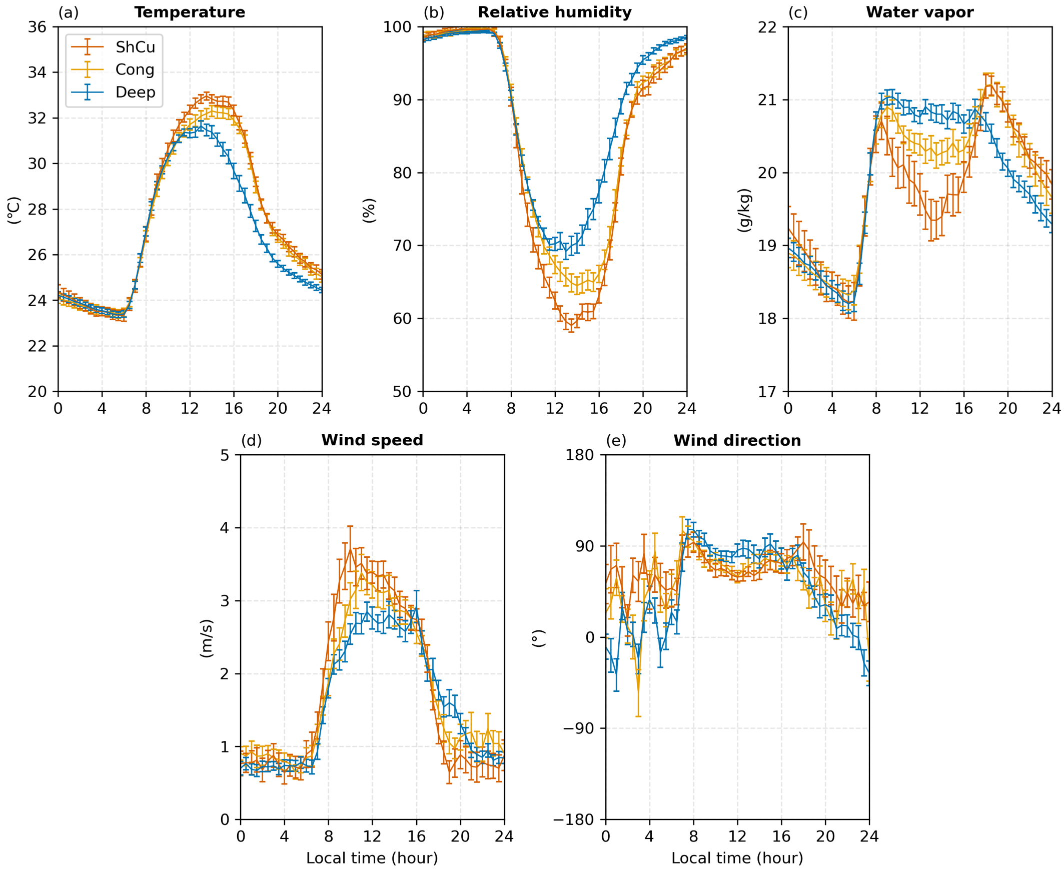

Figure 5.8 – Surface meteorology. (a) Temperature, (b) relative humidity, (c) water vapor mixing ratio, (d) wind speed, and (e) wind direction.

values in $r_v$ during the diurnal cycle (up to 18 LST) and lower temperatures, resulting in higher RH values in the afternoon. As we show later, evapotranspiration is similar among the convective regimes; thus, the low-level convergence plays a more vital role in sustaining the higher values in $r_v$ observed during Deep days. Around 17 LST, $r_v$ values during Deep days become lower than those in ShCu and Cong, because of the higher vertical transport and precipitation rates.

The surface wind during the night is weak ($\lesssim$ 1 m/s) due to the nighttime capping inversion and the stability of the nocturnal boundary layer. Vertical mixing becomes important with the diurnal cycle as the surface temperature increases and the boundary layer grows, which brings fast-moving air closer to the surface. The wind speed is higher in the ShCu regime (maximum of 3.71 m s$^{-1}$) and weaker in the Deep regime (maximum of 2.92 m s$^{-1}$) because of the difference in surface heating and boundary layer development between the regimes, discussed in the next section. The Cong regime shows an intermediate behavior (maximum of 3.38 m s$^{-1}$). During the diurnal cycle, the wind becomes predominantly easterly, in the same direction as the low-level jet above the boundary layer.

### 5.3.3 Boundary Layer Properties

The planetary boundary layer (PBL) height, the lifting condensation level (LCL), and the level of free convection (LFC) are shown in Figure 5.9. The convective indices are calculated using the 100-hPa mixed-layer parcel. The main difference between the convective regimes occurs during the diurnal cycle at 14 LST. The LCL is usually below the PBL height in the afternoon, indicating the entrainment zone on top of the convective mixed layer. Thus, the cloud base is about 300 m lower for the deep (1.09 km) than the shallow (1.37 km) regime. The LFC also tends to be below and closer to the PBL height and the LCL in the afternoon, although these parameters are considerably higher for ShCu days. The diurnal PBL height and convective indices for the Cong regime are similar to the Deep regime.

As the magnitude of convective indices depends on the idealization of the rising parcels, Appendix A shows the results for the comparison of PBL, LCL, and LFC heights, where LCL and LFC are calculated using the most unstable parcel (Figure A.1), 50-hPa mixed-layer parcel (Figure A.2), 25-hPa mixed-layer parcel (Figure A.3), and 10-hPa mixed-layer parcel (Figure A.4). Since the air parcel is lifted up dry adiabatically to the LCL, the parcel idealization provides little impact on the LCL magnitudes. Thus, LCL is essentially lower on Deep days and higher on ShCu days during the afternoon. On the other hand, the altitude of LFC is significantly sensitive to air parcel idealization. The qualitative behavior of the LFC is similar for the mixed-layer parcel using the 100-hPa, 50-hPa, and 25-hPa layers. In the case of a parcel using the 10-hPa layer, it is noted a large error bar in the Cong regime at 14 LST, where the mean LFC height (1.76 km) is above the PBL (1.62 km). For the most unstable parcel, it is observed significantly higher values of LFC, where their values are always above the PBL. However, the qualitative behavior is still qualitatively similar to all cases, with ShCu days exhibiting higher values and Deep and Cong showing comparable values.

Figure 5.10 shows the 100-hPa Mixed-Layer Convective Inhibition (MLCIN) and Convective Available Potential Energy (MLCAPE). The most developed convective regimes show a combination of higher MLCAPE and lower MLCIN in the early morning, which provides more buoyancy and a lower initial thermodynamic barrier for convection to develop. In the afternoon, the MLCAPE is higher for the Deep regime (1237 J kg$^{-1}$), a few hours preceding the late afternoon STD transition, slightly surpassing the value for the Cong regime (1111 J kg$^{-1}$) and significantly exceeding the value for the ShCu regime (671 J kg$^{-1}$).

Figure 5.10c shows minus the difference in CAPE between two consecutive radiosonde launch times. The difference $-\Delta$MLCAPE at 17 LST (CAPE(14 LST) - CAPE(20 LST)) is higher for the Deep regime (390 J kg$^{-1}$), while the Cong regime (62 J kg$^{-1}$) approximates zero, and the ShCu regime (-398 J kg$^{-1}$) shows negative values. This suggests

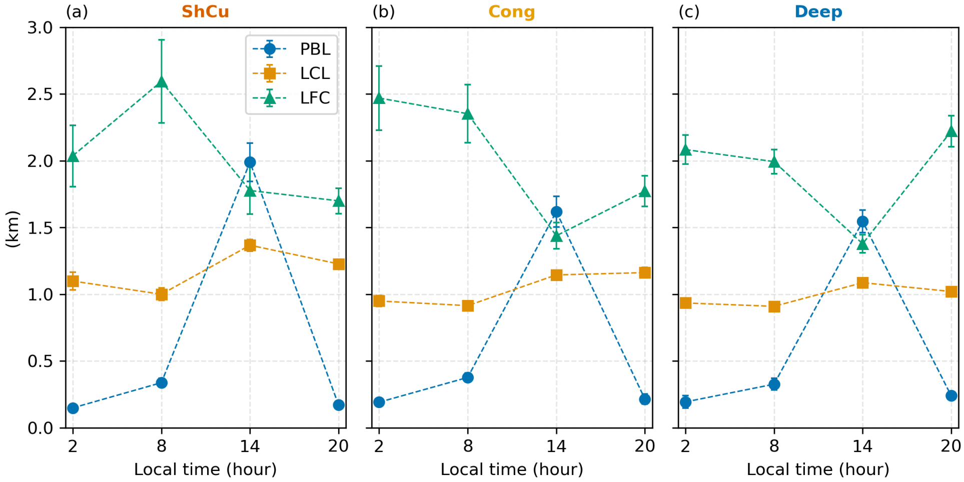

Figure 5.9 – Comparison of PBL, LCL, and LFC heights for (a) ShCu regime, (b) Cong regime, and (c) Deep regime. LCL and LFC are determined using the 100-hPa mixed-layer parcel.

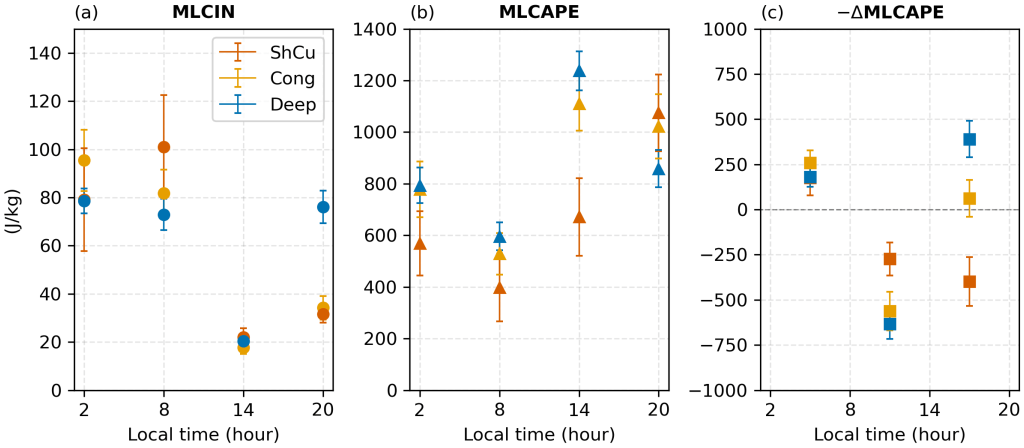

Figure 5.10 – (a) 100-hPa mixed-layer (ML)CIN, (b) MLCAPE, and (c) and −ΔMLCAPE. The circle marker shows MLCIN and MLCAPE available at the radiosonde launch times (02, 08, 14, and 20 LST), while the triangle marker describes −ΔMLCAPE calculated as the difference in MLCAPE between two consecutive times.

that convection in more advanced stages consumes CAPE more effectively, resulting in the elimination of atmospheric instability.

The Appendix A also shows the results for CIN, CAPE, and −ΔCAPE determined using the most unstable parcel (Figure A.5), 50-hPa mixed-layer parcel (Figure A.6), 25-hPa mixed-layer parcel (Figure A.7), and 10-hPa mixed-layer parcel (Figure A.8). CIN calculated using the mixed-layer parcel shows similar qualitative behavior for all layers. For the most unstable parcel, the early morning CIN for the Deep (15.69 J $kg^{-1}$) days are slightly greater than for the Cong (14.40 J $kg^{-1}$) days. The CAPE displays similar qualitative behavior for all idealized parcels, with the Deep regime showing a much larger CAPE than the ShCu regime at 14 LST. Moreover, CAPE increases for narrower mixing layers, and the difference between the convective regimes also increases. This indicates that layers closer to the surface are more unstable in the Deep regime.

### 5.3.4 Surface Energy Balance

Figure 5.11 shows the surface energy balance. The solar surface insolation exhibits a clear diurnal cycle. It increases in the morning, from 06 LST, then peaks around noon and drops to zero in the early evening, at 18 LST. The ShCu regime shows a more significant peak (713 W $m^{-2}$), while the surface-measured insolation is reduced in the Deep regime (561 W $m^{-2}$). This is explained by the more extensive cloud cover scattering and reflecting more incoming solar radiation on deep days. The surface longwave radiation shows less significant variations than solar radiation during the day, with a peak widely spread from about 10 to 14 LST. The longwave radiation is also higher for the ShCu regime (111 W $m^{-2}$) and lower for the Deep regime (84 W $m^{-2}$), depending primarily on the surface temperature, which is warmer for ShCu and colder for Deep (section 5.3.2).

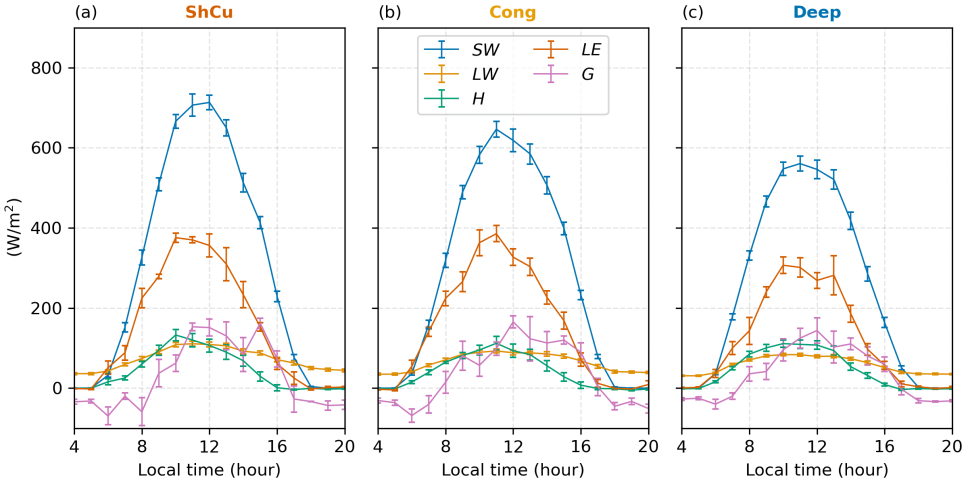

Figure 5.11 – Surface energy balance for (a) ShCu regime, (b) Cong regime, and (c) Deep regime. SW indicates the net shortwave radiation, LW shows the longwave radiation, H corresponds to the sensible heat flux, LE is the latent heat flux, and G is the ground heat flux.

Since the air temperature is mainly related to sensible heat fluxes, the ShCu regime also exhibits greater values (maximum of 133 W $m^{-2}$) than Deep days (maximum of 111 W $m^{-2}$) in sensible heat flux. The latent heat flux is reduced on the Deep days (307 W $m^{-2}$), while the ShCu (maximum of 376 W $m^{-2}$) and Cong regimes (maximum of 386 W $m^{-2}$) have similar magnitudes. Surface evaporation depends primarily on surface temperature and soil moisture. Thus, surface temperature should be a more significant control on latent heat fluxes, mainly because the soil conditions are usually substantially humid during the Amazonian wet season due to abundant precipitation. The net surface radiation is not partitioned only in sensible and latent heat fluxes, but energy is also partially stored on the ground. Figure 5.11 shows that the ground heat flux is positive during the diurnal cycle when the surface is warming and negative during nighttime when the surface is cooling.

### 5.3.5 Surface Water Balance

To understand how the differences in the surface fluxes change CWV and affect the STD transition and accumulated surface precipitation, we analyze the surface water balance. The integral form of the continuity equation for the total water $r_t$ can be written as,

$$\frac{\partial}{\partial t}\int_{p_{\mathrm{top}}}^{p_{\mathrm{bottom}}} r_t \frac{dp}{g} + \nabla \cdot \int_{p_{\mathrm{top}}}^{p_{\mathrm{bottom}}} r_t \vec{V} \frac{dp}{g} = E - P\,, \tag{5.2}$$

where $p$ is pressure, $g$ is gravity acceleration, $\vec{V}$ is the horizontal wind vector, and $E$ and $P$ correspond to evaporation and precipitation. The total water $r_t$ is the sum of all water species mixing ratios, i.e., water vapor ($r_v$), liquid ($r_l$), and ice ($r_i$). The second integral is the water mass flux divergence, which is mostly associated with water vapor. As convective clouds develop or dissipate, the time change of total column water, the first integral, greatly contributes to the continuity equation.

For the sake of analysis, we divide equation (5.2) by the density of liquid water $\rho_l$ (1000 kg m$^{-3}$) and ignore the time variation of the ice term, which is usually a reasonable assumption. Thus, the continuity equation (5.2) can be rewritten in the simplified form

$$\frac{\partial}{\partial t}\mathrm{CWV} - \mathrm{EVAP} + \mathrm{PREC} = \mathrm{CONV} - \frac{\partial}{\partial t}\mathrm{LWP}\,, \tag{5.3}$$

where EVAP corresponds to the evaporation rate, PREC corresponds to the precipitation rate, and CONV represents the water vapor convergence. Note that we intentionally rearranged the equation's order to emphasize terms with observations on the left-hand side and the residue, which can only be estimated, on the right-hand side. The radiosonde provides atmospheric profiles every 6 hours, corresponding to the period where we can calculate CWV and its time variation. Evaporation is determined from the latent heat flux data. For precipitation, we use the surface measurements from AOSMET (see section 5.1). For timescale consistency, both evaporation and precipitation are averaged over 6 hours, corresponding to the interval of two consecutive radiosonde launches. The associated time derivative of CWV is given by

$$\frac{\partial}{\partial t}\mathrm{CWV}(t+3h) = \frac{\mathrm{CWV}(t+6h) - \mathrm{CWV}(t)}{6h}\,. \tag{5.4}$$

Note that it is necessary to use the CWV of the following day to estimate its time derivative at 23 LST. The difference in water vapor convergence and the variation in liquid water path, i.e., the right-hand side of equation (5.3), is estimated using the mean composites for $\partial\mathrm{CWV}/\partial t$, EVAP, and PREC.

The water balance results are shown in Figure 5.12. From nighttime to early morning (02-08 LST), before convection starts, the variation in CWV is essentially due to the advection of water vapor, as there is minimal evaporation. During this period, water vapor divergence predominates for ShCu and Cong regimes, while the Deep regime shows a neutral condition.

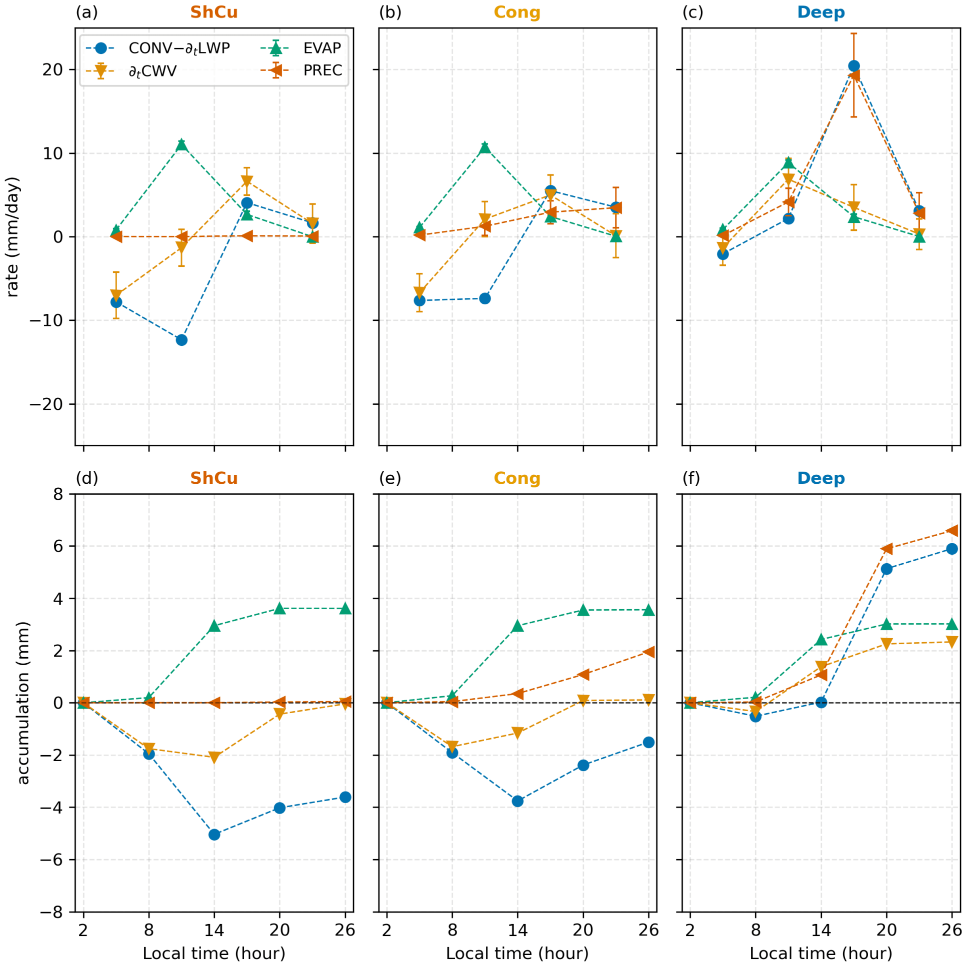

Figure 5.12 – Surface water balance for (a,d) ShCu regime, (b,e) Cong regime, and (c,f) Deep regime. Upper panels correspond to the rate of changes, while lower panels show water accumulation along the day. See the text for more details.

From early morning to early afternoon (08-14 LST), the difference in the convergence of water vapor and variation of liquid water path continues to be significantly negative for both ShCu and Cong regimes, being nearly in balance with evaporation. This divergence removes the evaporated water from lower levels; hence the variation in CWV is nearly zero for ShCu and Cong regimes, and there is little precipitation. On the other hand, the Deep regime shows a slightly positive value in CONV-$\partial$LWP/$\partial t$, which has to be associated with vertical motion (see section 5.3.6). Consequentially, the evaporation and convergence of water vapor promote more convective cloud development and precipitation around noon in the Deep regime (see Figure 5.5).

During the afternoon and evening (14-20 LST), the CONV-$\partial$LWP/$\partial t$ term shows a small positive value for ShCu and Cong regimes. Conversely, the Deep regime shows a substantial peak of CONV-$\partial$LWP$/\partial t$ and precipitation, being 20.4 mm day$^{-1}$ and 19.3 mm day$^{-1}$, respectively. Since the liquid water path increases with deep convection, the mean convergence of water vapor should be greater than 20 mm day$^{-1}$ in the afternoon for the Deep regime. The convergence of water vapor approximately balances deep precipitation, which indicates a strong relationship between convergence and STD convection transition. The lower panel in Figure 5.12 shows the integrated changes throughout the day. The relative contribution of each term in the water balance varies among the convective regimes. For the ShCu regime, the water gained through evaporation is almost totally removed by the moisture flux divergence; hence little precipitation is produced. The Cong regime shows a weaker moisture divergence than the ShCu regime, and thus evaporation is more efficiently converted into cloud water and precipitation. For the Deep regime, precipitation strongly relates to the convergence of water vapor, but also depends on evaporation. On Deep days, we also see a net increase in CWV at the end of the day of about 2 mm, which might affect the convective regimes developing the following day.

### 5.3.6 Large-Scale Wind Properties

Figure 5.13 shows the wind speed at 08 LST, 11 LST, and 14 LST for all convective regimes. There is a characteristic low-level jet during the wet season, with a peak between 900-800 hPa layer. During the morning, the ShCu regime shows a lower and slightly stronger jet. However, the PBL grows during the day to a height of 1-2 km (section 5.3.3), reaching higher altitudes for ShCu days, and the mixing of free-tropospheric and PBL momentum potentially reduces the wind speed. As a result, the lower jet in the ShCu regime is more significantly affected by the PBL growth. Thus, at both 11 LST or 14 LST, the Deep regime presents a more vigorous and slightly higher low-level jet. For the mid- and upper-levels, between 600-300 hPa layer, the ShCu regime shows an additional upper-level jet, while the Cong and Deep regimes exhibit weaker and comparable wind speeds.

Figure 5.14 shows the hodograph at 14 LST. The wind turns clockwise as height increases: north-easterly winds dominate in the boundary layer, roughly speaking below 800 hPa, while easterly winds dominate in the $\sim$ 700-500 hPa layer. The only notable difference in wind direction occurs in the high troposphere, above 400 hPa level. Particularly for the Deep days, the wind stops veering and shows a consistent south-easterly direction. Since the wind profiles at low- and mid-levels are comparable among the convective regimes, the veering of the wind solely does not explain the convection initiation in the Amazon. However, it hints at a possible control mechanism for the development from the congestus to the deep phase.

Figure 5.15 shows the large-scale subsidence from the variational analysis at 08

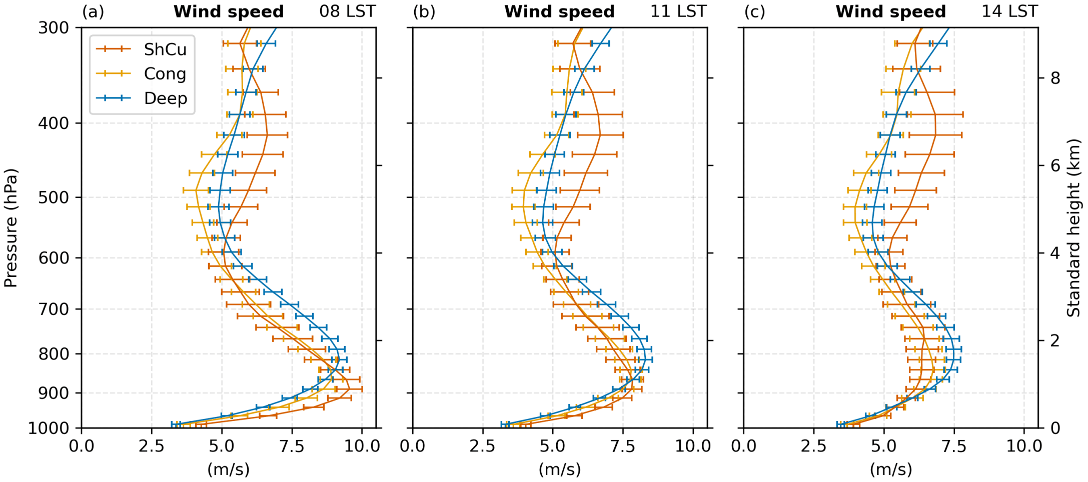

Figure 5.13 – Wind speed at (a) 08 LST, (b) 11 LST, and (c) 14 LST for ShCu, Cong, and Deep regimes.

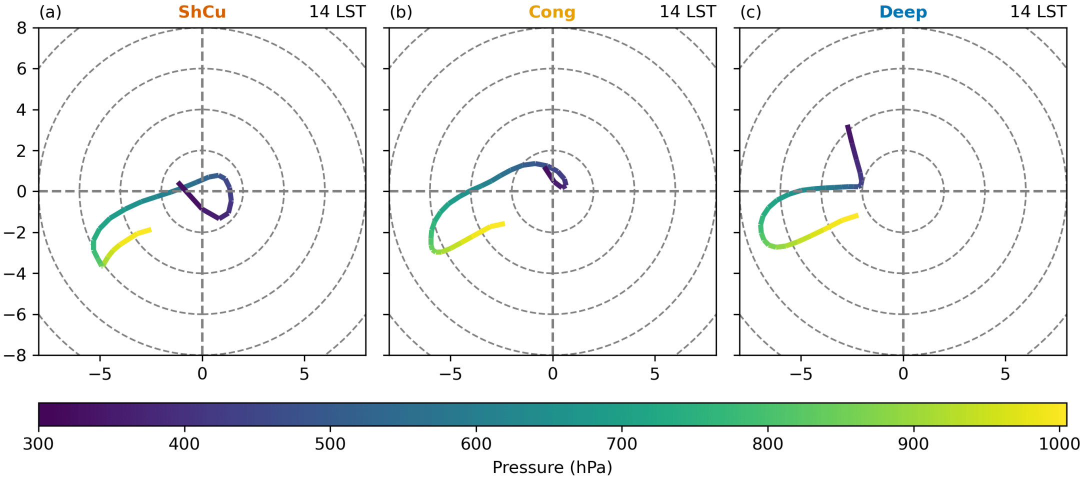

Figure 5.14 – Hodograph at 14 LST for (a) ShCu regime, (b) Cong regime, and (c) Deep regime.

LST, 11 LST, and 14 LST. In the early morning, the Deep regime shows moderate convergence below the 700 hPa, although it is relatively greater compared to those associated with the ShCu and Cong regimes. Above 700 hPa, the subsidence assumes positive and comparable values among the convective regimes. Around noon (11 LST), the Deep regime is dominated by convergence below 600 hPa, while the ShCu and Cong regimes exhibit similar profiles of subsidence with positive values above the surface. In the afternoon, significant differences in subsidence are observed among the convective regimes. The Deep regime is dominated by convergence, especially above the 800 hPa level. The ShCu and Cong regimes exhibit important subsidence in the low levels, particularly below 700 hPa, with ShCu-subsidence assuming higher magnitudes.

To evaluate the vertical wind shear, we used the bulk wind shear defined by the magnitude of the vector difference of the wind at two levels. Figure 5.16 shows the vertical bulk wind shear for the layers 0-2 km, 0-4 km, 0-6 km, and 0-8 km. The layer 0-2 km

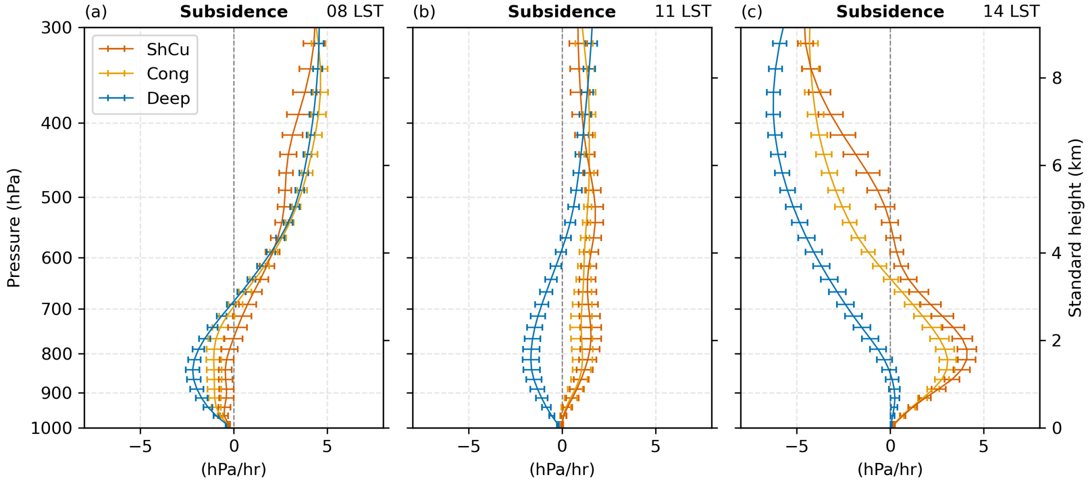

Figure 5.15 – Large-scale subsidence at (a) 08 LST, (b) 11 LST, and (c) 14 LST for ShCu, Cong, and Deep regimes.

shows a more evident dependence on the diurnal cycle, with the Deep days followed by Cong days showing the most substantial wind shear at any time. This result indicates that low-level vertical wind shear reasonably relates to convection development.

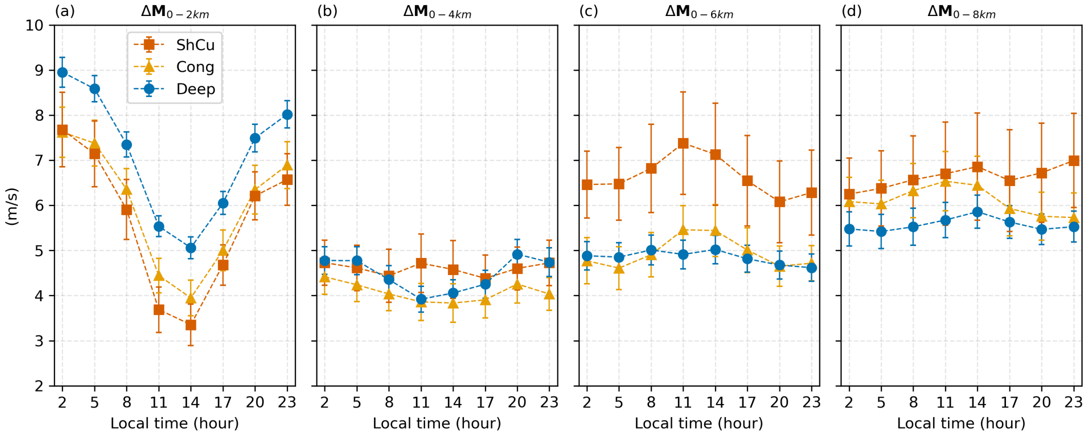

Figure 5.16 – Vertical bulk wind shear for the layers (a) 0-2 km (sfc-790 hPa), (b) 0-4 km (sfc-615 hPa), (c) 0-6 km (sfc-465 hPa), and (d) 0-8 km (sfc-365 hPa).

For the 0-4 km layer, the wind shear reveals a more similar pattern among the convective regimes. For the layer 0-6 km, only ShCu days exhibit a distinct wind shear, being more robust and with a standard deviation that can reach more than 1 m $s^{-1}$. However, this layer has an extension at least double the cloud top of the shallow cumulus ($<$ 3 km), suggesting that mid-level wind shear might play a minor role in the STD transition. For the layer 0-8 km, the wind shear is slightly greater for Cong days than Deep days.

## 5.4 Conditionally Averaged Precipitation

This section evaluates the conditionally averaged precipitation as a function of the most relevant variables controlling the STD transition. From the previous section, we verified that convective development is mainly related to moisture, instability, and vertical wind shear. Here, we investigate the response of precipitation to moisture using the low- and mid-troposphere CWV at 08 and 14 LST. The response to convective instability is assessed using the 100-hPa MLCAPE and its variation ($-\Delta$MLCAPE) at 17 LST. We use the bulk shear magnitude for the 0-2 and 0-8 km layers at 14 LST as the surrogate of vertical wind shear. Precipitation from S-band radar is averaged over the analysis domain ($100 \times 100$ km$^2$ centered at T3) and from 14 to 20 LST.

Figure 5.17 shows in green the conditionally averaged precipitation as a function of CWV for the local convective days. The conditionally averaged precipitation corresponds to the average precipitation observed within distinct CWV bins, which are represented as horizontal bars in Figure 5.17. Note that, for this analysis, we combine the ShCu, Cong, and Deep regimes as the local convective days. For comparison, we also include the ShCu data without taking any averaging. First, we note that early morning CWV (low or mid-levels) is reasonably correlated with afternoon precipitation. However, there are ShCu days with a similar range of CWV at 08 LST and no precipitation. Therefore, early morning CWV alone does not explain afternoon deep convection and precipitation.

Afternoon precipitation shows a more robust relationship with low-level CWV at 14 LST. Convective precipitation increases sharply above CWV$_{low}$ = 35 mm. However, ShCu days can have up to CWV$_{low}$ = 42 mm, indicating that the excess of low-level water vapor does not guarantee the STD transition. In the mid-levels, higher values of CWV are also associated with higher precipitation. In this case, there is no lower bound, i.e., a drier mid-level atmosphere reduces surface precipitation but does not preclude the STD transition from occurring. Here we also find ShCu days spanning a wide CWV$_{mid}$ range, indicating that the mid-level moisture does not control whether the convective development stops at the ShCu, Cong, or Deep stages.

Figure 5.18 shows the conditionally average precipitation as a function of instability and vertical wind shear. No single variable triggers the STD transition, as we observe precipitating and non-precipitating days for similar environmental conditions. Afternoon precipitation increases weakly with MLCAPE and more strongly with the change in MLCAPE from 14 to 20 LST. Precipitation also increases with low-level vertical wind shear. Finally, the upper-level bulk wind shear shows a weak impact on precipitation, with larger precipitation rates found for weaker deep-layer shear intensity.

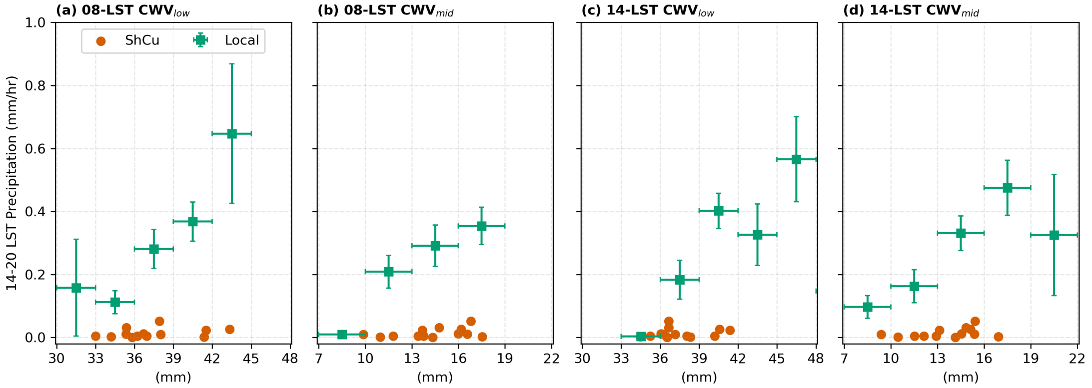

Figure 5.17 – Conditionally average precipitation to (a) low-troposphere CWV at 08 LST, (b) mid-troposphere CWV at 08 LST, (c) low-troposphere CWV at 14 LST, (d) mid-troposphere CWV at 14 LST. Precipitation corresponds to the mean S-band radar precipitation from 14 to 20 LST, averaged in 3 mm CWV intervals (horizontal bars). The conditionally average analysis is carried out for local (green square marker) convective days (ShCu, Cong, and Deep regimes). We also include the scatter ShCu (red circle marker) data.

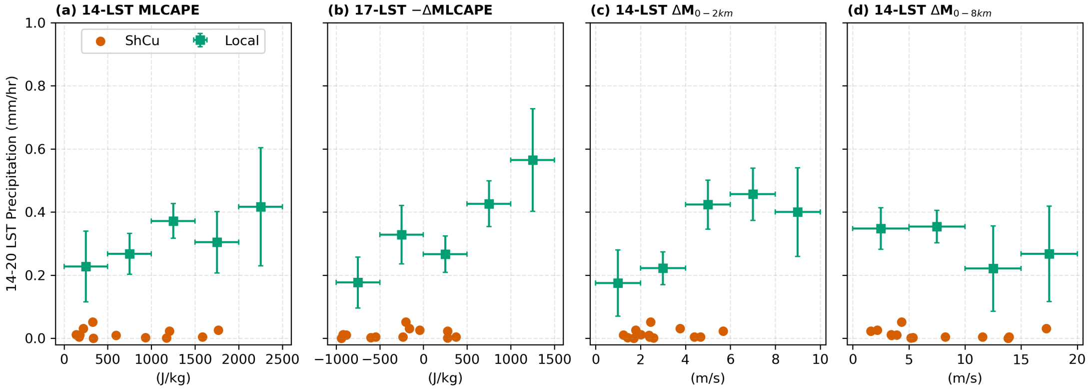

Figure 5.18 – Conditionally average precipitation to (a) 100-hPa MLCAPE at 14 LST, (b) $-\Delta$CAPE at 17 LST, (c) 0-2 km bulk shear magnitude at 14 LST, and (d) 0-8 km bulk shear magnitude at 14 LST. Precipitation corresponds to the mean S-band radar precipitation from 14 to 20 LST. The MLCAPE and $-\Delta$MLCAPE have a bin size of 500 J kg$^{-1}$, 0-2 km bulk shear has a bin size of 2 m s$^{-1}$, and 0-8 km bulk shear has a bin size of 5 m s$^{-1}$ (horizontal bars).

## 5.5 Discussion

The previous section presented the wet-season composites of ShCu, Cong, and local Deep convection days for both environmental and cloud properties measured during the GoAmazon2014/5 Campaign. We found that isolated deep convection is associated with more extensive and longer-lived clouds throughout the diurnal cycle. The cumulonimbus clouds can extend up to 16 km of altitude, and maximum rain cover occurs around 16-17 LST, being associated with STD transition in the central Amazon. This agrees with previous studies in the southern Amazon. For instance, TOTA *et al.* (2000) and

MACHADO (2002) analyzed data from the Wet Season Atmospheric Mesoscale Campaign (WETAMC), from January to February 1999, and reported two main modes of precipitation: isolated convection, which peaks in the afternoon around 16 LST, and organized convection associated with mesoscale convective systems, with a maximum during nighttime around 04 LST. The diurnal peak associated with deep convection is also documented more recently in GHATE; KOLLIAS (2016) and TIAN *et al.* (2021), who also used the GoAmazon2014/5 observations but did not focus on the wet season as in our study.

Our results show that deep days are associated with moister conditions in the early morning, but only in the low troposphere, particularly below 3 km. Above that altitude, the partial column water vapor ($\mathrm{CWV_{mid}}$) is slightly greater in the Cong regime at 08 LST. During the dry season, GHATE; KOLLIAS (2016) found a similar early morning moist layer but at higher altitudes, between 3 and 5 km. From early morning to afternoon, a divergence of water vapor dominates the ShCu and Cong regimes, while convergence predominates in the Deep days. Thus, the Deep regime shows more significant water vapor excess in both low- and mid-troposphere at 14 LST, a few hours preceding the late afternoon STD transition. From 14 to 20 LST, water vapor convergence substantially increases in Deep days, suggesting a strong relationship with deep convection. However, since our water budget analysis is based on a 6-hr resolution, we can not know for sure, for example, whether the convergence causes convection or is a result of vertical motion associated with convection. Therefore, the convergence could be a trigger for the STD transition or only an associated effect.

Despite that, the relevance of water vapor convergence to deep convection is also highlighted in ADAMS *et al.* (2013). They used 3.5 years of data from a dense Global Navigation Satellite System (GNSS) meteorological network in the central Amazon, which provided high frequency (5 min), all-weather, CWV data. The authors observed a rapid increase in water vapor convergence, starting 4 hours before the STD transition, showing a characteristic peak reasonably in phase with the maximum cloud depth and precipitation. While an advantage of their analysis is the long-term GNSS observations of CWV, they did not have evaporation data to investigate its contribution to the water budget. Our analysis showed an important contribution of this term, of about 3.5 mm per day. Evaporation is maximum around 11 LST, which helps moisten the atmosphere; in contrast, moisture convergence is maximum in the mid afternoon, 15 LST, more directly associated with the STD transition.

The large-scale wind shows a typical low-level jet from E-NE during the wet season, with a peak between 900-800 hPa layer. As the diurnal cycle progresses, the boundary layer growth affects the low-level jet strength. Since the ShCu regime shows a higher convective boundary layer height, the low-level jet also tends to be weaker in the afternoon of shallow days. Based on the conditionally-averaged precipitation, we identified that precipitation increases when low-level wind shear (0-2 km) increases. However, similar high wind shear values were found for ShCu days without precipitation. Hence, low-level vertical wind shear is not critical for the STD transition but can modulate the diurnal precipitation intensity. The deep-layer wind shear (0-8 km) has the opposite effect, although it is not as important as that from the low-level shear. Deep-layer shear is higher for ShCu than for Cong or Deep days, but a weaker shear only slightly favors precipitation.

In particular for the GoAmazon2014/5 experiment, several other studies also assessed vertical wind shear's role in convection. ZHUANG *et al.* (2017) used the radar wind profiler and radiosonde data to evaluate the shear conditions using a bulk metric. They relate a more intense wind shear in both layers 0-3 and 0-6 km to deep convection, but this is only seen during the dry season. Thus, they suggest that wind shear does not favor convection during the wet and transition seasons. CHAKRABORTY *et al.* (2018) focused only on the transition season and used the radiosonde data and bulk shear method. They noted that shallow convection days had a stronger low-level and weaker deep-level shear intensity than deep convective days. The authors argued that vertical wind shear could limit the development of deep convection, as the entrainment of dry air increases under more intense low-level vertical wind shear conditions. In the work by TIAN *et al.* (2021), they investigated wind shear through the vertical derivative of the large-scale zonal wind from the variational analysis. The authors noted a relevant difference in the vertical wind shear in the mid-troposphere among congestus and deep convection days, suggesting that wind shear may limit the vertical extent of convection regardless of the season. Despite the different procedures used to analyze the vertical wind shear, our results contribute to the consensus that vertical wind shear is not a trigger to the STD transition, and only weakly modulates cloud vertical development and precipitation.

The conditionally-averaged precipitation analysis indicated that the STD transition is not triggered by any of the analyzed environmental conditions alone. While precipitation scales linearly with the low troposphere CWV in the afternoon, we also observe days with relatively high humid conditions where convection stays confined to the ShCu regime. Precipitation also increases with mid-troposphere CWV, but there is still precipitation even for the driest conditions at these levels. SCHIRO *et al.* (2016) showed that precipitation significantly correlates to CWV in the Amazon and a western Pacific tropical site; however, they analyzed total CWV and precipitation averaged in the same time window. In our case, we found that even the early morning CWV, at both low and mid-levels, has an impact on the afternoon precipitation.

From our results, mixed-layer CAPE is smaller for ShCu days and higher for Deep days, with the difference increasing from nighttime (2 LST) to early afternoon (14 LST). Still, it only weakly correlates with afternoon precipitation. After this time, CAPE is smaller for Deep and higher for ShCu, as it is significantly consumed by the diurnal precipitation. Hence, the change in CAPE from 14 to 20 LST shows a more robust relationship with precipitation. SCHIRO *et al.* (2018) evaluated the relationship between buoyancy and precipitation. They also showed that CAPE weakly relates to precipitation if not including deep-inflow mixing to represent the entrainment of dry air in the parcel.

## 5.6 Preliminary Conclusions

We analyzed measurements from the GoAmazon2014/5 field campaign in the central Amazon with the goal of assessing possible controlling mechanisms of the shallow-to-deep convective transition. We classified wet season days into shallow (ShCu), congestus (Cong), and Deep regimes, purposely excluding mesoscale systems to focus on locally-driven deep convection.

The Deep regime is characterized by moister conditions in the low levels since early morning, notably below 3 km. There is significant water vapor divergence during the mornings of Cong and ShCu days and a weak convergence in the Deep days. As a result, the Deep regime shows higher column water vapor (CWV) in the low- and mid-troposphere at 14 LST. In the afternoon, more vigorous water vapor convergence occurs during Deep days, associated with the late afternoon STD transition. However, it is necessary to conduct further studies to evaluate whether the water vapor convergence is a cause or effect of convection.

By averaging the precipitation in intervals of CWV, we found that the afternoon precipitation (14 to 20 LST) for local convective days is highly correlated with the water vapor content in low and mid-troposphere, both in the early morning (08 LST) and afternoon (14 LST). Nevertheless, days without precipitation exhibit a somewhat similar range of CWV values, indicating that column water vapor is a necessary but insufficient condition for the STD transition.

Our results showed that CAPE is significantly higher in the Deep regime than in the ShCu days during the afternoon. Precipitation also tends to increase with CAPE, albeit weakly. Furthermore, there are days with high CAPE and no precipitation, indicating that while CAPE enhances stronger convection, it does not act as a trigger. The difference in CAPE after and before the STD transition correlates better with precipitation, indicating the effect of precipitation in removing instabilities from the atmosphere. A similar analysis of the vertical wind shear also showed that it does not trigger the STD transition, but instead only weakly influences the amount of precipitation. In contrast to some previous studies, we found that precipitation increases under environmental conditions of stronger low-level shear and weaker upper-level shear.

While our findings are statistically robust, we recognize that the water budget of the different convective regimes should be further investigated. We calculated the CWV using radiosonde measurements, which were launched every 6 hours. While the microwave radiometer provides high-temporal resolution measurements of CWV and liquid water path, it is only suitable for fair-weather conditions. Consequently, consistent high-temporal observations of these variables during the GoAmazon2014/5 campaign are lacking, particularly during deep precipitating events. Future analyses should aim to achieve a higher temporal resolution of the water balance and also incorporate information on liquid and ice water paths.

# 6 SENSITIVITY OF ENVIRONMENTAL CONTROLS ON CONVECTION IN HIGH-RESOLUTION NUMERICAL SIMULATIONS

This chapter presents our modeling study of convection and precipitation in the central Amazon. We study the sensitivity of the STD convection transition in the Amazon to different controlling mechanisms through idealized high-resolution simulations. Firstly, we focus on the model validation for the period of December 2014. Then, we propose sensitivity experiments in which moisture or wind are perturbed at different atmospheric levels to assess the relative importance of preconditioning and vertical wind shear at the low troposphere and higher levels in developing deep convection. The role of moisture advection is also evaluated.

We organize this chapter as follows: Section 6.1 describes the specific data and methods applied in the modeling study. Section 6.2 covers the model validation, where we compare simulation results with GoAmazon 2014/5 observations. Section 6.3 describes the properties of deep convection. Sensitivity experiments for moisture and wind shear are conducted in section 6.4. Section 6.5 discusses the results. Section 6.6 gives the preliminary conclusions.

## 6.1 Modeling Data and Methods

An overview of the GoAmazon2014/5 experiment (section 4.2), the important instrumentation for this project (section 4.3), the data to characterize the soil and vegetation (section 4.4), a summary of large-scale fields (section 4.5), and a description of the atmospheric model (section 4.6) are presented in Chapter 4. The following section describes the specific data used for the simulations and model validation. In addition, we also describe the model configuration and the procedures to identify cloud types and cloud regime days.

### 6.1.1 Modeling Data

For the model validation, we use the S-band surface precipitation rate averaged every 30-min over the model domain of 200x200 km$^2$ centered at the T3 site. Note that we conduct simulations in a modeling domain larger than the observational domain (100x100 km$^2$) utilized in the previous chapter. Since the MCSs cover a spatial scale of around 100 km (HOUZE Jr., 2004), we opted for a more extensive domain[1] to better accommodate these systems within our simulations. This ensures a more consistent representation of convection in the simulations, while it is important to emphasize that our primary focus

---

[1] The domain size is also contingent upon the cluster architecture (section 4.7), necessitating configuration adjustments to enhance simulation performance.

remains on locally-driven convection. Alongside precipitation, we calculate column water vapor (CWV) using SONDE data. We use the 30-min surface sensible heat flux (H) and latent heat flux (LE) from QCECOR. Additionally, we utilize a 30-min average of surface shortwave and longwave fluxes for the downward (SKYRAD) and upward (GNDRAD) components.

The simulations are forced with the VARANAL large-scale fields of water vapor mixing ratio, temperature, wind, and moisture and temperature tendencies (section 4.5). The Surface Land Model is initialized and forced using data of land cover type, leaf area index, clay and sand content, and soil temperature and wetness (section 4.4). These data are utilized with certain idealizations and optimizations, which are described in the following section.

### 6.1.2 Model Configuration

We use the System for Atmospheric Modeling version 6.11.8 (SAM 6.11.8) coupled with a simplified Surface Land Model (SLM) (see section 4.6). The control model configuration utilized in the simulations conducted in this thesis is based on a domain of $200\times200\times27$ km$^3$. The horizontal resolution is set at 500 m. The vertical resolution varies from a minimum of 50 m below 1.5 km up to 500 m in the upper troposphere, resulting in 128 grid points. The temporal resolution is 5 seconds, and instantaneous model fields and statistics are output every 30 minutes. We use the simplified SLM to calculate the surface fluxes. The CAM3 radiation scheme is called every 150 seconds.

Specifically for the model validation, we conducted simulations to test the impact of different microphysics parameterizations. The single-moment, double-moment, and P3 schemes were evaluated with 500 m resolution within a 200x200 km$^2$ domain. We also assessed resolution and domain size sensitivity using the P3 scheme: in one case, the resolution varied from 500 m to 250 m (P3/250m), and in another case, the domain size changed from 200x200 km$^2$ to 400x400 km$^2$ (P3/400km).

The large-scale forcing is based on the VARANAL dataset for the period of December 2014 in the central Amazon. Winds were nudged with a 2-hour timescale throughout the simulation. The water vapor mixing ratio was nudged only during the spin-up period (1-5 December 2014), at a timescale of 6 hours.

Figure 6.1 shows the MODIS data for land cover type during 2014 and mean leaf area index (LAI) for December 2014 over a domain of $200\times200$ km$^2$ centered at T3 site. These are associated with the period and area of our simulations. The domain averaged LAI is 4.4 m$^2$ m$^{-2}$, which was set as constant in our simulations. Evergreen broadleaf forests covered 83% of the area, so we idealize the simulations using this vegetation type. However, based on several tests conducted to optimize the SLM parameters, we modified the default near-infrared visible albedo for vegetation from 0.20 to 0.30, the displacement height factor from 0.68 to 0.65 (the corresponding displacement height is 0.65 x 20 m = 13 m, where 20 m is the default value of the height of vegetation), and the root length from 150 cm to 200 cm. These modifications improved the agreement between the observations and the simulated surface radiation, latent and sensible heat fluxes.

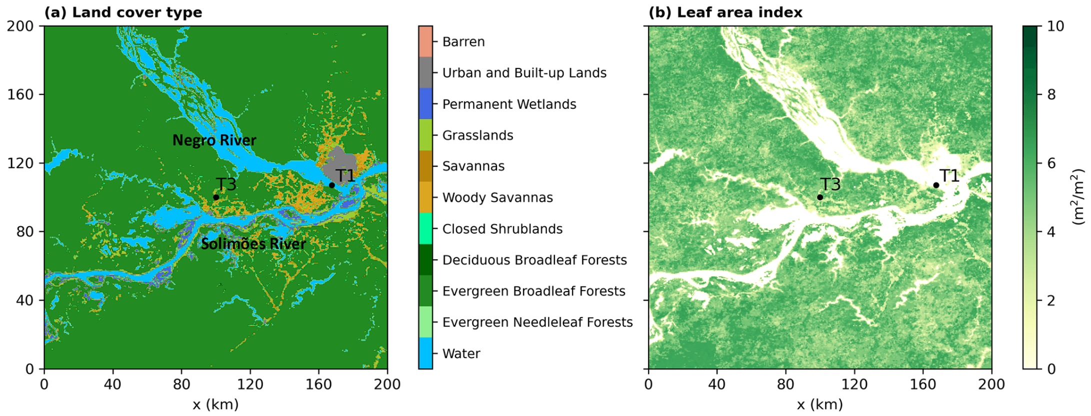

Figure 6.1 – (a) Land cover type and (b) LAI on SAM's coordinate. The 200x200 km$^2$ domain is centered at the T3 site (3.21°S, 60.60°W). Land cover is from 2014, and LAI is based on the average for December 2014. We also indicate in (a) the Solimões River and Negro River.

For the soil, we employed 11 layers from the surface down to a depth of 400 cm. Clay and sand contents for each layer are based on in-situ measurements on Terra-firma forests (section 4.4). The initial conditions for soil temperature and soil wetness are based on the GLDAS Noah, which provides information on 4 layers: 0-10, 10-40, 40-100, 100-200 cm. The SLM soil layers close to the surface, which reflect greater diurnal cycle variation, are interpolated using the nearest neighbor. The deeper soil layers are interpolated (and extrapolated) linearly. The initial profile of soil temperature and wetness is shown in Figure 6.2.

### 6.1.3 Cloud Type Identification

We create a mask of cloud type to analyze the deep convection properties (section 6.3). First, we define a cloud condensate mixing ratio, $r_n$, as the sum of cloud liquid water and total ice (including precipitating and nonprecipitating ice types) mixing ratios. A grid box is considered cloudy if $r_n > 10^{-1}$ g kg$^{-1}$, and a cloudy column is a continuous vertical column of cloudy grid boxes. The cloud base and cloud top correspond to the first and last levels of a cloudy column, respectively. We identify the cloud type at each location based on the criteria utilized by GIANGRANDE *et al.* (2017) with two adaptations, described in Table 6.1. Our cloud mask retains only the cloud type of the lower cloudy column, unless multiple convective clouds (cloud base < 3 km) are detected, in which case the most developed one is retained. For example, it is possible to find a shallow cumulus with a congestus cloud above. The condensate gap between the two cloudy columns could be

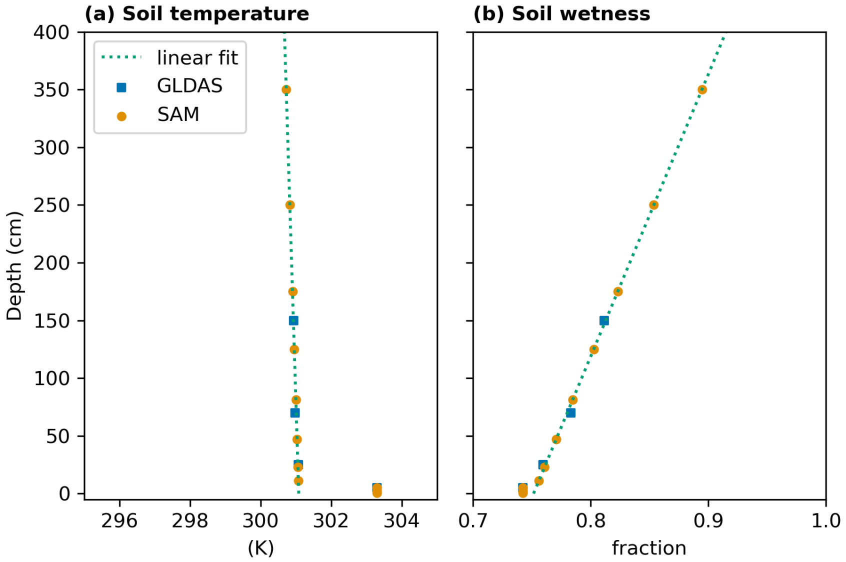

Figure 6.2 – (a) Soil temperature and (b) soil wetness initial condition. GLDAS Noah data for 1 December 2014 at 00 UTC.

Table 6.1 – Cloud type definitions based on the criteria of GIANGRANDE *et al.* (2017). The second criteria in (1) and (5) correspond to our adaptations.

| Cloud type | Cloud base | Cloud top | Cloud thickness |
|---|---|---|---|
| (1) Shallow cumulus | $< 3$ km | $< 3$ km | $< 3$ km |
| | $< 3$ km | 3-8 km | $< 1.5$ km |
| (2) Congestus | $< 3$ km | 3-8 km | $\geq 1.5$ km |
| (3) Deep convection | $< 3$ km | $> 8$ km | No restriction |
| (4) Altocumulus | 3-8 km | 3-8 km | $< 1.5$ km |
| (5) Altostratus | 3-8 km | 3-8 km | $\geq 1.5$ km |
| | 3-8 km | $> 8$ km | $< 1.5$ km |
| (6) Cirrostratus/anvil | 3-8 km | $> 8$ km | $\geq 1.5$ km |
| (7) Cirrus | $> 8$ km | $> 8$ km | No restriction |

filled by varying the condensate threshold or including one additional threshold. For our study, it is enough to use the simplified procedure for cloud-type identification.

### 6.1.4 Cloud Regime Days

For the sensitivity experiments, we select a set of shallow cumulus (ShCu) and deep convective (Deep) days from the control simulation (P3 microphysics scheme) and perturb the sounding or the large-scale forcing imposed. For the Deep selection, we require that the domain average of total ice presents a distinct deepening during the afternoon and deep convection exhibits a scattered (isolated) pattern. The chosen Deep days are 17, 21, 23, and 26 December. Ideally, we would select days with no ice water for the ShCu selection, but this condition is unavailable in our results. We identified five days with negligible ice content and specifically selected four days: 09, 13, 27, and 28 December. Figure 6.3 shows the profile of cloud liquid and total ice for our selection of cloud regime

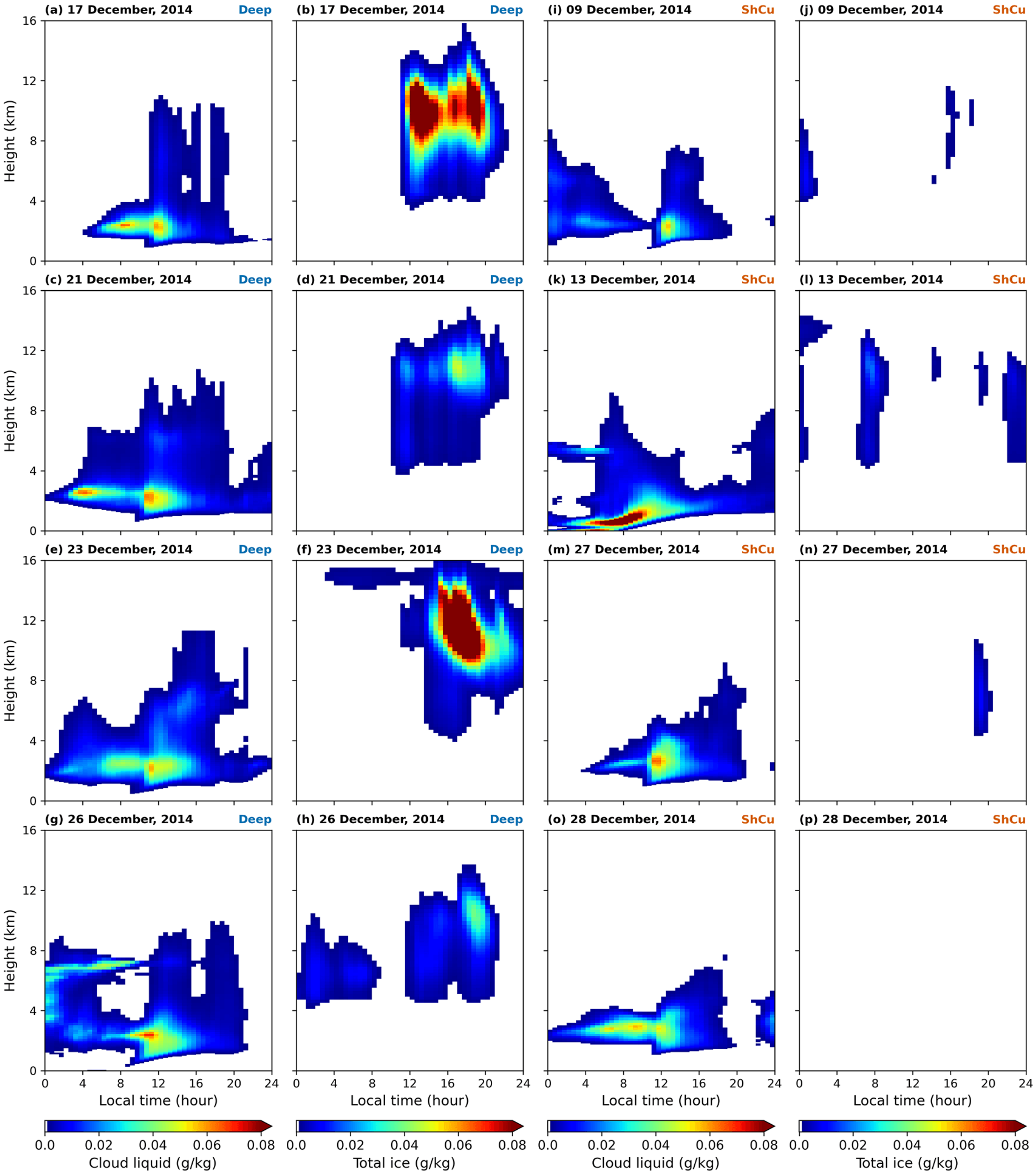

Figure 6.3 – Cloud regime days. The first row (a,c,e,g) shows the cloud liquid, and the second row (b,d,f,h) shows the total ice mixing ratio profile for the selected Deep days. The third row (i,k,m,o) shows the cloud liquid, and the fourth row (j,l,n,p) shows the total ice mixing ratio profile for the selected ShCu days.

days.

## 6.2 Model Validation

A comparison between CWV, precipitation rate, LE, and H between the observations and our simulations are shown in Figure 6.4. The latter encompass simulations carried out using the single-moment, double-moment, and P3 microphysics schemes, in addition to a higher-resolution simulation for the P3 scheme (P3/250m), and a simulation conducted within a larger domain for the P3 scheme (P3/400km). In order to provide quantitative information on the model performance, we also include a Taylor Diagram for each analyzed variable in Figure 6.5.

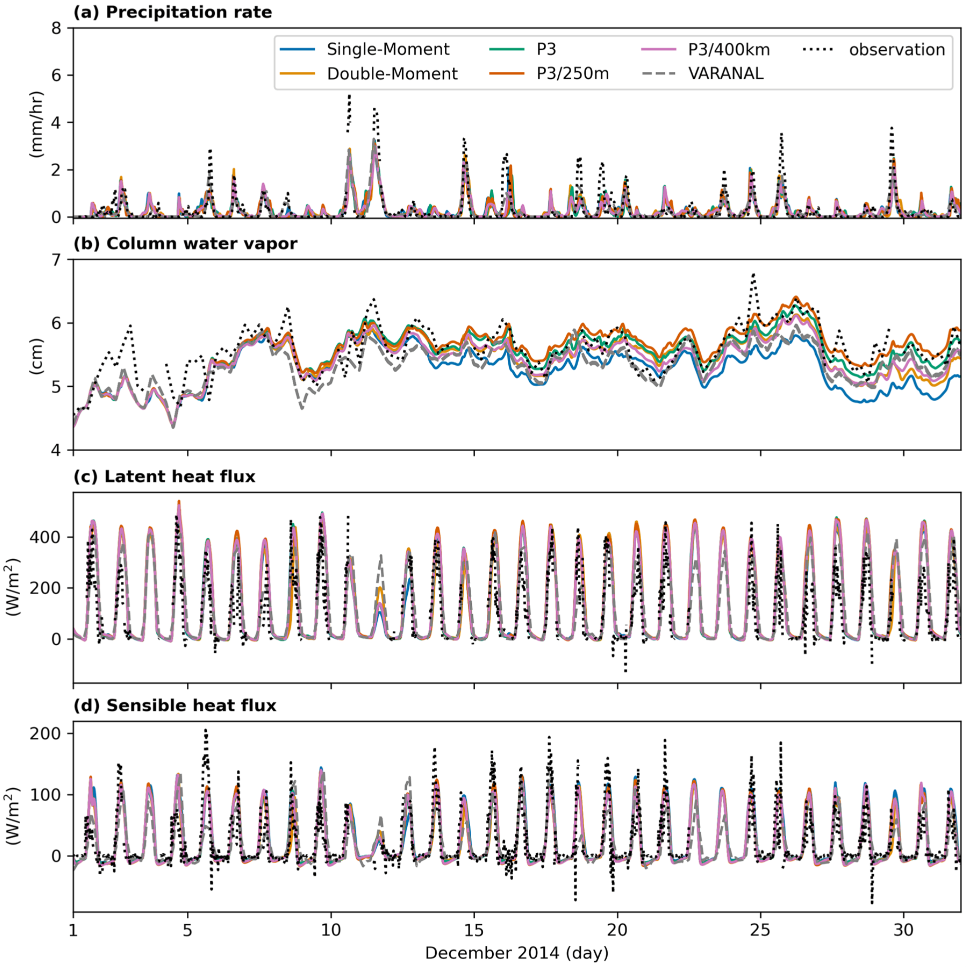

Figure 6.4 – Validation. (a) Precipitation rate. (b) Column water vapor. (c) Latent heat flux. (d) Sensible heat flux. The solid colored line represents the modeling results, the gray dashed line the VARANAL data (large-scale forcing), and the black dotted line the observations.

The similarity of the CWV from the three simulations and observations remains intact for approximately a week because of the water vapor nudging applied during the spin-up period. After this period, some differences start to emerge. CWV values are generally higher for the P3 scheme and lower for the single-moment run. The P3 cases exhibit the strongest correlation (Pearson) with the observations: 0.78 for P3/250m and 0.75 for both P3 and P3/400km. Conversely, the single-moment scheme shows a weaker correlation to the observed CWV (0.56), while the double-moment scheme correlation is close to the P3 scheme (0.70). In terms of the standard deviation of CWV, the model values range from 0.24 mm (P3/250m) to 0.28 mm (Single-Moment), whereas observations indicate a value of 0.34 mm. Despite this difference, these statistics suggest that the model can reasonably reproduce observed moisture content for at least one month without resorting

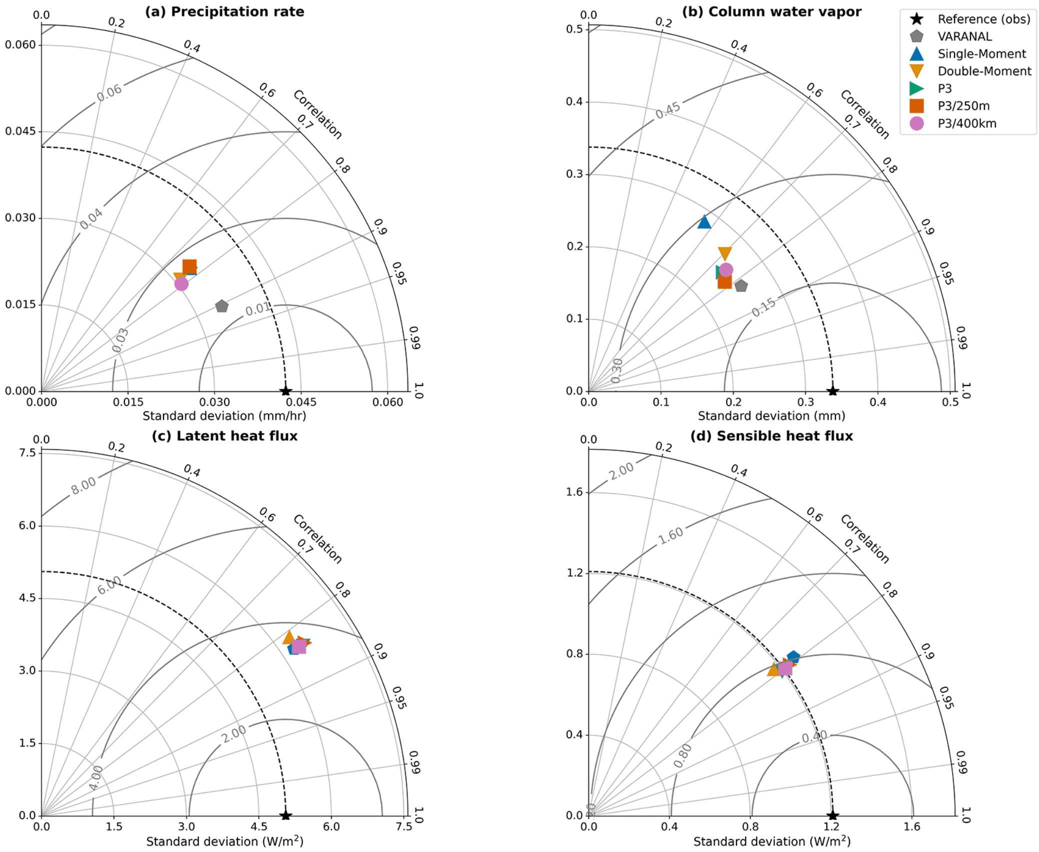

Figure 6.5 – Taylor Diagrams. (a) Precipitation rate. (b) Column water vapor. (c) Latent heat flux. (d) Sensible heat flux. The statistics correspond to the standard deviation of the mean and Pearson correlation.

to any water vapor nudging.

The different simulations closely replicated the observed surface precipitation rate, with correlations ranging from 0.76 (P3/250m) to 0.79 (P3/400km). The simulations exhibit better agreement for lower precipitation rates, while they tend to underestimate the most intense precipitation events associated with mesoscale systems. Moreover, the model precipitation did not show a significant sensitivity with the microphysics, spatial resolution, or domain size. Therefore, we hypothesize that the model's underestimation of intense surface precipitation could potentially be attributed to the periodic boundary conditions. These conditions might prevent the advection of MCSs that could have developed in areas outside the domain. Nevertheless, our validation results remain satisfactory. It is important to reiterate that this thesis primarily focuses on locally-driven STD convective transition.

Observed surface fluxes are reproduced reasonably accurately in the model runs. LE correlations vary from 0.81 (double-moment) to 0.84 (P3, P3/250m, and P3/400km), while the H correlations range from 0.78 (double-moment) to 0.80 (P3, P3/250m, and P3/400km). The model only slightly overestimates the standard deviation of the observed mean LE, with the difference between model runs and observations being less than 2 W

$m^{-2}$. However, it should be noted that the ECOR flux measurement system provides local measurements of surface fluxes in a grassland region (T3 site, see Figure 6.1), while the model provides an average profile for an area of 200x200 $km^2$ (or 400x400 $km^2$ for P3/400km), entirely covered by evergreen broadleaf forest. These differences make the qualitative agreement between model simulations and observations quite impressive.

To evaluate the simulated cloud properties, Figure 6.6 and Figure 6.7 show a comparison between model results and observations of surface shortwave and longwave fluxes, including both downward and upward components.. There is a high-frequency variability of the observed fluxes, which is not present in the model because its values correspond to horizontal averages in the domain, while observational values are taken at the T3 site. Nonetheless, the model satisfactorily reproduces the observations for surface downward/upward shortwave and upward longwave fluxes (correlation ranges 0.82-0.86). In the case of downward longwave fluxes, the correlation is weaker, ranging from 0.57 (single and double-moment) to 0.62 (P3, P3/250m, and P3/400km), although these values are reasonable.

Finally, the CWV displayed more distinct differences between the microphysics schemes, with the P3 scheme exhibiting a stronger correlation with the observations. While neither the higher resolution (P3/250m) nor the larger domain size (P3/400km) simulations demonstrated significant improvements over the P3 case, they notably increased computational costs (see section 4.7). This motivated our choice of the P3 scheme with 500 m horizontal resolution and a 200x200 $km^2$ domain size as the control run configuration which underlies the results presented below.

## 6.3 Deep Convection Analysis

In this section, we first look at the spatial distribution of cloud types, water vapor, and vertical velocity surrounding the STD transition in our control simulation. We then analyze a specific vertical cross-section of a deep convection region. The analysis is based on December 23, 2014, at 15:30 LST, a day representative of the isolated deep convection during the Amazon wet season. These results help to further validate the model.

Figure 6.8a shows the horizontal distribution of cloud types (section 6.1.3). Most of the cloud cover is due to shallow cumulus, altocumulus, and cirrus clouds. Deep clouds typically consist of anvils and cirrus clouds, and the region between them is filled with shallow and congestus clouds. However, accurate identification of cloudy regions would require the evaluation of the contiguous volume of clouds instead of looking at individual pixels in isolation. For instance, most of the cirrus shown here are still part of the anvil and are misclassified because of the somewhat arbitrary choice of thresholds (Table 6.1).

Figure 6.8b shows the horizontal cross-section of the water vapor mixing ratio,

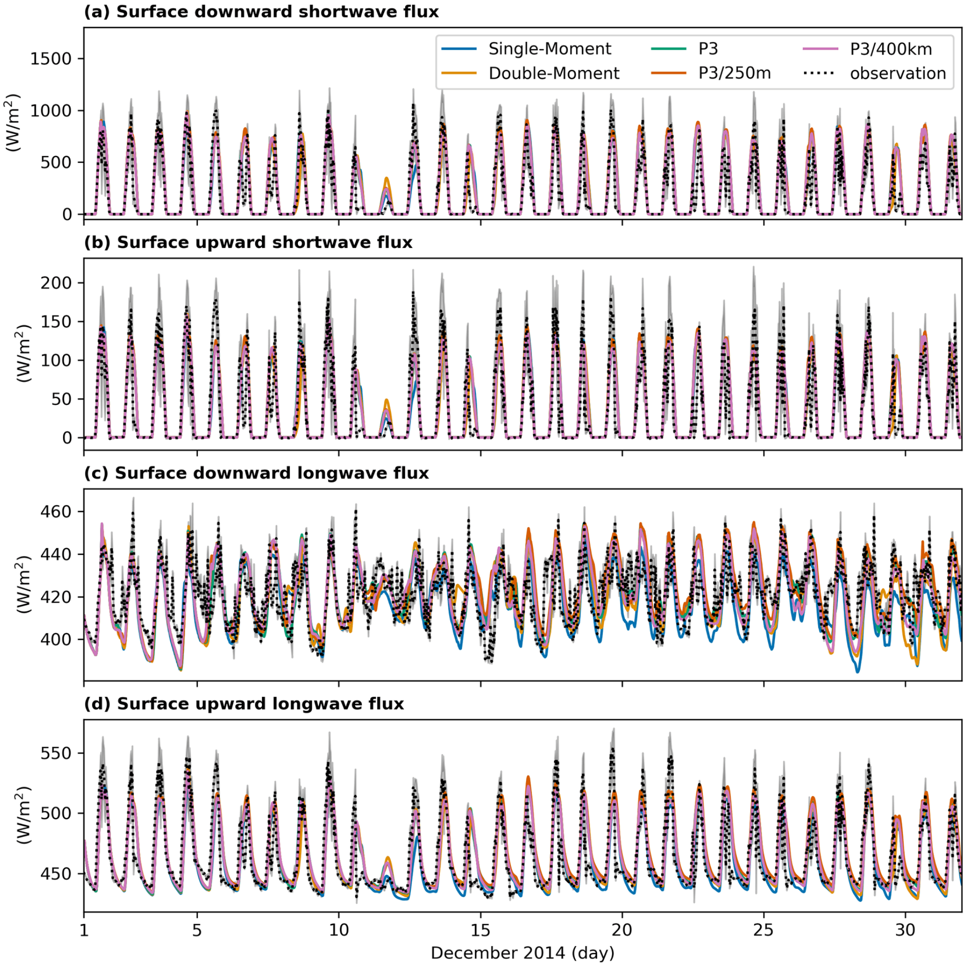

Figure 6.6 – Validation. (a) Surface downward shortwave flux. (b) Surface upward shortwave flux. (c) Surface downward longwave flux. (d) Surface upward longwave flux. The solid colored line shows the modeling results, and the black dotted line represents the observations.

$r_v$, at the 3 km level. The deep convective regions are located in areas with significant moisture, reaching values of 12 g kg$^{-1}$ or higher. In contrast, drier regions exhibit half the amount of moisture and are typically associated with shallow altocumulus or clear-sky conditions. Close inspection of the full simulation output shows that some of the clusters of shallow and congestus clouds seen in the figure, evolve into deep convective clouds.

Figure 6.8c shows the horizontal cross-section of vertical velocity at 3 km. The regions with the strongest updrafts correspond to the same regions with cumulus cloud clusters. Where these cumuli are shallow or congestus, we later observe the STD transition. Where the clouds are already deep, we observe nearby strong downdrafts and gravity waves propagating into the surroundings. While it is apparent that certain areas experiencing shallow convection may exhibit substantial water vapor and strong updrafts at low levels, Figures 6.8d-e indicate that these conditions persist exclusively during deep convection or in proximity to anvils and congestus clouds at higher altitudes.

To evaluate the deep convection properties in greater detail, we analyze the vertical

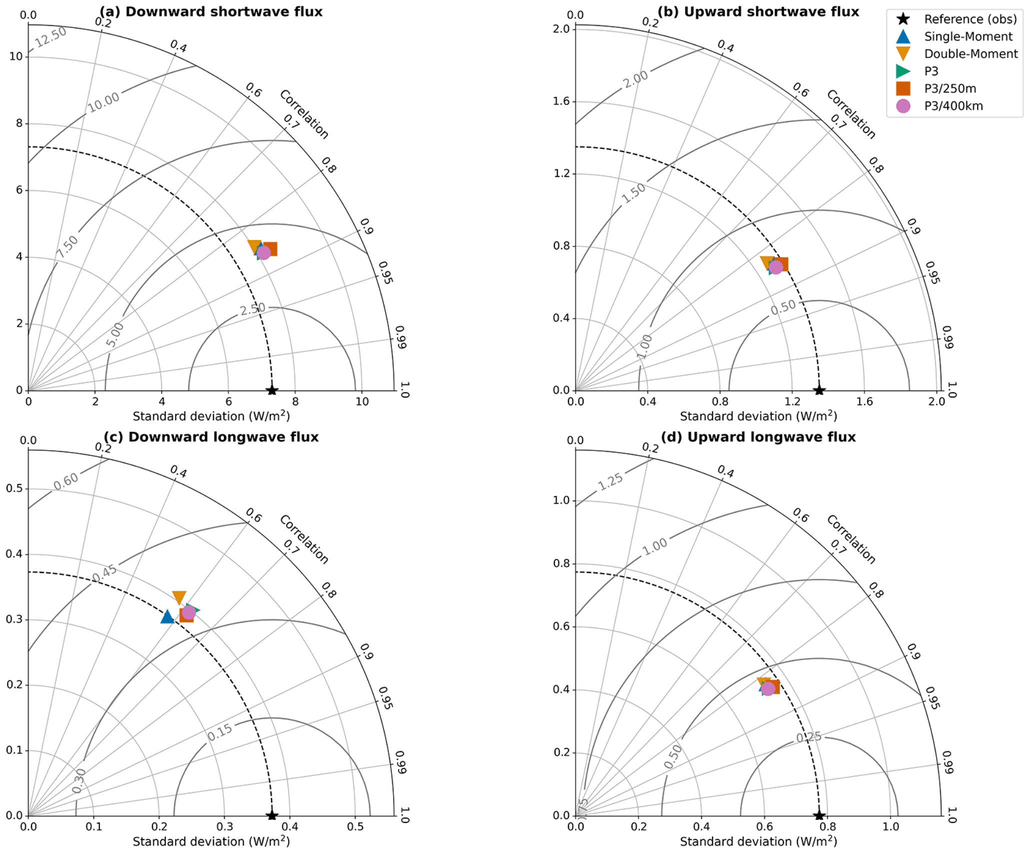

Figure 6.7 – Taylor Diagrams. (a) Surface downward shortwave flux. (b) Surface upward shortwave flux. (c) Surface downward longwave flux. (d) Surface upward longwave flux. The statistics correspond to the standard deviation of the mean and Pearson correlation.

cross-section of a deep cloud in the region shown by a vertical line in Figure 6.8a. Our aim here is to demonstrate that simulations at 500 m resolution reasonably represent inflow and outflow of the deep convective clouds.

Figure 6.9a shows the profile of cloud liquid water mixing ratio. The black contour line indicates the cloudy grid boxes (section 6.1.3) delineating the deep convective cloud. Liquid water increases from the cloud base up to 11 km, with higher values where vertical velocity is greater (Figure 6.9e). Figure 6.9b shows the total ice water (precipitating and non-precipitating). There is ice since the cloud base, possibly due to precipitating graupel, although more significant values are observed only above 4 km, with a maximum occurring between 12 and 15 km. The melting of ice might be the primary reason for the high values of rainwater observed around 4 km (Figure 6.9c), where the vertical velocity is downward (Figure 6.9e). Note that both cloud liquid and rainwater exhibit a cutoff around 11 km, which is physically consistent because liquid water cannot exist at temperatures below -40°C, a threshold known as homogeneous freezing. Congestus clouds are observed a few kilometers away, to the left and right of the deep cloud, with purely rainwater and surface-reaching precipitation, albeit with a lesser magnitude.

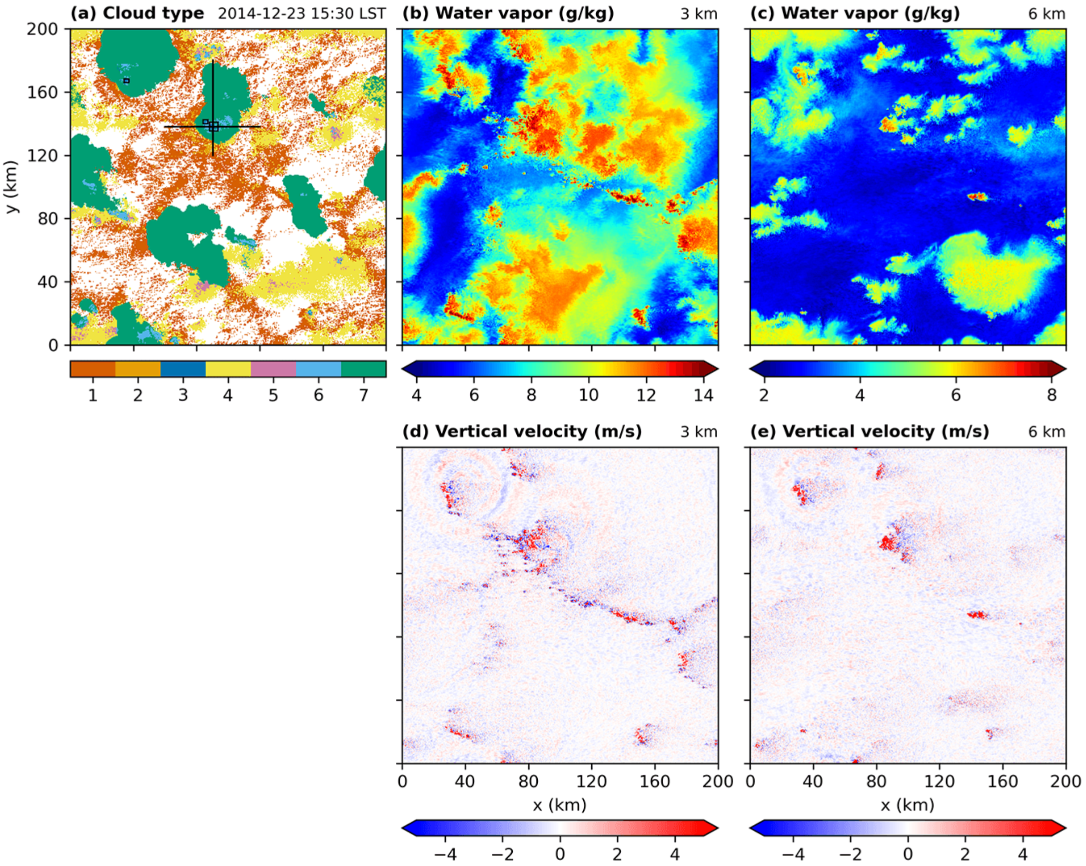

Figure 6.8 – Simulation results for 23 December 2014 at 15:30 LST. (a) Cloud type according to Table 6.1. Particularly for convective clouds, shallow cumulus is 1, congestus is 2, and deep convection is 3. The black rectangle shows the deep convection regions with contiguous area $\geq$ 2.5 km$^2$ ($\geq$ 10 pixels). The vertical line corresponds to the vertical cross-section in Figure 6.9, while the horizontal line corresponds to the vertical cross-section in Figure 6.10. Water vapor at the (b) 3 km and (c) 6 km levels. Vertical velocity at the (d) 3 km and (e) 6 km levels.

Figure 6.9d contains the anomaly in moist static energy ($\mathrm{MSE}' = \mathrm{MSE} - \overline{\mathrm{MSE}}(z)$). The anomaly is positive from a little below the cloud base up to 12 km. Negative values occur close to the surface and around the top of the deep cloud. Figure 6.9e shows the buoyancy and vertical velocity (streamlines). The negative surface values are possibly related to cold pools (TORRI; KUANG; TIAN, 2015). The positive values inside the cloud get larger with increasing altitude due to latent heat release, reaching a maximum around 10 km, and they are an indication of instability. The negative values near the cloud top could be possibly related to the dry-air entrainment at the cloud top, fluctuations around the level of neutral buoyancy, or gravity waves. Buoyancy decreases rapidly as we move away from the cloud core and into the anvil, it is slightly positive inside the deep anvil, below the cloud top, but it continuously decreases for regions farther away from the deep vertical axis (that intersects with the cloud base center), until the anvil-buoyancy becomes nearly zero coinciding with the outside region.

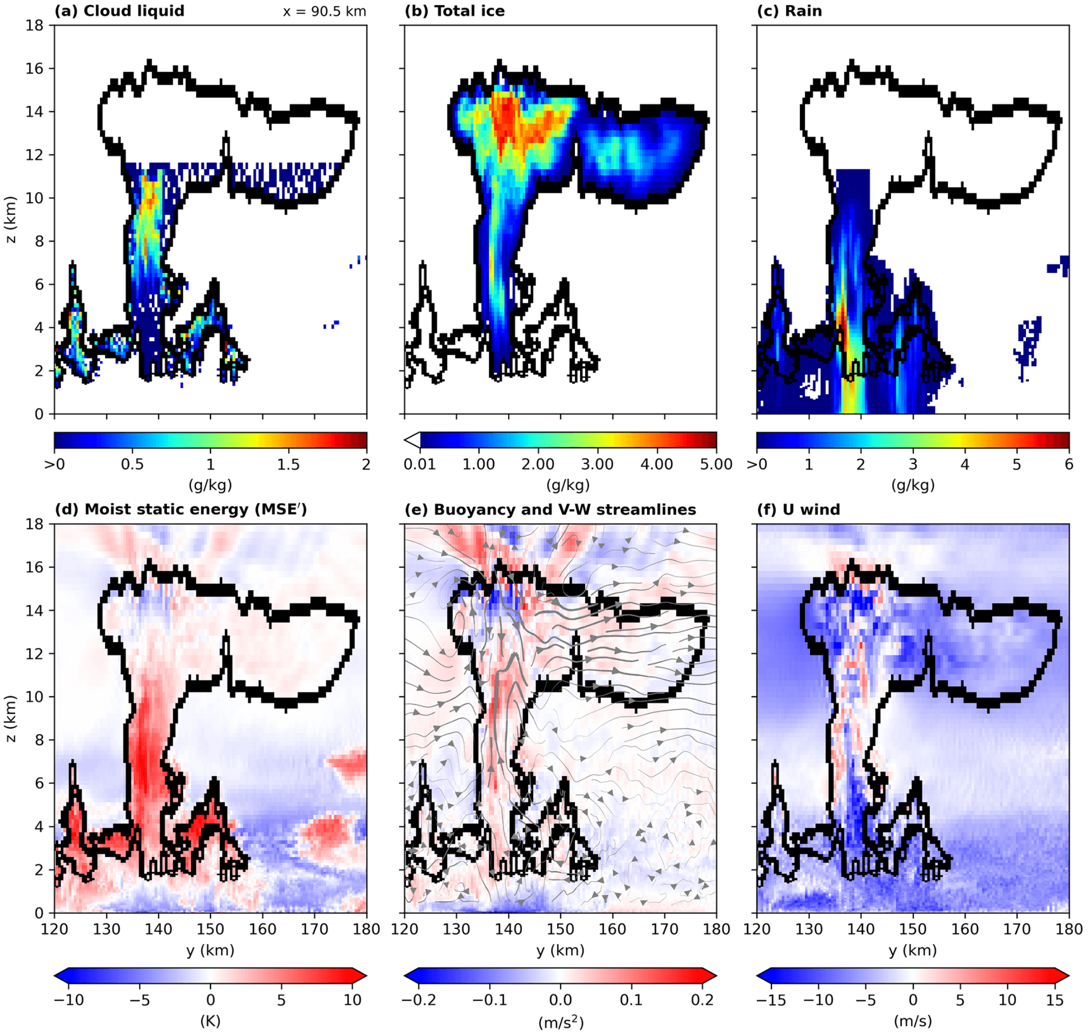

Figure 6.9 – Vertical cross-section of deep convection. Results correspond to the plane $x$ = 90.5 km for 23 December 2014 at 15:30 LST. (a) Cloud liquid. (b) Total ice water. (c) Rain content. (d) Anomaly in moist static energy (divided by $c_p$) (MSE′ = MSE - $\overline{\text{MSE}}$(z)). (e) Buoyancy and V-W wind components (streamlines). (f) U wind component. The black contour illustrates the deep convection region drawn using the cloud definition (section 6.1.3).

The vertical velocity also shows positive values inside the cloud, except in the cloud-top region and low levels (below $\sim$ 4 km). Near the surface, the V wind (Figure 6.9e) shows negative values to the right of the deep cloud, and positive values to the left, indicating the low-level convergence that brings moist air parcels into the deep convection region. Around the altitude of the level of neutral buoyancy, the updraft spreads outward forming the anvil, with the V wind now pointing northward. The U wind component (Figure 6.9f), perpendicular to the anvil direction, shows more important anomalies only inside the deep cloud. Thus, the U component of the environmental wind strongly relates to the large-scale wind, being little affected by the observed cold pools. The pattern inside the cloud provides a more regular shape to the deep cloud on the x-axis, as shown in Figure 6.10.

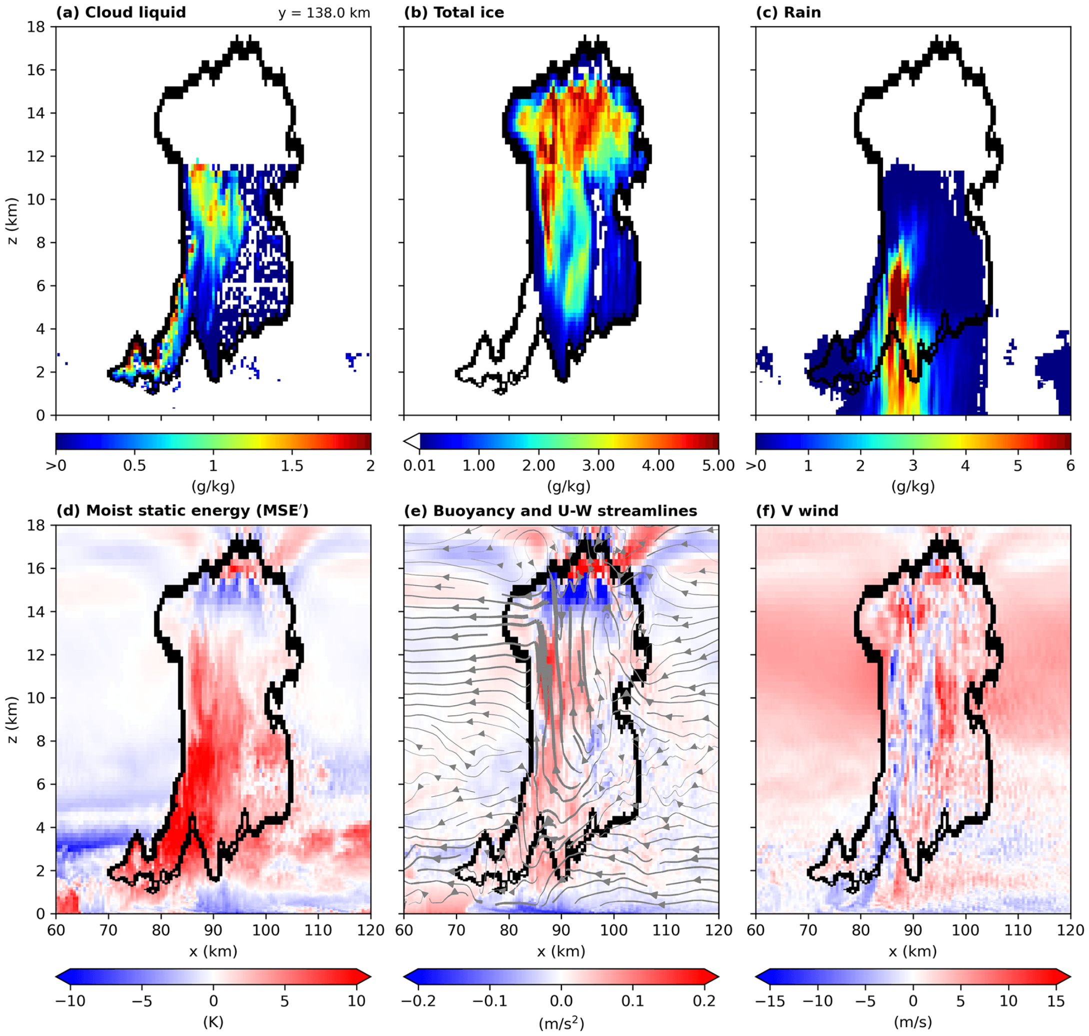

Figure 6.10 – Vertical cross-section of deep convection. Results correspond to the plane $y$ = 138.0 km for 23 December 2014 at 15:30 LST. (a) Cloud liquid. (b) Total ice water. (c) Rain content. (d) Anomaly in moist static energy (divided by $c_p$). (e) Buoyancy and U-W wind components (streamlines). (f) V wind component. The black contour illustrates the deep convection region drawn using the cloud definition (section 6.1.3).

## 6.4 Sensitivity Experiments

To evaluate the role of moisture and vertical wind shear on the STD convection transition, we performed a series of sensitivity experiments. First, we perturbed the water vapor profile in the low levels (0-1.5 km) and the free troposphere (> 3 km) to investigate the importance of low- and mid-level preconditioning. To assess the importance of moisture advection, we replaced the horizontal or vertical component of large-scale moisture tendency forcing. We simulated Deep days with the ShCu forcing, or vice versa. Finally, we varied the structure of the low or upper-level jets to evaluate the relative importance of vertical wind shear at different levels. The results in this section correspond to the mean composites of Deep or ShCu simulated days.

Figure 6.11 shows the composite of cloud liquid ($r_l$), total ice ($r_i$), and rain water ($r_r$) domain-averaged mixing ratios for the Deep and ShCu days. Both regimes exhibit a peak in $r_l$ associated with shallow convection, which is evident below 3 km between 10-14 LST. Additionally, Deep days show two peaks in $r_i$. The first occurs between 12-14 LST at upper levels ($>$ 8 km), associated with deep convection driven by surface heating (MARTIN *et al.*, 2016; TANG *et al.*, 2016; ZHUANG *et al.*, 2017; TIAN *et al.*, 2021). The second peak occurs a few hours later, between 16-18 LST, being associated with the late afternoon STD convection transition triggered by the land-atmosphere interactions.

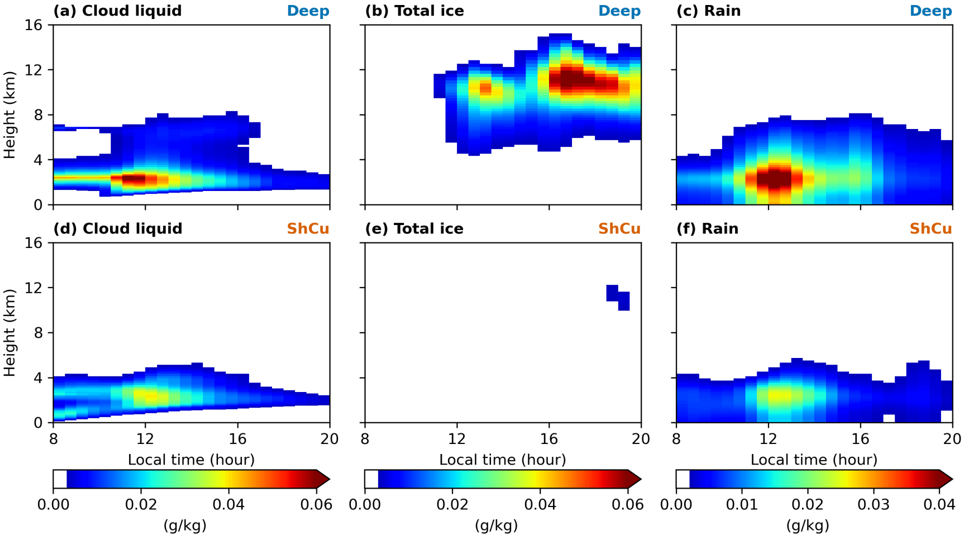

Figure 6.11 – Composites for the Deep (top) and ShCu regime days showing the diurnal cycle of domain-averaged (a,d): Cloud liquid water, (b,e): Total ice, and (c,f): Rain content. Results for control simulation for December 2014, from which 4 Deep (17, 21, 23, and 26) and 4 ShCu days (9, 13, 27, and 28) days were selected (section 6.1.4).

### 6.4.1 Low-Level Moisture Experiment

The low-level moisture experiment consisted in applying a moisture perturbation in the bottom 1.5 km of the domain at 02 LST of each one of the four Deep days selected. As a perturbation in the model displaces it from its current equilibrium, applying the perturbation overnight guarantees sufficient time for the model to return to an equilibrium state before the afternoon, ensuring consistent results during the period of interest when the STD transition occurs. The perturbation was introduced by multiplying the water vapor mixing ratio by a factor $\beta < 1$. In order to ensure smoothness of the water vapor profile, we linearly interpolated $\beta$ to 1 between 1.25 km and 1.75 km. We tested several factors and selected ones that provide representative results for the effects of the low-level moisture experiment, which correspond to the values of $\beta$ = 0.80, 0.85, and 0.90. It is worth noting that we needed to modify the SAM source code to incorporate the perturbation during the restart, as described above.

The results show that the dry perturbations diminish throughout the day but are still present at 20 LST (see Figure 6.12). Above the perturbed region, the mixing ratio values are very similar, indicating little vertical mixing. During the afternoon and early evening, the water vapor profile in experiments using factors $\beta_{0.85}$ and $\beta_{0.90}$ closely resembles that of the ShCu days (control).

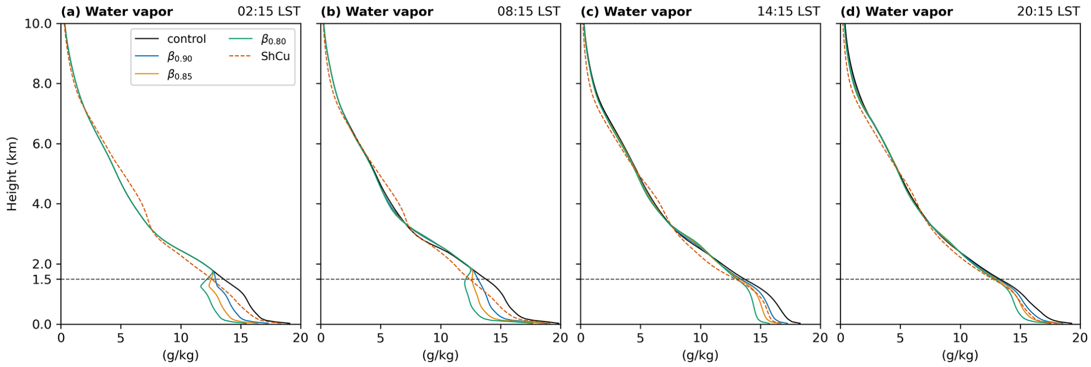

Figure 6.12 – Low-level moisture experiment. Water vapor profile at (a) 02:15 LST, (b) 08:15 LST, (c) 14:15 LST, and (d) 20:15 LST. The black line is the control (Deep composite) simulation, and the colored line represents the sensitivity experiments for the factors 0.9 (blue), 0.8 (orange), and 0.7 (green). We also show the ShCu composite (dashed red line).

Figure 6.13 shows the magnitude (colors) and relative (contours) difference between experiment and control case for cloud liquid, total ice, and rain domain-averaged mixing ratios. Cloud liquid water is reduced up to 75% near the cloud base, with a more extensive impact observed for drier scenarios from 10 to 12 LST. Interestingly, above 3 km, near the shallow cloud top, the opposite effect is found. This positive anomaly extends higher later in the day (e.g., $\sim$ 6 km at 16 LST). These higher values at mid-levels for drier low-level conditions are most likely a consequence of more mid-level detrainment from more frequent congestus clouds, as deep clouds are suppressed.

Ice water content is significantly reduced for drier low-level conditions. Although factor $\beta_{0.90}$ significantly affects the ice content (reduction of $\sim$ 50-75%), there is still a late-afternoon deep convection transition over reduced areas. Conversely, the experiments with factors $\beta_{0.85}$ and $\beta_{0.80}$ show only a negligible quantity of ice, with the first peak (12-14 LST) in ice water being completely removed and the second peak (16-18 LST) showing a reduction of at least 75% in mixing ratio. In these cases, the resulting ice profile is comparable to what we observed in the ShCu composite (Figure 6.11e). Since $\beta_{0.85}$ provides an environmental condition similar to ShCu days, preconditioning of lower levels possibly plays an essential role in the late afternoon STD convection transition.

For rain content, the experiment with factor $\beta_{0.90}$ shows a reduction of about 50% from 08 to 12 LST. Factor $\beta_{0.85}$ shows a reduction of about 75% in the same period, but it extends up to 14 LST at higher levels (above 4 km). A similar reduction is also observed

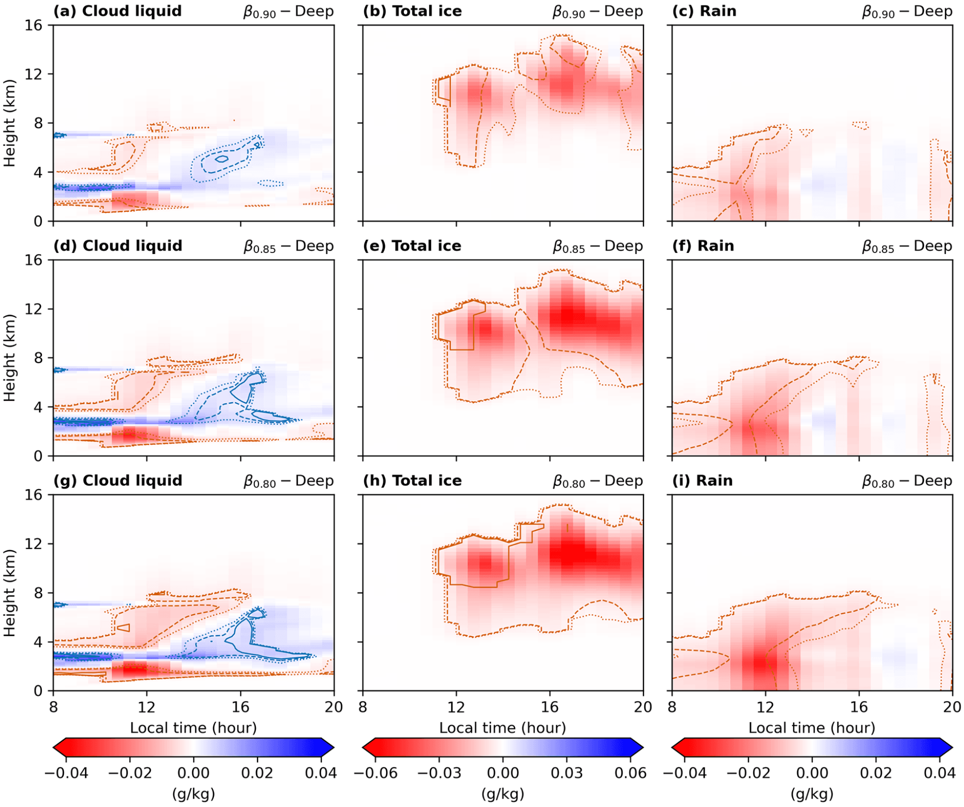

Figure 6.13 – Low-level moisture experiment. The composites show the diurnal cycle of domain-averaged anomalies for (a,d,g) Cloud liquid water, (b,e,h) Total ice, and (c,f,i) Rain content. Each row corresponds to an experiment for a different factor: (a-c) $\beta_{0.90}$, (d-f) $\beta_{0.85}$, and (g-i) $\beta_{0.80}$. The colors indicate the difference between experiment and control case, while the contours show the relative difference. The dotted line shows either an increase (blue) or decrease (red) in mixing ratio of 50%, the dashed line indicates 75%, and solid line corresponds to 100%. The simulations were conducted for the Deep days.

for factor $\beta_{0.80}$, but in this case, it extends to later in the day (16 LST). Figure 6.14 shows the domain-averaged precipitation rate for each experiment. The drier scenarios (Figure 6.14a) are associated with less intense precipitation peaking later during the day. While the Deep case shows a peak of 0.86 mm day$^{-1}$ at 12:15 LST, the drier experiment ($\beta = 0.80$) presents a peak of 0.30 mm day$^{-1}$ at 13:45 LST. These could be related to moisture and instability conditions necessary to promote precipitation, which occurs earlier for the moister scenarios, resulting in earlier precipitation which, in turn, stabilizes the troposphere.

### 6.4.2 Free Troposphere Moisture Experiment

Next, we tested the sensitivity of the STD transition to free-tropospheric moisture. Analogously to the previous section, the experiments consisted of applying a perturbation to the water vapor profile at 02 LST of each one of the four Deep days selected. In this

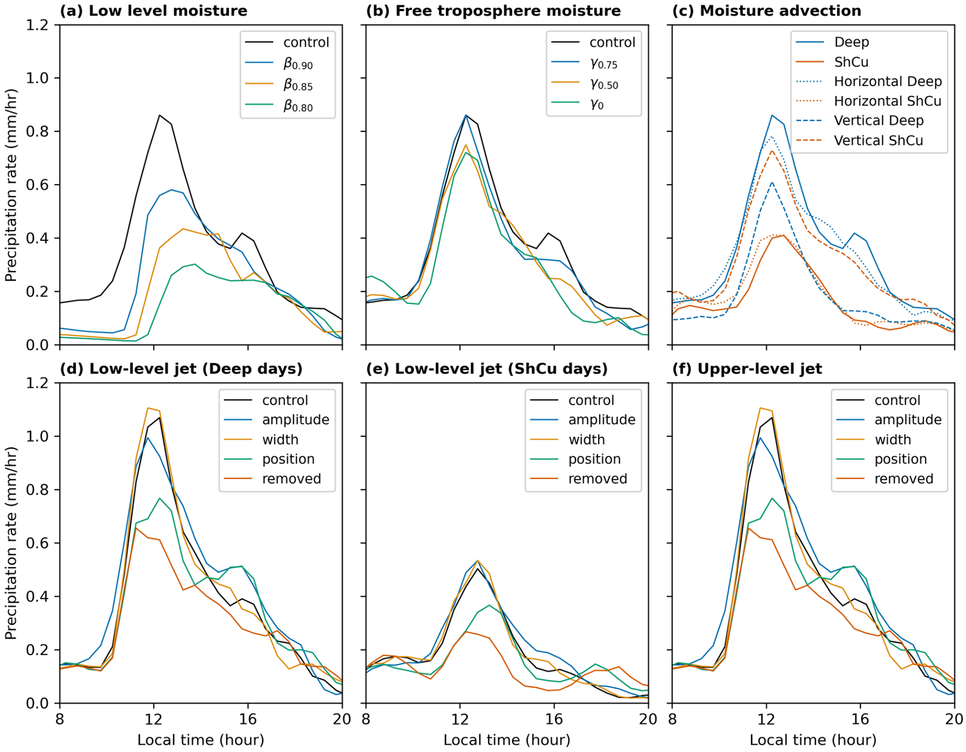

Figure 6.14 – Precipitation rate for each sensitivity experiment. (a) Low-level moisture experiment. (b) Free troposphere moisture experiment. (c) Moisture advection experiment. (d) Low-level jet experiment conducted during the Deep days. (e) Low-level jet experiment conducted during the ShCu days. (d) Upper-level jet experiment.

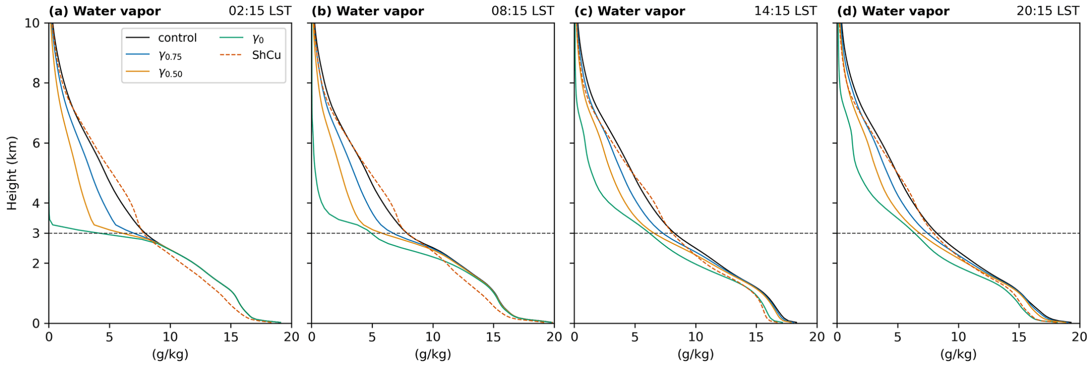

Figure 6.15 – Free troposphere moisture experiment. Water vapor profile at (a) 02:15 LST, (b) 08:15 LST, (c) 14:15 LST, and (d) 20:15 LST. The black line is the control (Deep composite) simulation, and the colored line represents the sensitivity experiments for the factors 0.75 (blue), 0.50 (orange), and 0 (green). We also show the ShCu composite (dashed red line).

case, however, we applied a factor $\gamma < 1$ above 3 km. We opted to perturb the moisture profile from 3 km, above the low levels, to prevent the influence of lower levels from affecting simulations aimed at evaluating sensitivity in the mid and upper levels. We also tested several factors and selected ones that provide representative results for the effects of the free troposphere moisture experiment, which correspond to the values of $\gamma = 0.00$, 0.50, and 0.75.

The dry perturbations in the free troposphere diminish throughout the day but not as rapidly as the low-level perturbations (compare Figure 6.15 and 6.12). Mixing with low-level moisture starts from the top of the boundary layer, thus the simulations for smaller factors $\gamma$ exhibit drier low-level conditions between 3 and 1.5 km by early afternoon. The exception is the extreme case of removing all free-troposphere moisture, where the whole boundary layer becomes drier. Contrasting these experiments with the ShCu composite reveals that the shallow days have drier conditions throughout the morning only in the lower troposphere, below 3 km.

Figure 6.16 shows the magnitude (colors) and relative (contours) difference between the experiment and control case for cloud liquid, total ice, and rain domain-averaged mixing ratios. Cloud liquid water has low sensitivity to the amount of water vapor mixing ratio in the free troposphere. The contours indicating a reduction of 50-75% are associated to regions with only little amount of $r_l$ ($< 0.02$ g kg$^{-1}$, Figure 6.11a). Interestingly, for the drier experiment ($\gamma_0$), $r_l$ decreases above the boundary layer (1.5 to 3 km) and increases immediately above the perturbation ($\sim$ 3-4 km). This could potentially be related to lesser low-level clouds and faster detrainment of moister air as these clouds penetrate the dry layer above.

Moisture in the free troposphere affects the cloud ice water during the afternoon, with anomalies ranging from 50% (factor $\gamma_{0.75}$) to 75% (factor $\gamma_0$). The late afternoon peak in $r_i$ is only completely removed in the extremely dry case ($\gamma_0$), although some residues of ice are still observed during the day. However, the factor $\gamma_{0.75}$ already corresponds to a significantly dry environment. This indicates that the free troposphere preconditioning plays a minor role in convection in the Amazon, with only a weak impact on high cloud cover.

The rain content does not always decrease for the drier experiments. In fact, $r_r$ slightly increases or decreases depending on the time and altitude for factors $\gamma_{0.75}$ or $\gamma_{0.50}$. For these experiments, a reduction of 50% is observed only for regions with little amount of $r_r$ ($< 0.01$ g kg$^{-1}$, Figure 6.11c). As seen for $r_l$, $r_r$ increases just above the perturbation between 08-16 LST for the extremely dry case. After 16 LST, $r_r$ is smaller in the entire troposphere for factor $\gamma_0$. At the surface, the drier scenarios are associated with lower precipitation rates (Figure 6.14b). The peak of precipitation occurs at 12:15 LST for all experiments, but the magnitude varies from 0.86 mm day$^{-1}$ (Deep case and factor $\gamma_{0.75}$) to 0.72 mm day$^{-1}$ (factor $\gamma_0$). The relative difference in precipitation is more important on the late afternoon. Particularly at 16:15 LST, precipitation varies from 0.39 mm day$^{-1}$ (Deep case) to 0.18 mm day$^{-1}$ (factor $\gamma_0$), where the corresponding reduction in $r_r$ is about 50%.

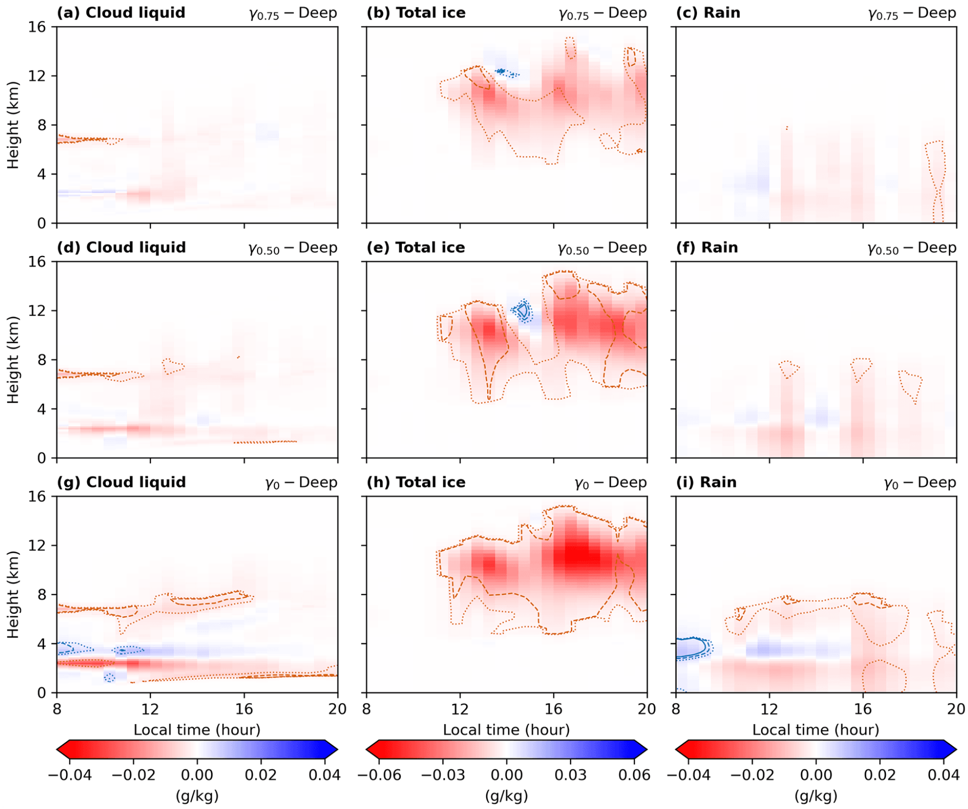

Figure 6.16 – Free troposphere moisture experiment. The composites show the diurnal cycle of domain-averaged anomalies for (a,d,g) Cloud liquid water, (b,e,h) Total ice, and (c,f,i) Rain content. Each row corresponds to an experiment for a different factor: (a-c) $\gamma_{0.75}$, (d-f) $\gamma_{0.50}$, and (g-i) $\gamma_{0}$. The colors indicate the difference between experiment and control case, while the contours show the relative difference. The dotted line shows either an increase (blue) or decrease (red) in mixing ratio of 50%, the dashed line indicates 75%, and solid line corresponds to 100%. The simulations were conducted for the Deep days.

### 6.4.3 Moisture Advection Experiment

To evaluate the importance of moisture advection, we simulated the days with the STD transition again, but this time applying the large-scale horizontal or vertical moisture tendency from the composite of ShCu days (Figure 6.17). For each Deep day, the model was restarted from the control run at 02 LST. We also performed the reversed experiment, i.e., we simulated the ShCu days but applying the large-scale moisture tendencies from the Deep days. The results are shown in Figure 6.18.

Although the horizontal tendencies exhibit significant values below the mid-levels ($< 6$ km), they are somewhat comparable on average for both Deep and ShCu days. Thus, the experiment on horizontal moisture advection shows minimal impact on the simulated cloud liquid water and rain content. The sensitivity experiments for ShCu days show little impact on convection, and the simulated days are still ShCu days. Only the ice content on Deep days is importantly affected by the ShCu composite of horizontal advection. The

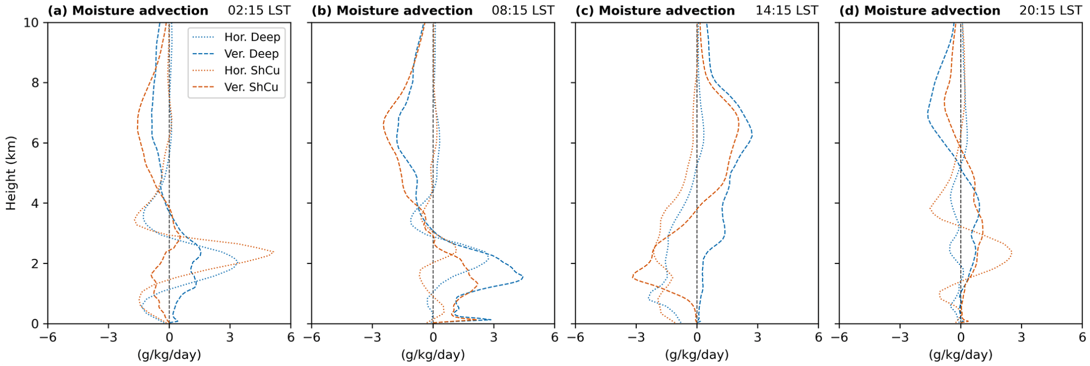

Figure 6.17 – Moisture advection experiment. Horizontal (dotted line) and vertical (dashed line) tendency of water vapor at (a) 02:15 LST, (b) 08:15 LST, (c) 14:15 LST, and (d) 20:15 LST. The blue line shows the Deep composite and the red line indicates the ShCu composite.

reduction is usually around 50%, but it can reach up to 75% around 12 km at 13 LST and around 8 km at 20 LST. A positive anomaly reaching 100% is also observed above 12 km at 15 LST, but this is a minor effect associated with changes in small values of ice mixing ratio. Despite these anomalies, the STD transition still occurs, and there is little impact on the surface precipitation (Figure 6.14c). Thus, the horizontal advection seems only to modulate the cloud ice content, particularly at the deep anvil region.

On the other hand, the vertical moisture advection greatly impacts the simulated clouds. The Deep days forced with vertical advection from ShCu days show lower mixing ratio values for all water species, while the ShCu days forced with vertical advection from Deep days show higher water content. The vertical tendency for the ShCu composite at 14 LST (Figure 6.17c) shows a drying of the low levels in the afternoon, affecting the congestus growth and suppressing the STD transition. The vertical tendency for the Deep composite from nighttime to early morning (Figure 6.17a-b) contributes to humidifying the low-troposphere, facilitating convection during the day. Thus, the ShCu days experiment shows a modest increase in ice content associated with the STD transition, although the amount of ice is still significantly lower than the observed for the Deep control case. Conversely, the STD transition is substantially suppressed for the Deep days (ice content drops up to 75%), although it still presents higher ice content than the observed for the ShCu control case.

### 6.4.4 Wind Jet Experiment

Finally, to assess the impact of the wind shear on the deepening of convective clouds in the Amazon, we performed sensitivity experiments in which the low- or high-level jets were modified. While the mean wind profile for the entire wet season (December-April) does not differ significantly from that during December 2014, it exhibits smoother features. Thus, we idealized the control wind speed for the jet experiments by adjusting

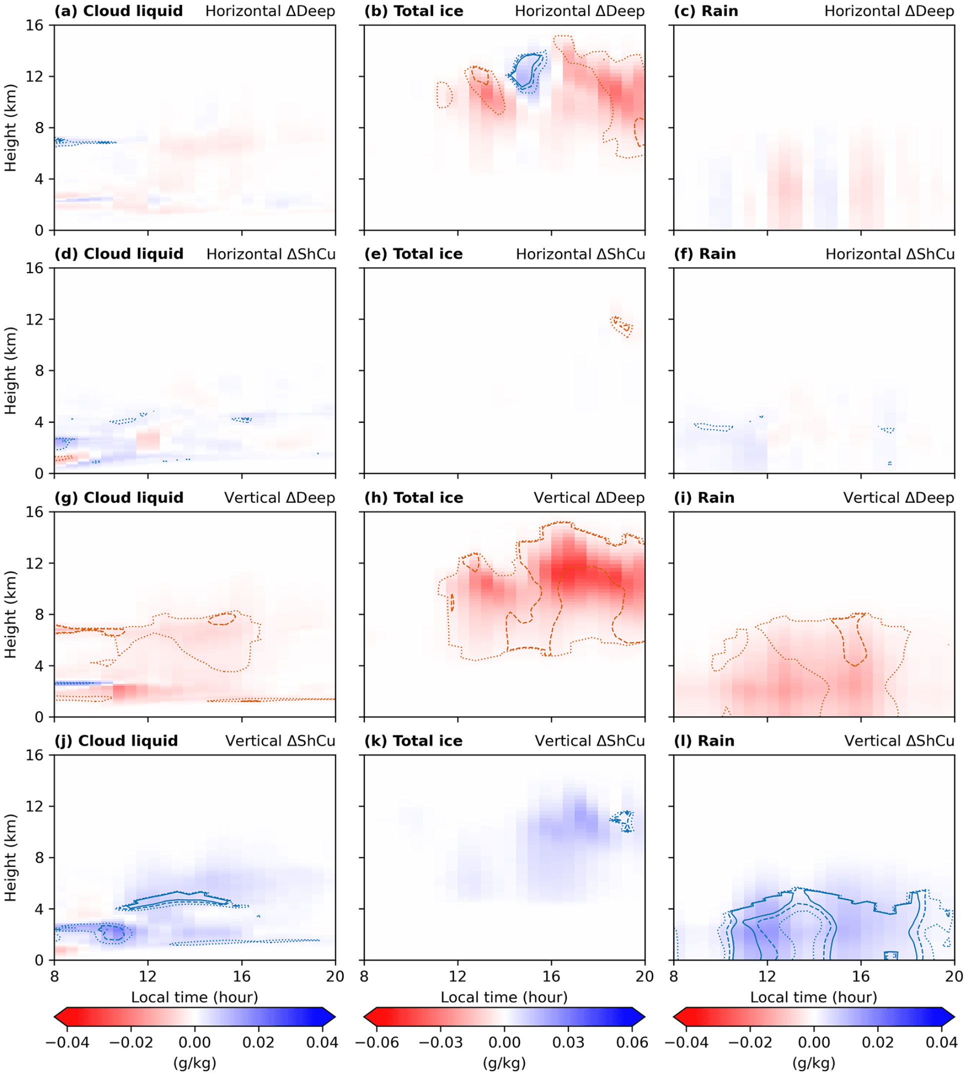

Figure 6.18 – Moisture advection experiment. The composites show the diurnal cycle of domain-averaged anomalies for (a,d,g,j) Cloud liquid water, (b,e,h,k) Total ice, and (c,f,i,l) Rain content. Experiment applying a different horizontal tendency during (a-c) Deep and (d-f) ShCu days. Experiment applying a different vertical tendency during (g-i) Deep and (j-l) ShCu days. The colors indicate the difference between experiment and control (a-f: Deep composite, g-l: ShCu composite) case, while the contours show the relative difference. The dotted line shows either an increase (blue) or decrease (red) in mixing ratio of 50%, the dashed line indicates 75%, and solid line corresponds to 100%.

two Gaussian functions in the observed wind profile during the wet season (Figure 6.19a):

$$v_{spd}(z) = v_0 + a_1 \exp\left(-\frac{(z-\overline{z}_1)^2}{2\sigma_1^2}\right) + a_2 \exp\left(-\frac{(z-\overline{z}_2)^2}{2\sigma_2^2}\right) \tag{6.1}$$

where $v_0 = 0.5$ m s$^{-1}$, $a_1 = 8.4$ m s$^{-1}$, $\overline{z}_1 = 2.1$ km, $\sigma_1 = 1.6$ km, $a_2 = 5.4$ m s$^{-1}$, $\overline{z}_2 = 11.75$ km, and $\sigma_2 = 2.5$ km. The parameters $a_i$ control the jets amplitudes, $z_i$ the jets positions, and $\sigma_i$ their widths.

The wind direction was idealized using a piece-wise linear approximation (Figure

6.19b). Direction is constant in the bottom ~2 km. It veers clockwise at a constant rate of about 14° $\text{km}^{-1}$ from 2 to 15 km, and counterclockwise at a rate of -28° $\text{km}^{-1}$ from 15 to 20 km. The wind direction is constant above 20 km.

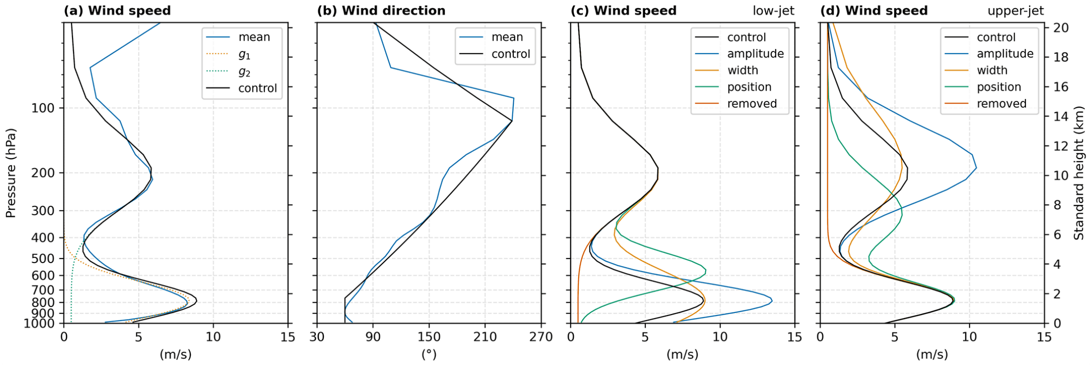

Figure 6.19 – Wind profiles for the jet experiments control run showing: (a) large-scale wind speed and (b) wind direction, as measured (blue) and as idealized (black). Sensitivity experiments perturbed the wind speed profile of either the (c) low-level or (d) upper-level wind jets, by intensifying (blue), widening (orange), shifting (green), or removing the jet (red).

For each jet, we conducted 4 experiments in which we (1) increased the jet amplitude, (2) increased the width, (3) shifted the peak position, and (4) removed the jet entirely, while keeping the wind direction constant in all cases. The modified wind profiles are shown in Figures 6.19c-d. For each experiment, the model was restarted from the control run at 02 LST of each one of the four Deep or ShCu days selected. These are compared with additional control runs, this time considering the idealized wind profile.

Figure 6.20 shows the anomaly results between the low-level jet experiments and the control jet case during Deep days. While the jet position significantly affects cloud liquid water, the jet width shows a negligible impact. The higher position possibly favors the low-level updrafts, which increases $r_l$ above 2 km, especially in the late afternoon (around 16 LST), when $r_l$ increases by up to 100%. The experiment removing the low-level jet also exhibits a similar impact on cloud liquid water, although the anomalies are relatively smaller than those associated with the jet position. The stronger jet only slightly impacts the cloud liquid water. While $r_l$ is increasing up to 75% around 4 km at 15 LST, this is a minor effect given the small values of mixing ratio at this altitude.

The cloud ice content is more significantly affected by the low-level wind jet. For the stronger jet, positive anomalies dominate before 12 and after 16 LST, when $r_i$ can increase by up to 100%, with negative anomalies observed in between. These suggest that a stronger low-level jet is associated with an earlier peak of precipitation due to surface fluxes, while the late afternoon STD transition occurs later. For the wider jet, a positive anomaly dominates throughout the diurnal cycle, especially around 12 and 16 LST, when $r_i$ shows an increase of up to 100% above 12 km. The higher jet shows a decrease ranging

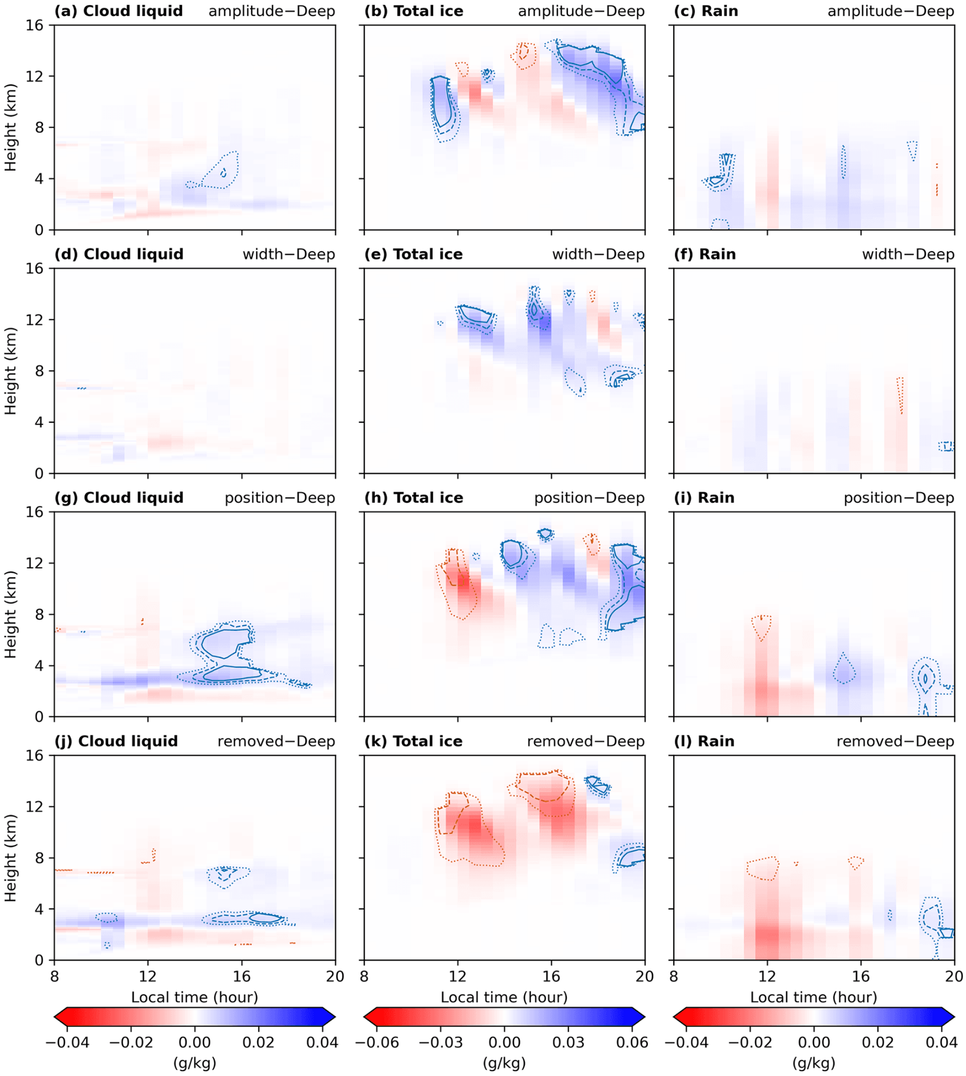

Figure 6.20 – Low-level jet experiment. The composites show the diurnal cycle of domain-averaged anomalies for (a,d,g,j) Cloud liquid water, (b,e,h,k) Total ice, and (c,f,i,l) Rain content. Experiments for the jet (a-c) amplitude, (d-f) width, (g-i) position, and (j-l) low-level jet removed entirely (see Figure 6.19c). The colors indicate the difference between the experiment and the jet control case, while the contours show the relative difference. The dotted line shows either an increase (blue) or decrease (red) in mixing ratio of 50%, the dashed line indicates 75%, and solid line corresponds to 100%. The simulations were conducted for the Deep days.

from 50-75% in $r_i$ between 8-12 km around 12 LST. After that, $r_i$ increases, especially above 12 km, where the relative anomaly can reach up to 100% between 14-16 LST. After 18 LST, $r_i$ also shows an increase of up to 100%. Thus, convection is reduced around noon and enhanced in the late afternoon, with the deep clouds lasting longer. When the low-level jet is removed, the high clouds are substantially suppressed (up to 75%), although the STD transition still occurs later in the day, and surface precipitation increases after the second peak (17 LST) (see Figure 6.14d).

Rain content follows the changes in total ice mixing ratio, with negative (positive) anomalies where ice decreased (increased). However, changes in $r_r$ are less significant, with smaller areas showing changes greater than 50%.

Figure 6.21 shows the results for similar sensitivity tests conducted on ShCu days. In all experiments, the effects are similar to those found in Deep days, but much less pronounced. Higher or missing jets suppressed rain around noon, increasing it early evening, but in the warm phase only. More importantly, stronger or wider jets produced negligible changes in the ice mixing ratio and did not trigger the STD transition.

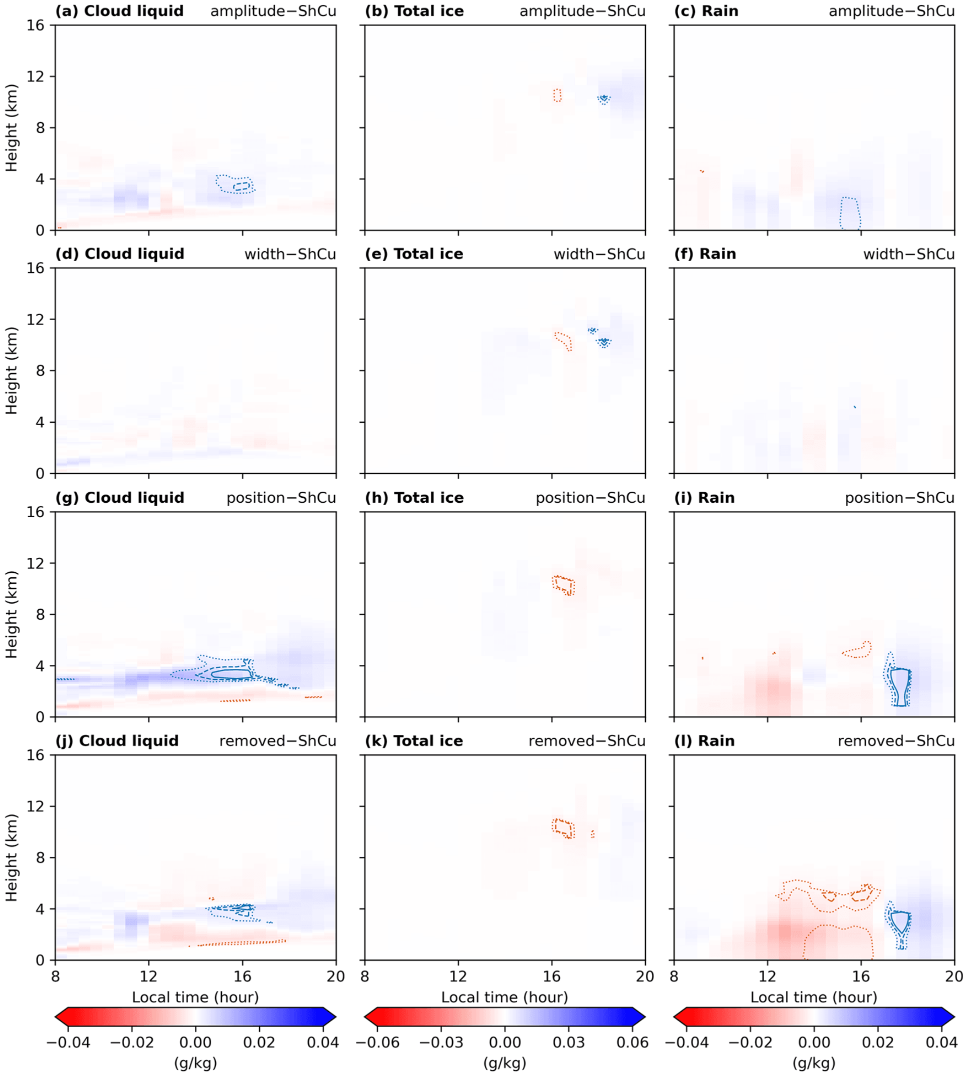

Figure 6.21 – Low-level jet experiment. The composites show the diurnal cycle of domain-averaged anomalies for (a,d,g,j) Cloud liquid water, (b,e,h,k) Total ice, and (c,f,i,l) Rain content. Experiments for the jet (a-c) amplitude, (d-f) width, (g-i) position, and (j-l) low-level jet removed entirely (see Figure 6.19c). The colors indicate the difference between the experiment and the jet control case, while the contours show the relative difference. The dotted line shows either an increase (blue) or decrease (red) in mixing ratio of 50%, the dashed line indicates 75%, and solid line corresponds to 100%. The simulations were conducted for the ShCu days.

Figure 6.22 shows the anomaly results between the upper-level jet experiments and the control jet case during Deep days. First, the upper-level jet affects convection only in the high troposphere, with no effects on the liquid water or rain content. The stronger upper-level jet shows a greater reduction in ice content during the afternoon, although the anomalies are usually under 50%. However, after 17 LST, all experiments show an increase of up to 100% in ice water. The results between the wider jet and stronger jet differ around noon time, when the ice content slightly increases for the wider jet case, although it is usually under 50%. The shifted or removed jet experiment show an analogous behavior to the wider jet, but the observed anomalies are slightly greater. Nevertheless, these anomalies are more minor than those observed for the low-level wind shear, and it contributes especially to the delay of the late afternoon STD transition.

## 6.5 Discussion

We conducted numerical simulations using the SAM model coupled with a Surface Land Model (SLM) for December 2014. Despite our idealized surface, the model reproduced consistent values of surface fluxes after we employed a comprehensive effort to adjust the SLM parameters. We also tested the performance of the single-moment, double-moment, and P3 microphysics schemes. The only variable that exhibited a noticeable sensitivity to the microphysics scheme was the column water vapor, where the P3 scheme demonstrated a stronger correlation with the observations. Compared with previous work addressing the model sensitivity to microphysics, model domain, and resolution (KHAIROUTDINOV; RANDALL, 2003; KHAIROUTDINOV; RANDALL, 2006; BLOSSEY *et al.*, 2007; KHAIROUTDINOV *et al.*, 2009; HENDERSON; PINCUS, 2009; LIU; MUHLBAUER; ACKERMAN, 2015; BLOSSEY; BRETHERTON; MOHRMANN, 2021), this thesis focused specifically on the Amazon region and considered the calculation of surface fluxes through the SLM. Although the recent work by GONÇALVES *et al.* (2022) employed the GoAmazon2014/5 observations, they did not assess the evolution of moisture content and surface latent and sensible heat fluxes. The work by LEBO; MORRISON (2015) indicated that the convective characteristics between the horizontal resolution of 500 and 250 m exhibit sudden changes, specifically the mean convective updraft mass flux and tracer transport. Despite this resolution threshold, our results did not show a relevant impact during the 1-month simulated period between the simulations with 500 m or 250 m for the P3 microphysics scheme.

We also conducted a detailed validation of the 3D fields for our control simulation (P3 scheme, with a resolution of 500 m and a domain size of 200x200 km$^2$) on 23 December 2014 at 15:30 LST. While both regions associated with shallow and deep convection may exhibit substantial moisture content at low levels, these conditions only remain nearby of deep convection at higher levels. This is a reasonable result, being associated with water vapor convergence (ADAMS *et al.*, 2013; ADAMS; BARBOSA; RíOS, 2017) and detrain-

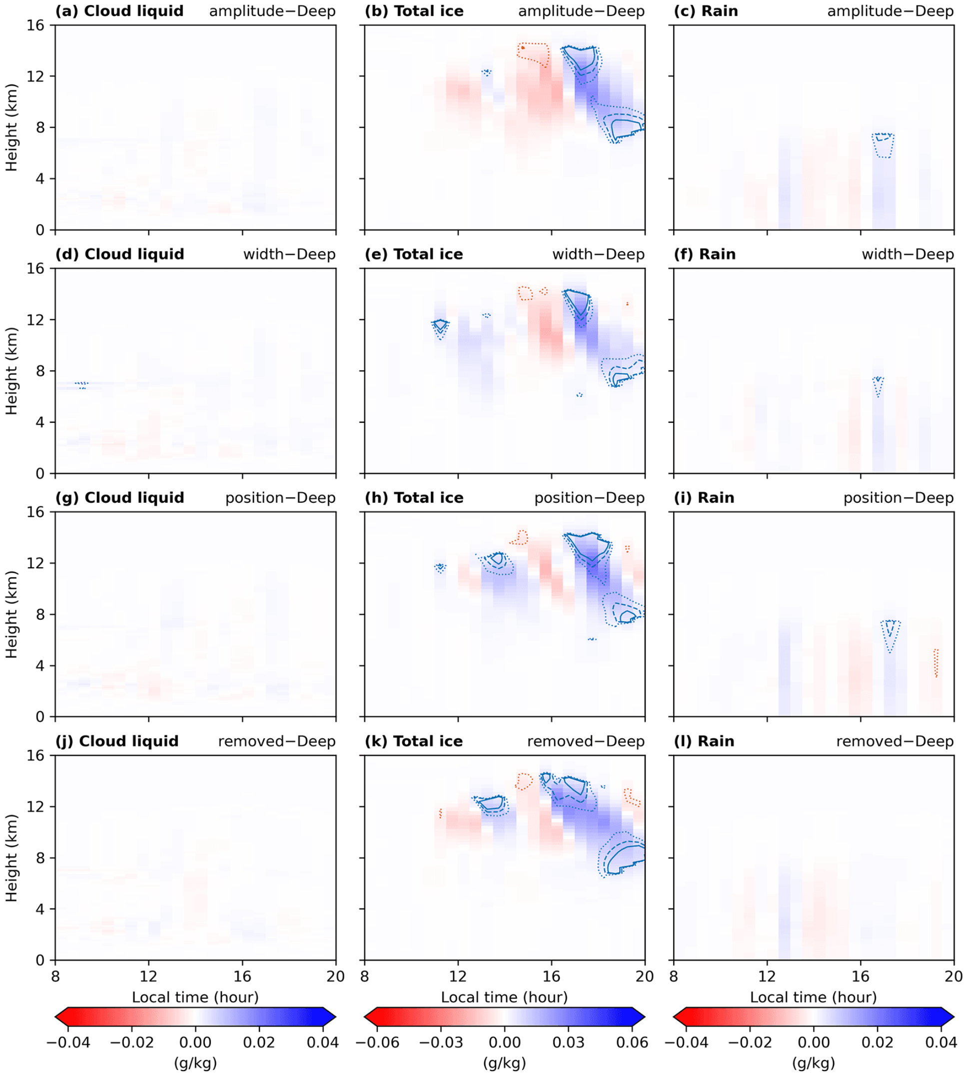

Figure 6.22 – Upper-level jet experiment. The composites show the diurnal cycle of domain-averaged anomalies for (a,d,g,j) Cloud liquid water, (b,e,h,k) Total ice, and (c,f,i,l) Rain content. Experiments for the jet (a-c) amplitude, (d-f) width, (g-i) position, and (j-l) upper-level jet removed entirely (see Figure 6.19d). The colors indicate the difference between the experiment and the jet control case, while the contours show the relative difference. The dotted line shows either an increase (blue) or decrease (red) in mixing ratio of 50%, the dashed line indicates 75%, and solid line corresponds to 100%. The simulations were conducted for the Deep days.

ment of water vapor from congestus and deep clouds (JOHNSON *et al.*, 1999; WAITE; KHOUIDER, 2010). Gravity waves may also propagate near deep convection areas, which is consistent with their importance in redistributing heat and moisture (BRETHERTON; SMOLARKIEWICZ, 1989). Cold pools are formed along deep convection regions. Inside the deep cloud, a significant positive anomaly in MSE and positive buoyancy are observed below the anvil. Above that, near the cloud top, a negative anomaly in MSE and negative buoyancy prevails, which could be related to the entrainment of drier air at the cloud top and gravity waves. These characteristics of deep convection are in line with the findings of KHAIROUTDINOV; RANDALL (2006), which conducted idealized high-resolution simulations over the Amazon. Moreover, these observations are consistent with our current understanding of tropical convection (COTTON; BRYAN; HEEVER, 2011; KRISHNAMURTI; STEFANOVA; MISRA, 2013).

Sensitivity experiments showed that low-level preconditioning is critical to deep convection. The drying experiments were associated with more extensive low cloud cover, while the ice content and vertical cloud development were strongly suppressed. The experiments also showed that free troposphere preconditioning impacts the vertical development between the congestus and deep phase only in extremely dry scenarios, which does not occur naturally in the Amazon region. While KHAIROUTDINOV; RANDALL (2006) conducted experiments that differed from those designed in this study and were limited to a single idealized case during TRMM-LBA on February 23, 1999, they similarly indicated that free troposphere preconditioning plays a minor role in convection. Based on GoAmazon2014/5 observations, GHATE; KOLLIAS (2016) noted that locally-driven precipitating days during the dry season exhibit a water vapor excess above 2 km since early morning. Conversely, ZHUANG *et al.*; TIAN *et al.* (2017, 2021) found that deep convective days show a moister profile, starting from the surface and independent of the season. Our findings align with the studies conducted by ZHUANG *et al.*; TIAN *et al.* (2017, 2021), as we observed that low-level humidity plays a critical role in convection. However, our results differ from the findings of GHATE; KOLLIAS (2016), as we showed that the free troposphere humidity does not significantly impact precipitation. Moreover, since convection occurs over relatively drier conditions during the dry season, the importance of low-level preconditioning may be even more pronounced.

Experiments with the large-scale horizontal and vertical moisture advection used to force the SAM model hinted on their distinct roles on the STD transition. We found that horizontal advection weakly modulated the ice content for the Deep simulated days. On the contrary, the vertical moisture advection significantly contributed to convection in both ShCu and Deep days. Our results suggest that vertical advection is associated with a drying of the low levels in the afternoon of ShCu days. On the other hand, there is a moistening of these levels in Deep days, from nighttime to afternoon, which facilitates the late afternoon STD convection transition. Since the Amazon region shows little change in latent heat flux between ShCu and Deep days (TIAN *et al.*, 2021; ZHUANG *et al.*, 2017), moisture advection is responsible for the slow water vapor convergence, since early morning, reported by ADAMS *et al.* (2013). Other environmental conditions still play a role to promote the strong convergence associated with the STD convection transition.

We explored vertical wind shear experiments to investigate its role in the STD transition. The low-level jet greatly impacts high-cloud development. The late afternoon convection is enhanced for a wider jet of moderate strength peaking at a relatively higher position (from ∼ 2 to 4 km). The jet structure also affects the time and intensity of the precipitation peaks, emphasizing the low-level shear importance to convection. In addition to the low-level wind, the upper-level jet also contributes to modulating the STD transition, but it is role is minor and mainly related to the peak time. Interestingly, all the experiments were associated with a later peak in the STD transition, although the stronger upper-level jet provided a greater reduction in ice content around 16 LST. While vertical wind shear impacts convection, our findings suggest that wind shear is not a necessary condition for the STD transition, as it may occur even in its absence. This particular result was also observed by KHAIROUTDINOV; RANDALL (2006).

Furthermore, our modeling results provide more quantitative information than previous observational studies on the vertical wind shear role for convection in the Amazon. For example, ZHUANG *et al.* (2017) showed that ShCu days are associated with stronger deep-layer shear during the wet season. Although we show that strong upper-level shear negatively affects ice content, it does not impede the STD convection transition. TIAN *et al.* (2021) suggested that the mid-troposphere vertical wind shear could significantly limit the vertical development of convection. We observed that the ice content is only moderately reduced during the afternoon when the upper-level jet either increases its amplitude and width, or the peak position shifts from 12 to 8 km. While CHAKRABORTY *et al.* (2018) indicated that a more intense low-level shear is associated with shallow convection during the transition season, we suggest that a stronger low-level shear would only shift the STD convection transition to a later time instead of preventing it.

## 6.6 Preliminary Conclusions

We employed the SAM model coupled with a Surface Land Model (SLM) to perform simulations for the Amazon region in December 2014. The model was forced with the large-scale fields from the variational analysis, and the observations from the GoAmazon2014/5 experiment were used to validate the model results. The SLM default input parameters were modified according to in-situ and satellite observations over the Amazon region, and fine-tuning tests focused on improving the model agreement with the observations. The simulations consistently reproduced the observations for precipitation, column water vapor, surface latent and sensible heat fluxes, and surface radiation fluxes. Sensitivity tests showed that simulations conducted using a single-moment microphysics scheme drifted towards a drier state, while simulations with the P3 microphysics scheme more closely reproduced the observed water budget. For a more detailed validation of the SLM, having more comprehensive observations of the soil properties (e.g. temperature and wetness down to 4 m) would be necessary.

We conducted sensitivity experiments to study the STD transition, focusing on the role of moisture and vertical wind shear in both low-level and higher levels. The low-level preconditioning appeared to have the greatest impact on convection. As humidity is reduced at low levels in simulations of Deep scenarios, the ice content drops to negligible values under conditions closely associated with ShCU scenarios. Thus, low-level preconditioning is a necessary condition for deep convection. The second most important factor was the large-scale vertical advection, which affects the diurnal low-level moisture condition as well, thus also impacting convection. Conversely, the free troposphere preconditioning plays a minor role in convection and only weakly influences the development of deep cloud anvils and precipitation.

Vertical wind shear does affect the STD transition, but it is not a trigger. The low-level jet significantly impacts the ice water content, which is favored especially in the afternoon for a broader jet of moderate strength peaking from 2 to 4 km. When the low-level jet is removed, ice water shows a modest decrease during the day, but deep convection still occurs over smaller areas. The upper-level jet negatively affects the ice content, although its impact is more minor than that observed for the low-level jet.

While our results provide quantitative information on the role of moisture and wind shear in convection, we also recommend that sensitivity experiments should be conducted using different cloud-resolving models. For instance, SAM uses periodic lateral conditions, which artificially impact the numerical results. Using multiple models can aid in evaluating the robustness of the findings and identifying potential biases in the models. Finally, we suggest that future studies conduct more idealized experiments to quantitatively evaluate the role of water vapor convergence and the impact of the large-scale wind direction on convection, as we focus only on the wind speed to idealize the jet experiments.

# 7 CONCLUSIONS AND FUTURE DIRECTIONS

In order to evaluate the potential controlling mechanisms of isolated convection during the wet season (December-April) in the central Amazon, we analyzed measurements collected during the GoAmazon2014/5 field campaign. Furthermore, we conducted high-resolution numerical simulations to assess the sensitivity of the STD transition to these mechanisms, specifically focusing on the month of December 2014.

From the analysis of the GoAmazon observations, we noted an excess of water vapor since early morning in the lower levels, particularly below 3 km, on days characterized by deep convection. Moreover, the mornings of Cong and ShCu days presented significant water vapor divergence, while on Deep days, there was a weak convergence. Consequently, the Deep regime exhibited higher column water vapor (CWV) in the mid-troposphere in the afternoon. The numerical simulations demonstrated a pronounced sensitivity of the STD transition to low-level preconditioning. Specifically, as the humidity was decreased in the simulations of Deep scenarios, the ice content decreased significantly, reaching negligible values resembling those observed in ShCu scenarios. On the other hand, the preconditioning of the free troposphere had a limited impact on convection and only weakly influenced the formation of deep cloud anvils and precipitation. Therefore, these findings indicate that only preconditioning in the low levels plays a crucial role in the development of convection in the Amazon.

During the afternoon of Deep days, we observed a strong convergence of water vapor associated with the late afternoon STD transition, while ShCu and Cong days showed almost no convergence. The simulations further highlighted the notable sensitivity to large-scale vertical advection, which is closely tied to water vapor convergence. Hence, both observational and modeling studies indicate a robust correlation between convergence and convection.

Based on the conditionally averaged precipitation analysis, we found a strong correlation between the observed afternoon precipitation (14 to 20 LST) on local convective days and the water vapor content in the low and mid-troposphere, both in the early morning (08 LST) and the afternoon (14 LST). However, days without precipitation also exhibited a relatively similar range of CWV values. This suggests that while moisture is a necessary condition, it is not sufficient on its own to trigger the STD transition. Additionally, we found that precipitation also displays a modest association with vertical wind shear. Specifically, precipitation tends to increase in the presence of stronger low-level shear and weaker deep-layer shear intensity. However, this relationship is relatively weaker compared to the correlation observed with CWV.

The numerical simulations revealed that vertical wind shear plays a significant role in the STD transition, but is not a trigger. The low-level jet had a notable impact on the ice water content, particularly during the afternoon. Convection was enhanced when the jet was relatively broader and of moderate strength, peaking at a higher position (from 2 to 4 km). However, when the low-level jet was removed from the simulations, there was only a modest decrease in ice water throughout the day and deep convection still occurred, albeit over smaller areas. The upper-level jet had a negative impact on the ice content, although its influence was relatively minor compared to the low-level jet. Both observational and modeling results indicate that vertical wind shear has a relatively smaller role in convection compared to moisture and moisture advection. However, the low-level shear still contributes significantly to the development of high clouds and the overall amount of precipitation.

Our observational analysis of the water budget encountered significant limitations in terms of time coverage, as the radiosonde was launched only every 6 hours. Furthermore, consistent observations of liquid and ice water during deep precipitating events were lacking. In addition, the sensitivity experiments conducted to assess the role of moisture advection yielded only indirect information regarding the impact of moisture convergence on the STD transition. Therefore, further observational and idealized numerical simulation studies are required to comprehensively investigate the relative contribution of moisture convergence in convective development and help to provide insights into whether convergence acts as a cause or an effect of the STD transition. The influence of the large-scale wind direction was not addressed in our numerical simulations, and future studies are also necessary to further evaluate this aspect.

Although our findings demonstrate statistical robustness, both the observational and modeling studies conducted in this project are limited in terms of time coverage. The observational study spanned ten months (from December to April 2014-2015), and the modeling study covered one month (December 2014). In the future, when multi-year observations become available, for instance, from the Amazon Tall Tower Observatory (ANDREAE *et al.*, 2015), it will be crucial to reproduce not only this study but also other literature studies. A broader temporal perspective is particularly important in the context of climate change, as it has the potential to significantly alter cloud convective processes. As climate conditions evolve, it becomes essential to reevaluate these observational datasets to identify potential shifts or trends in convective behavior.

For the modeling study, it is also important to conduct similar investigations using different cloud-resolving models. Utilizing multiple models can help assess the robustness of the findings and identify potential model biases. This will contribute to strengthening the confidence in the findings. Finally, while this study purposely focused on specific aspects of convection and excluded the examination of mesoscale convective systems and aerosol effects, these research areas pose open questions that need to be addressed. Investigating the dynamics and behavior of mesoscale convective systems, as well as understanding the impact of aerosols on convection, are also important for enhancing our knowledge of tropical convection and improving weather and climate models.

# 8 DATA AVAILABILITY

The GoAmazon2014/5 observations are publicly available at https://www.arm.gov/research/campaigns/amf2014goamazon. The large-scale forcing data based on the variational analysis for the GoAmazon2014/5 experiment is available at the ARM Archive: http://iop.archive.arm.gov/arm-iop/0eval-data/xie/scm-forcing/iop_at_mao/. The Moderate Resolution Imaging Spectroradiometer (MODIS) data for land cover and leaf area index can be downloaded through the Application for Extracting and Exploring Analysis Ready Samples ($A\rho\rho$EEARS, https://appeears.earthdatacloud.nasa.gov/). The Global Land Data Assimilation System (GLDAS) data for soil temperature and soil wetness are available at https://disc.gsfc.nasa.gov/datasets/GLDAS_NOAH025_3H_2.1/summary. Topography and bathymetry data are provided by NOAA National Centers for Environmental Information (2022).

# REFERENCES

ADAMS, D. K.; BARBOSA, H. M. J.; RíOS, K. P. G. D. L. A spatiotemporal water vapor–deep convection correlation metric derived from the amazon dense gnss meteorological network. **Monthly Weather Review**, American Meteorological Society, Boston MA, USA, v. 145, n. 1, p. 279 – 288, 2017. Available at: https://journals.ametsoc.org/view/journals/mwre/145/1/mwr-d-16-0140.1.xml.

ADAMS, D. K. *et al.* The amazon dense GNSS meteorological network: A new approach for examining water vapor and deep convection interactions in the tropics. **Bulletin of the American Meteorological Society**, American Meteorological Society, v. 96, n. 12, p. 2151–2165, dec 2015.

ADAMS, D. K. *et al.* A dense GNSS meteorological network for observing deep convection in the amazon. **Atmospheric Science Letters**, Wiley, v. 12, n. 2, p. 207–212, jan 2011.

ADAMS, D. K. *et al.* GNSS observations of deep convective time scales in the amazon. **Geophysical Research Letters**, American Geophysical Union (AGU), v. 40, n. 11, p. 2818–2823, jun 2013.

AMS/APCA Second Joint Conference on Applications of Air Pollution Meteorology, March 24–27, 1980, New Orleans, La. **Bulletin of the American Meteorological Society**, American Meteorological Society, v. 61, n. 1, p. 65–98, 1980. ISSN 00030007, 15200477. Available at: http://www.jstor.org/stable/26220687.

ANDREAE, M. O. *et al.* The amazon tall tower observatory (ATTO): overview of pilot measurements on ecosystem ecology, meteorology, trace gases, and aerosols. **Atmospheric Chemistry and Physics**, Copernicus GmbH, v. 15, n. 18, p. 10723–10776, sep 2015.

ARAGÃO, L. E. O. C. *et al.* Environmental change and the carbon balance of amazonian forests. **Biological Reviews**, Wiley, v. 89, n. 4, p. 913–931, fev. 2014. Available at: https://doi.org/10.1111/brv.12088.

ARAKAWA, A. The cumulus parameterization problem: Past, present, and future. **Journal of Climate**, American Meteorological Society, v. 17, n. 13, p. 2493–2525, jul 2004.

ARM, Atmospheric Radiation Measurement. **Data Quality Assessment for ARM Radiation Data (QCRAD1LONG). 2013-12-20 to 2015-12-01, ARM Mobile Facility (MAO) Manacapuru, Amazonas, Brazil; AMF1 (M1)**. Compiled by D. Zhang, Atmospheric Radiation Measurement (ARM) Archive, Oak Ridge, Tennessee, USA, 2013. Available at: http://dx.doi.org/10.5439/1227214.

ARM, Atmospheric Radiation Measurement. **Meteorological Measurements associated with the Aerosol Observing System (AOSMET). 2013-12-12 to 2015-12-01, ARM Mobile Facility (MAO) Manacapuru, Amazonas, Brazil; MAOS (S1)**. Compiled by J. Kyrouac, S. Springston and M. Tuftedal, Atmospheric

Radiation Measurement (ARM) Archive, Oak Ridge, Tennessee, USA, 2013. Available at: http://dx.doi.org/10.5439/1984920.

ARM, Atmospheric Radiation Measurement. **ARM Best Estimate Data Products (ARMBEATM). 2014-01-01 to 2015-12-31, ARM Mobile Facility (MAO) Manacapuru, Amazonas, Brazil; AMF1 (M1)**. Compiled by C. Xiao and X. Shaocheng, Atmospheric Radiation Measurement (ARM) Archive, Oak Ridge, Tennessee, USA, 2014. Available at: http://dx.doi.org/10.5439/1333748.

ARM, Atmospheric Radiation Measurement. **ARM Best Estimate Data Products (ARMBECLDRAD). 2014-01-01 to 2015-12-01, ARM Mobile Facility (MAO) Manacapuru, Amazonas, Brazil; AMF1 (M1)**. Compiled by C. Xiao and X. Shaocheng, Atmospheric Radiation Measurement (ARM) Archive, Oak Ridge, Tennessee, USA, 2014. Available at: http://dx.doi.org/10.5439/1333228.

ARM, Atmospheric Radiation Measurement. **Balloon-Borne Sounding System (SONDEWNPN). 2014-01-01 to 2015-12-01, ARM Mobile Facility (MAO) Manacapuru, Amazonas, Brazil; AMF1 (M1)**. Compiled by: Keeler, E., and Burk, K., Atmospheric Radiation Measurement (ARM) Archive, Oak Ridge, Tennessee, USA, 2014. Available at: https://doi.org/10.5439/1595321.

ARM, Atmospheric Radiation Measurement. **Ceilometer (CEIL). 2014-01-01 to 2015-12-01, ARM Mobile Facility (MAO) Manacapuru, Amazonas, Brazil; AMF1 (M1)**. Compiled by V. Morris, D. Zhang and B. Ermold, Atmospheric Radiation Measurement (ARM) Archive, Oak Ridge, Tennessee, USA, 2014. Available at: http://dx.doi.org/10.5439/1181954.

ARM, Atmospheric Radiation Measurement. **Eddy Correlation Flux Measurement System (30ECOR). 2014-04-03 to 2015-12-01, ARM Mobile Facility (MAO) Manacapuru, Amazonas, Brazil; AMF1 (M1)**. Compiled by R. Sullivan, D. Billesbach, E. Keeler and B. Ermold, Atmospheric Radiation Measurement (ARM) Archive, Oak Ridge, Tennessee, USA, 2014. Available at: http://dx.doi.org/10.5439/1025039.

ARM, Atmospheric Radiation Measurement. **Micropulse Lidar (MPLPOLFS). 2014-01-03 to 2015-12-01, ARM Mobile Facility (MAO) Manacapuru, Amazonas, Brazil; AMF1 (M1)**. Compiled by P. Muradyan, E. Cromwell, A. Koontz and R. Coulter, Atmospheric Radiation Measurement (ARM) Archive, Oak Ridge, Tennessee, USA, 2014. Available at: http://dx.doi.org/10.5439/1320657.

ARM, Atmospheric Radiation Measurement. **Planetary Boundary Layer Height (PBLHTSONDE1MCFARL). 2014-01-01 to 2015-12-01, ARM Mobile Facility (MAO) Manacapuru, Amazonas, Brazil; AMF1 (M1)**. Compiled by L. Riihimaki and D. Zhang, Atmospheric Radiation Measurement (ARM) Archive, Oak Ridge, Tennessee, USA, 2014. Available at: http://dx.doi.org/10.5439/1150253.

ARM, Atmospheric Radiation Measurement. **Quality Controlled Eddy Correlation Flux Measurement (30QCECOR). 2014-04-03 to 2015-12-01, ARM Mobile Facility (MAO) Manacapuru, Amazonas, Brazil; AMF1 (M1)**. Compiled by S. Xie, Atmospheric Radiation Measurement (ARM) Archive, Oak Ridge, Tennessee, USA, 2014. Available at: http://dx.doi.org/10.5439/1097546.

ARM, Atmospheric Radiation Measurement. **Radar Wind Profiler (1290RW-PWINDCON). 2014-02-14 to 2015-12-01, ARM Mobile Facility (MAO) Manacapuru, Amazonas, Brazil; AMF1 (M1)**. Compiled by R. Coulter, P. Muradyan and T. Martin, Atmospheric Radiation Measurement (ARM) Archive, Oak Ridge, Tennessee, USA, 2014. Available at: http://dx.doi.org/10.5439/1025031.

ARM, Atmospheric Radiation Measurement. **Surface Meteorological Instrumentation (MET). 2014-01-01 to 2015-12-01, ARM Mobile Facility (MAO) Manacapuru, Amazonas, Brazil; AMF1 (M1)**. Compiled by J. Kyrouac and Y. Shi, Atmospheric Radiation Measurement (ARM) Archive, Oak Ridge, Tennessee, USA, 2014. Available at: http://dx.doi.org/10.5439/1786358.

ARM, Atmospheric Radiation Measurement. **W-Band (95 GHz) ARM Cloud Radar (WACR). 2014-02-18 to 2015-12-02, ARM Mobile Facility (MAO) Manacapuru, Amazonas, Brazil; AMF1 (M1)**. Compiled by N. Bharadwaj, I. Lindenmaier, K. Johnson, D. Nelson, B. Isom, J. Hardin and A. Matthews, Atmospheric Radiation Measurement (ARM) Archive, Oak Ridge, Tennessee, USA, 2014. Available at: http://dx.doi.org/10.5439/1973060.

ARRAUT, J. M. *et al.* Aerial rivers and lakes: Looking at large-scale moisture transport and its relation to amazonia and to subtropical rainfall in south america. **Journal of Climate**, American Meteorological Society, v. 25, n. 2, p. 543–556, jan 2012.

ARTAXO, P. *et al.* Atmospheric aerosols in amazonia and land use change: from natural biogenic to biomass burning conditions. **Faraday Discuss.**, Royal Society of Chemistry (RSC), v. 165, p. 203–235, 2013.

BECHTOLD, P. *et al.* The simulation of the diurnal cycle of convective precipitation over land in a global model. **Quarterly Journal of the Royal Meteorological Society**, v. 130, n. 604, p. 3119–3137, 2004. Available at: https://rmets.onlinelibrary.wiley.com/doi/abs/10.1256/qj.03.103.

BETTS, A. K. Evaluation of the diurnal cycle of precipitation, surface thermodynamics, and surface fluxes in the ECMWF model using LBA data. **Journal of Geophysical Research**, American Geophysical Union (AGU), v. 107, n. D20, 2002.

BETTS, A. K. *et al.* The amazonian boundary layer and mesoscale circulations. *In*: **Amazonia and Global Change**. American Geophysical Union, 2009. p. 163–181. Available at: https://doi.org/10.1029/2008gm000725.

BETTS, A. K.; JAKOB, C. Study of diurnal cycle of convective precipitation over amazonia using a single column model. **Journal of Geophysical Research: Atmospheres**, American Geophysical Union (AGU), v. 107, n. D23, p. ACL 25–1–ACL 25–13, dez. 2002. Available at: https://doi.org/10.1029/2002jd002264.

BLOSSEY, P. N. *et al.* Cloud-resolving model simulations of KWAJEX: Model sensitivities and comparisons with satellite and radar observations. **J. Atmos. Sci.**, American Meteorological Society, v. 64, n. 5, p. 1488–1508, maio 2007.

BLOSSEY, P. N.; BRETHERTON, C. S.; MOHRMANN, J. Simulating observed cloud transitions in the northeast pacific during CSET. **Monthly Weather Review**, American Meteorological Society, maio 2021. Available at: https://doi.org/10.1175/mwr-d-20-0328.1.

BRETHERTON, C. S.; PETERS, M. E.; BACK, L. E. Relationships between water vapor path and precipitation over the tropical oceans. **Journal of Climate**, American Meteorological Society, v. 17, n. 7, p. 1517–1528, abr. 2004. Available at: https://doi.org/10.1175/1520-0442(2004)017<1517:rbwvpa>2.0.co;2.

BRETHERTON, C. S.; SMOLARKIEWICZ, P. K. Gravity waves, compensating subsidence and detrainment around cumulus clouds. **Journal of the Atmospheric Sciences**, American Meteorological Society, v. 46, n. 6, p. 740–759, mar. 1989. Available at: https://doi.org/10.1175/1520-0469(1989)046<0740:gwcsad>2.0.co;2.

CARVALHO, L. M. V. *et al.* The south american monsoon system and the 1970s climate transition. **International Journal of Climatology**, Wiley, v. 31, n. 8, p. 1248–1256, abr. 2010. Available at: https://doi.org/10.1002/joc.2147.

CHAKRABORTY, S. *et al.* On the role of aerosols, humidity, and vertical wind shear in the transition of shallow-to-deep convection at the green ocean amazon 2014/5 site. **Atmospheric Chemistry and Physics**, Copernicus GmbH, v. 18, n. 15, p. 11135–11148, aug 2018.

COLLIER, J. C.; BOWMAN, K. P. Diurnal cycle of tropical precipitation in a general circulation model. **Journal of Geophysical Research**, American Geophysical Union (AGU), v. 109, n. D17, 2004. Available at: https://doi.org/10.1029/2004jd004818.

COLLINS, W. D. *et al.* The formulation and atmospheric simulation of the community atmosphere model version 3 (CAM3). **Journal of Climate**, American Meteorological Society, v. 19, n. 11, p. 2144–2161, jun. 2006. Available at: https://doi.org/10.1175/jcli3760.1.

COTTON, W. R.; BRYAN, G. H.; HEEVER, S. C. Van den. **Storm and cloud dynamics: the dynamics of clouds and precipitating mesoscale systems**. 2. ed. ed. Amsterdam Heidelberg: Academic Press, 2011. (International geophysics series, 99). ISBN 9780120885428.

DAI, A.; TRENBERTH, K. E. The diurnal cycle and its depiction in the community climate system model. **Journal of Climate**, American Meteorological Society, v. 17, n. 5, p. 930–951, mar. 2004.

DEE, D. *et al.* Ecmwf reanalyses: Diagnosis and application. 2009. Available at: https://www.ecmwf.int/node/15237.

DEE, D. P. *et al.* The ERA-interim reanalysis: configuration and performance of the data assimilation system. **Quarterly Journal of the Royal Meteorological Society**, Wiley, v. 137, n. 656, p. 553–597, abr. 2011. Available at: https://doi.org/10.1002/qj.828.

DEFRIES, R. S. *et al.* Fire-related carbon emissions from land use transitions in southern amazonia. **Geophys. Res. Lett.**, American Geophysical Union (AGU), v. 35, n. 22, nov. 2008.

EISSNER, J. M. *et al.* Factors governing cloud growth and entrainment rates in shallow cumulus and cumulus congestus during GoAmazon2014/5. **Journal of Geophysical Research: Atmospheres**, American Geophysical Union (AGU), v. 126, n. 12, jun. 2021. Available at: https://doi.org/10.1029/2021jd034722.

FENG, Z.; GIANGRANDE, S. **Merged RWP-WACR-ARSCL Cloud Mask and Cloud Type**. Atmospheric Radiation Measurement (ARM) Archive, Oak Ridge National Laboratory (ORNL), Oak Ridge, TN (US), 2018. Artwork Size: 1 GB Pages: 1 GB Type: dataset. Available at: https://www.osti.gov/servlets/purl/1462693/.

FIGUEROA, S.; NOBRE, C. Precipitation distribution over central and western tropical south america. **Climanálise**, v. 5, p. 36–45, 01 1990.

FITZJARRALD, D. R. *et al.* Spatial and temporal rainfall variability near the Amazon-Tapajós confluence. **J. Geophys. Res.**, American Geophysical Union (AGU), v. 113, n. G1, mar. 2008.

FREITAS, S. R. *et al.* Cascading toward a kilometer-scale GCM: Impacts of a scale-aware convection parameterization in the goddard earth observing system GCM. **Geophysical Research Letters**, American Geophysical Union (AGU), v. 47, n. 17, set. 2020. Available at: https://doi.org/10.1029/2020gl087682.

FRIEDL, M. A. *et al.* Modis collection 5 global land cover: Algorithm refinements and characterization of new datasets. **Remote Sensing of Environment**, v. 114, n. 1, p. 168–182, 2010. ISSN 0034-4257. Available at: https://www.sciencedirect.com/science/article/pii/S0034425709002673.

GENTINE, P. *et al.* Role of surface heat fluxes underneath cold pools. **Geophysical Research Letters**, American Geophysical Union (AGU), v. 43, n. 2, p. 874–883, jan 2016.

GHATE, V. P.; KOLLIAS, P. On the controls of daytime precipitation in the amazonian dry season. **Journal of Hydrometeorology**, American Meteorological Society, v. 17, n. 12, p. 3079–3097, dec 2016.

GIANGRANDE, S. E. *et al.* Cloud characteristics, thermodynamic controls and radiative impacts during the observations and modeling of the green ocean amazon (GoAmazon2014/5) experiment. **Atmospheric Chemistry and Physics**, Copernicus GmbH, v. 17, n. 23, p. 14519–14541, dec 2017.

GLOOR, M. *et al.* Intensification of the amazon hydrological cycle over the last two decades. **Geophys. Res. Lett.**, American Geophysical Union (AGU), v. 40, n. 9, p. 1729–1733, maio 2013.

GONÇALVES, L. J. M. *et al.* Interaction between cloud–radiation, atmospheric dynamics and thermodynamics based on observational data from GoAmazon 2014/15 and a cloud-resolving model. **Atmos. Chem. Phys.**, Copernicus GmbH, v. 22, n. 23, p. 15509–15526, dez. 2022.

GONÇALVES, W. A.; MACHADO, L. A. T.; KIRSTETTER, P.-E. Influence of biomass aerosol on precipitation over the central amazon: an observational study. **Atmos. Chem. Phys.**, Copernicus GmbH, v. 15, n. 12, p. 6789–6800, jun. 2015.

GRABOWSKI, W. W. *et al.* Daytime convective development over land: A model intercomparison based on LBA observations. **Quarterly Journal of the Royal Meteorological Society**, Wiley, v. 132, n. 615, p. 317–344, jan 2006.

HECKENBERGER, M. J. *et al.* The legacy of cultural landscapes in the brazilian amazon: implications for biodiversity. **Philosophical Transactions of the Royal Society B: Biological Sciences**, The Royal Society, v. 362, n. 1478, p. 197–208, jan. 2007. Available at: https://doi.org/10.1098/rstb.2006.1979.

HENDERSON, P. W.; PINCUS, R. Multiyear evaluations of a cloud model using ARM data. **J. Atmos. Sci.**, American Meteorological Society, v. 66, n. 9, p. 2925–2936, set. 2009.

HENKES, A. *et al.* Morning boundary layer conditions for shallow to deep convective cloud evolution during the dry season in the central amazon. **Atmospheric Chemistry and Physics**, Copernicus GmbH, v. 21, n. 17, p. 13207–13225, set. 2021. Available at: https://doi.org/10.5194/acp-21-13207-2021.

HERDIES, D. L. Moisture budget of the bimodal pattern of the summer circulation over south america. **Journal of Geophysical Research**, American Geophysical Union (AGU), v. 107, n. D20, 2002. Available at: https://doi.org/10.1029/2001jd000997.

HOHENEGGER, C.; STEVENS, B. Preconditioning deep convection with cumulus congestus. **Journal of the Atmospheric Sciences**, American Meteorological Society, v. 70, n. 2, p. 448–464, feb 2013.

HOLLOWAY, C. E.; NEELIN, J. D. Moisture vertical structure, column water vapor, and tropical deep convection. **Journal of the Atmospheric Sciences**, American Meteorological Society, v. 66, n. 6, p. 1665–1683, jun. 2009. Available at: https://doi.org/10.1175/2008jas2806.1.

HOUZE Jr., R. A. Mesoscale convective systems. **Reviews of Geophysics**, v. 42, n. 4, 2004. Available at: https://agupubs.onlinelibrary.wiley.com/doi/abs/10.1029/2004RG000150.

HOUZE Jr., R. A. **Cloud Dynamics**. [*S.l.: s.n.*]: Academic Press, 2014. ISBN 978-0-12-374266-7.

HUBBELL, S. P. *et al.* How many tree species are there in the amazon and how many of them will go extinct? **Proceedings of the National Academy of Sciences**, Proceedings of the National Academy of Sciences, v. 105, n. Supplement 1, p. 11498–11504, ago. 2008. Available at: https://doi.org/10.1073/pnas.0801915105.

ITTERLY, K. F.; TAYLOR, P. C.; DODSON, J. B. Sensitivity of the amazonian convective diurnal cycle to its environment in observations and reanalysis. **Journal of Geophysical Research: Atmospheres**, American Geophysical Union (AGU), v. 123, n. 22, nov. 2018. Available at: https://doi.org/10.1029/2018jd029251.

JOHNSON, R. H. *et al.* Trimodal characteristics of tropical convection. **Journal of Climate**, American Meteorological Society, v. 12, n. 8, p. 2397–2418, ago. 1999. Available at: https://doi.org/10.1175/1520-0442(1999)012<2397:tcotc>2.0.co;2.

KELLER, M. *et al.* ECOLOGICAL RESEARCH IN THE LARGE-SCALE BIOSPHERE– ATMOSPHERE EXPERIMENT IN AMAZONIA: EARLY RESULTS. **Ecological Applications**, Wiley, v. 14, n. sp4, p. 3–16, ago. 2004. Available at: https://doi.org/10.1890/03-6003.

KERR, R. A. A north atlantic climate pacemaker for the centuries. **Science**, American Association for the Advancement of Science (AAAS), v. 288, n. 5473, p. 1984–1985, jun. 2000. Available at: https://doi.org/10.1126/science.288.5473.1984.

KHAIROUTDINOV, M.; RANDALL, D. High-resolution simulation of shallow-to-deep convection transition over land. **Journal of the Atmospheric Sciences**, American Meteorological Society, v. 63, n. 12, p. 3421–3436, dec 2006.

KHAIROUTDINOV, M. F. *et al.* Large-eddy simulation of maritime deep tropical convection. **Journal of Advances in Modeling Earth Systems**, American Geophysical Union (AGU), v. 2, dez. 2009. Available at: https://doi.org/10.3894/james.2009.1.15.

KHAIROUTDINOV, M. F.; RANDALL, D. A. Cloud resolving modeling of the ARM summer 1997 IOP: Model formulation, results, uncertainties, and sensitivities. **Journal of the Atmospheric Sciences**, American Meteorological Society, v. 60, n. 4, p. 607–625, feb 2003.

KNIGHT, J. R.; FOLLAND, C. K.; SCAIFE, A. A. Climate impacts of the atlantic multidecadal oscillation. **Geophysical Research Letters**, American Geophysical Union (AGU), v. 33, n. 17, 2006. Available at: https://doi.org/10.1029/2006gl026242.

KOCH, D.; GENIO, A. D. D. Black carbon semi-direct effects on cloud cover: review and synthesis. **Atmos. Chem. Phys.**, Copernicus GmbH, v. 10, n. 16, p. 7685–7696, ago. 2010.

KOREN, I. *et al.* Measurement of the effect of amazon smoke on inhibition of cloud formation. **Science**, American Association for the Advancement of Science (AAAS), v. 303, n. 5662, p. 1342–1345, fev. 2004.

KOREN, I. *et al.* Smoke invigoration versus inhibition of clouds over the amazon. **Science**, American Association for the Advancement of Science (AAAS), v. 321, n. 5891, p. 946–949, ago. 2008.

KRISHNAMURTI, T. N.; STEFANOVA, L.; MISRA, V. **Tropical Meteorology**. 2013. ed. New York, NY: Springer, 2013. (Springer Atmospheric Sciences).

LAURANCE, W. F. ENVIRONMENT: The future of the brazilian amazon. **Science**, American Association for the Advancement of Science (AAAS), v. 291, n. 5503, p. 438–439, jan. 2001. Available at: https://doi.org/10.1126/science.291.5503.438.

LAURENT, H. Characteristics of the amazonian mesoscale convective systems observed from satellite and radar during the WETAMC/LBA experiment. **Journal of Geophysical Research**, American Geophysical Union (AGU), v. 107, n. D20, 2002. Available at: https://doi.org/10.1029/2001jd000337.

LEBLANC, T. *et al.* Measurements of humidity in the atmosphere and validation experiments (MOHAVE)-2009: overview of campaign operations and results. **Atmospheric Measurement Techniques**, Copernicus GmbH, v. 4, n. 12, p. 2579–2605, dez. 2011. Available at: https://doi.org/10.5194/amt-4-2579-2011.

LEBO, Z. J.; MORRISON, H. Effects of horizontal and vertical grid spacing on mixing in simulated squall lines and implications for convective strength and structure. **Monthly Weather Review**, American Meteorological Society, Boston MA, USA, v. 143, n. 11, p. 4355 – 4375, 2015. Available at: https://journals.ametsoc.org/view/journals/mwre/143/11/mwr-d-15-0154.1.xml.

LEE, J. M.; KHAIROUTDINOV, M. A simplified land model (SLM) for use in cloud-resolving models: Formulation and evaluation. **Journal of Advances in Modeling Earth Systems**, American Geophysical Union (AGU), v. 7, n. 3, p. 1368–1392, set. 2015. Available at: https://doi.org/10.1002/2014ms000419.

LEWINSOHN, T.; PRADO, P. I. **BIODIVERSIDADE BRASILEIRA : sintese do estado atual do conhecimento**. São Paulo: EDITORA CONTEXTO, 2002. ISBN 8572442308.

LIN, X.; RANDALL, D. A.; FOWLER, L. D. Diurnal variability of the hydrologic cycle and radiative fluxes: Comparisons between observations and a GCM. **Journal of Climate**, American Meteorological Society, v. 13, n. 23, p. 4159–4179, dez. 2000.

LIU, L. *et al.* Impact of biomass burning aerosols on radiation, clouds, and precipitation over the amazon: relative importance of aerosol–cloud and aerosol–radiation interactions. **Atmospheric Chemistry and Physics**, v. 20, n. 21, p. 13283–13301, 2020. Available at: https://acp.copernicus.org/articles/20/13283/2020/.

LIU, S.; LIANG, X.-Z. Observed diurnal cycle climatology of planetary boundary layer height. **J. Clim.**, American Meteorological Society, v. 23, n. 21, p. 5790–5809, nov. 2010.

LIU, Z.; MUHLBAUER, A.; ACKERMAN, T. Evaluation of high-level clouds in cloud resolving model simulations with ARM and KWAJEX observations. **J. Adv. Model. Earth Syst.**, American Geophysical Union (AGU), v. 7, n. 4, p. 1716–1740, dez. 2015.

MACHADO, L. A. T. Diurnal march of the convection observed during TRMM-WETAMC/LBA. **Journal of Geophysical Research**, American Geophysical Union (AGU), v. 107, n. D20, 2002.

MACHADO, L. A. T. *et al.* Seasonal and diurnal variability of convection over the amazonia: A comparison of different vegetation types and large scale forcing. **Theoretical and Applied Climatology**, Springer Science and Business Media LLC, v. 78, n. 1-3, apr 2004.

MADDEN, R. A.; JULIAN, P. R. Observations of the 40–50-day tropical oscillation—a review. **Monthly Weather Review**, American Meteorological Society, v. 122, n. 5, p. 814–837, maio 1994. Available at: https://doi.org/10.1175/1520-0493(1994)122<0814:ootdto>2.0.co;2.

MAHER, P. *et al.* The impact of parameterized convection on climatological precipitation in atmospheric global climate models. **Geophysical Research Letters**, American Geophysical Union (AGU), v. 45, n. 8, p. 3728–3736, abr. 2018. Available at: https://doi.org/10.1002/2017gl076826.

MALHI, Y. *et al.* The regional variation of aboveground live biomass in old-growth amazonian forests. **Global Change Biology**, Wiley, v. 12, n. 7, p. 1107–1138, maio 2006. Available at: https://doi.org/10.1111/j.1365-2486.2006.01120.x.

MAPES, B.; MILLIFF, R.; MORZEL, J. Composite life cycle of maritime tropical mesoscale convective systems in scatterometer and microwave satellite observations. **Journal of the Atmospheric Sciences**, American Meteorological Society, v. 66, n. 1, p. 199–208, jan. 2009. Available at: https://doi.org/10.1175/2008jas2746.1.

MAPES, B.; NEALE, R. Parameterizing convective organization to escape the entrainment dilemma. **Journal of Advances in Modeling Earth Systems**, v. 3, n. 2, 2011. Available at: https://agupubs.onlinelibrary.wiley.com/doi/abs/10.1029/2011MS000042.

MAPES, B. *et al.* The mesoscale convection life cycle: Building block or prototype for large-scale tropical waves? **Dynamics of Atmospheres and Oceans**, Elsevier BV, v. 42, n. 1-4, p. 3–29, dez. 2006. Available at: https://doi.org/10.1016/j.dynatmoce.2006.03.003.

MARENGO, J. A. *et al.* Two contrasting severe seasonal extremes in tropical south america in 2012: Flood in amazonia and drought in northeast brazil. **Journal of Climate**, American Meteorological Society, v. 26, n. 22, p. 9137–9154, nov. 2013. Available at: https://doi.org/10.1175/jcli-d-12-00642.1.

MARENGO, J. A. *et al.* Hydro-climate and ecological behaviour of the drought of amazonia in 2005. **Philos. Trans. R. Soc. Lond. B Biol. Sci.**, The Royal Society, v. 363, n. 1498, p. 1773–1778, maio 2008.

MARENGO, J. A. *et al.* The drought of 2010 in the context of historical droughts in the amazon region. **Geophys. Res. Lett.**, American Geophysical Union (AGU), v. 38, n. 12, jun. 2011.

MARTIN, S. T. *et al.* The green ocean amazon experiment (GoAmazon2014/5) observes pollution affecting gases, aerosols, clouds, and rainfall over the rain forest. **Bulletin of the American Meteorological Society**, American Meteorological Society, v. 98, n. 5, p. 981–997, maio 2017. Available at: https://doi.org/10.1175/bams-d-15-00221.1.

MARTIN, S. T. *et al.* Introduction: Observations and modeling of the green ocean amazon (GoAmazon2014/5). **Atmospheric Chemistry and Physics**, Copernicus GmbH, v. 16, n. 8, p. 4785–4797, apr 2016.

MATTIOLI, V. *et al.* Analysis of radiosonde and ground-based remotely sensed PWV data from the 2004 north slope of alaska arctic winter radiometric experiment. **Journal of Atmospheric and Oceanic Technology**, American Meteorological Society, v. 24, n. 3, p. 415–431, mar. 2007. Available at: https://doi.org/10.1175/jtech1982.1.

MAYORGA, E. *et al.* **LBA-ECO CD-06 Amazon River Basin Land and Stream Drainage Direction Maps**. ORNL Distributed Active Archive Center, 2012. Available at: http://daac.ornl.gov/cgi-bin/dsviewer.pl?ds_id=1086.

MLAWER, E. J. *et al.* Radiative transfer for inhomogeneous atmospheres: RRTM, a validated correlated-k model for the longwave. **Journal of Geophysical Research: Atmospheres**, American Geophysical Union (AGU), v. 102, n. D14, p. 16663–16682, jul. 1997. Available at: https://doi.org/10.1029/97jd00237.

MO, K. C.; KOUSKY, V. E. Further analysis of the relationship between circulation anomaly patterns and tropical convection. **Journal of Geophysical Research:**

**Atmospheres**, American Geophysical Union (AGU), v. 98, n. D3, p. 5103–5113, mar. 1993. Available at: https://doi.org/10.1029/92jd02952.

MONCRIEFF, M. W. *et al.* Multiscale convective organization and the YOTC virtual global field campaign. **Bulletin of the American Meteorological Society**, American Meteorological Society, v. 93, n. 8, p. 1171–1187, aug 2012.

MORRISON, H. Modeling clouds observed at SHEBA using a bulk microphysics parameterization implemented into a single-column model. **Journal of Geophysical Research**, American Geophysical Union (AGU), v. 108, n. D8, 2003. Available at: https://doi.org/10.1029/2002jd002229.

MORRISON, H.; CURRY, J. A.; KHVOROSTYANOV, V. I. A new double-moment microphysics parameterization for application in cloud and climate models. part i: Description. **Journal of the Atmospheric Sciences**, American Meteorological Society, v. 62, n. 6, p. 1665–1677, jun. 2005. Available at: https://doi.org/10.1175/jas3446.1.

MORRISON, H.; MILBRANDT, J. A. Parameterization of cloud microphysics based on the prediction of bulk ice particle properties. part i: Scheme description and idealized tests. **Journal of the Atmospheric Sciences**, American Meteorological Society, v. 72, n. 1, p. 287–311, jan. 2015. Available at: https://doi.org/10.1175/jas-d-14-0065.1.

NEGRI, A. J. A TRMM-calibrated infrared rainfall algorithm applied over brazil. **Journal of Geophysical Research**, American Geophysical Union (AGU), v. 107, n. D20, 2002. Available at: https://doi.org/10.1029/2000jd000265.

NEWMAN, M. *et al.* The pacific decadal oscillation, revisited. **Journal of Climate**, American Meteorological Society, v. 29, n. 12, p. 4399–4427, jun. 2016. Available at: https://doi.org/10.1175/jcli-d-15-0508.1.

NOAA National Centers for Environmental Information. **ETOPO 2022 15 Arc-Second Global Relief Model**. NOAA National Centers for Environmental Information, 2022. Available at: https://data.noaa.gov/metaview/page?xml=NOAA/NESDIS/NGDC/MGG/DEM//iso/xml/etopo_2022.xml&view=getDataView&header=none.

NOBRE, C. A.; MARENGO, J. A.; ARTAXO, P. Understanding the climate of Amazonia: Progress from LBA. **Washington DC American Geophysical Union Geophysical Monograph Series**, v. 186, p. 145–147, jan. 2009.

NOBRE, C. A. *et al.* Characteristics of amazonian climate: Main features. *In*: ______. **Amazonia and Global Change**. American Geophysical Union (AGU), 2009. p. 149–162. ISBN 9781118670347. Available at: https://agupubs.onlinelibrary.wiley.com/doi/abs/10.1029/2009GM000903.

RANDALL, D. A. *et al.* Single-column models and cloud ensemble models as links between observations and climate models. **Journal of Climate**, American Meteorological Society, v. 9, n. 8, p. 1683–1697, ago. 1996. Available at: https://doi.org/10.1175/1520-0442(1996)009<1683:scmace>2.0.co;2.

RAO, V. B.; CAVALCANTI, I. F.; HADA, K. Annual variation of rainfall over brazil and water vapor characteristics over south america. **Journal of Geophysical Research: Atmospheres**, Wiley Online Library, v. 101, n. D21, p. 26539–26551, 1996.

REDDINGTON, C. L. *et al.* Air quality and human health improvements from reductions in deforestation-related fire in brazil. **Nat. Geosci.**, Springer Science and Business Media LLC, v. 8, n. 10, p. 768–771, out. 2015.

RICKENBACH, T. M. Modulation of convection in the southwestern amazon basin by extratropical stationary fronts. **Journal of Geophysical Research**, American Geophysical Union (AGU), v. 107, n. D20, 2002.

RODELL, M. *et al.* The global land data assimilation system. **Bulletin of the American Meteorological Society**, American Meteorological Society, v. 85, n. 3, p. 381–394, mar. 2004. Available at: https://doi.org/10.1175/bams-85-3-381.

SAATCHI, S. S. *et al.* Benchmark map of forest carbon stocks in tropical regions across three continents. **Proceedings of the National Academy of Sciences**, Proceedings of the National Academy of Sciences, v. 108, n. 24, p. 9899–9904, maio 2011. Available at: https://doi.org/10.1073/pnas.1019576108.

SALATI, E. *et al.* Recycling of water in the amazon basin: An isotopic study. **Water Resources Research**, American Geophysical Union (AGU), v. 15, n. 5, p. 1250–1258, out. 1979. Available at: https://doi.org/10.1029/wr015i005p01250.

SCHAEFER, C. *et al.* Solos da região amazônica. *In*: _____. [*S.l.: s.n.*], 2017. p. 111–176. ISBN 9788586504228.

SCHIRO, K. A. *et al.* GoAmazon2014/5 campaign points to deep-inflow approach to deep convection across scales. **Proceedings of the National Academy of Sciences**, Proceedings of the National Academy of Sciences, v. 115, n. 18, p. 4577–4582, abr. 2018. Available at: https://doi.org/10.1073/pnas.1719842115.

SCHIRO, K. A. *et al.* Deep convection and column water vapor over tropical land versus tropical ocean: A comparison between the amazon and the tropical western pacific. **Journal of the Atmospheric Sciences**, American Meteorological Society, v. 73, n. 10, p. 4043–4063, oct 2016.

SCHUMACHER, C.; FUNK, A. **GoAmazon2014/5 Rain Rates from the SIPAM Manaus S-band Radar**. Atmospheric Radiation Measurement (ARM) Archive, Oak Ridge National Laboratory (ORNL), Oak Ridge, TN (US), 2018. Available at: https://www.osti.gov/servlets/purl/1459578/.

SCHUMACHER, C.; FUNK, A. **GoAmazon2014/5 Three-dimensional Gridded S-band Reflectivity and Radial Velocity from the SIPAM Manaus S-band Radar**. Atmospheric Radiation Measurement (ARM) Archive, Oak Ridge National Laboratory (ORNL), Oak Ridge, TN (US), 2018. Available at: https://www.osti.gov/servlets/purl/1459573/.

SENA, E. T.; ARTAXO, P.; CORREIA, A. L. Spatial variability of the direct radiative forcing of biomass burning aerosols and the effects of land use change in amazonia. **Atmos. Chem. Phys.**, Copernicus GmbH, v. 13, n. 3, p. 1261–1275, fev. 2013.

SHERWOOD, S. C.; BONY, S.; DUFRESNE, J.-L. Spread in model climate sensitivity traced to atmospheric convective mixing. **Nature**, Springer Science and Business Media LLC, v. 505, n. 7481, p. 37–42, jan. 2014. Available at: https://doi.org/10.1038/nature12829.

SILVA DIAS, M. A. F. *et al.* **LBA-ECO CD-01 Meteorological Data, Tapajos and Amazon Rivers, Santarem, Brazil: 2001**. ORNL Distributed Active Archive Center, 2012. Available at: http://daac.ornl.gov/cgi-bin/dsviewer.pl?ds_id=1114.

SILVA DIAS, M. A. F. *et al.* River breeze circulation in eastern amazonia: observations and modelling results. **Theoretical and Applied Climatology**, Springer Science and Business Media LLC, v. 78, n. 1-3, abr. 2004. Available at: https://doi.org/10.1007/s00704-004-0047-6.

SILVA DIAS, M. A. F. *et al.* Cloud and rain processes in a biosphere-atmosphere interaction context in the amazon region. **Journal of Geophysical Research: Atmospheres**, v. 107, n. D20, p. LBA 39–1–LBA 39–18, 2002. Available at: https://agupubs.onlinelibrary.wiley.com/doi/abs/10.1029/2001JD000335.

SILVA, R. R. da *et al.* Cloud streets and land–water interactions in the amazon. **Biogeochemistry**, Springer Science and Business Media LLC, v. 105, n. 1-3, p. 201–211, apr 2011.

SØRENSEN, J. H. *et al.* Mesoscale influence on long-range transport — evidence from ETEX modelling and observations. **Atmos. Environ. (1994)**, Elsevier BV, v. 32, n. 24, p. 4207–4217, dez. 1998.

STEEGE, H. ter *et al.* Hyperdominance in the amazonian tree flora. **Science**, American Association for the Advancement of Science (AAAS), v. 342, n. 6156, p. 1243092–1243092, out. 2013. Available at: https://doi.org/10.1126/science.1243092.

STEVENS, B.; BONY, S. What are climate models missing? **Science**, American Association for the Advancement of Science (AAAS), v. 340, n. 6136, p. 1053–1054, maio 2013. Available at: https://doi.org/10.1126/science.1237554.

STULL, R. **Practical Meteorology: An Algebra-based Survey of Atmospheric Science**. AVP International, University of British Columbia, 2016. (BC Open Textbook Collection). ISBN 9780888651761. Available at: https://books.google.com.br/books?id=xP2sDAEACAAJ.

TANG, S. *et al.* Large-scale vertical velocity, diabatic heating and drying profiles associated with seasonal and diurnal variations of convective systems observed in the GoAmazon2014/5 experiment. **Atmospheric Chemistry and Physics**, Copernicus GmbH, v. 16, n. 22, p. 14249–14264, nov. 2016. Available at: https://doi.org/10.5194/acp-16-14249-2016.

TIAN, Y. *et al.* Interpreting the diurnal cycle of clouds and precipitation in the arm goamazon observations: Shallow to deep convection transition. **Journal of Geophysical Research: Atmospheres**, Wiley Online Library, v. 126, n. 5, p. e2020JD033766, 2021.

TORRI, G.; KUANG, Z.; TIAN, Y. Mechanisms for convection triggering by cold pools. **Geophysical Research Letters**, American Geophysical Union (AGU), v. 42, n. 6, p. 1943–1950, mar 2015.

TOTA, J. *et al.* Análise da variabilidade diária da precipitação em área de pastagem para a época chuvosa de 1999 - projeto TRMM/LBA. **Acta Amazonica**, FapUNIFESP (SciELO), v. 30, n. 4, p. 629–629, dez. 2000. Available at: https://doi.org/10.1590/1809-43922000304639.

WAITE, M. L.; KHOUIDER, B. The deepening of tropical convection by congestus preconditioning. **Journal of the Atmospheric Sciences**, American Meteorological Society, v. 67, n. 8, p. 2601–2615, aug 2010.

WALLACE, J. M.; HOBBS, P. V. **Atmospheric science : an introductory survey**. Amsterdam Boston: Elsevier Academic Press, 2006. ISBN 978-0127329512.

WENG, W. *et al.* Aerial and surface rivers: downwind impacts on water availability from land use changes in amazonia. Copernicus GmbH, set. 2017. Available at: https://doi.org/10.5194/hess-2017-526.

WU, C.-M.; STEVENS, B.; ARAKAWA, A. What controls the transition from shallow to deep convection? **Journal of the Atmospheric Sciences**, American Meteorological Society, Boston MA, USA, v. 66, n. 6, p. 1793 – 1806, 01 Jun. 2009. Available at: https://journals.ametsoc.org/view/journals/atsc/66/6/2008jas2945.1.xml.

YEO, K.; ROMPS, D. M. Measurement of convective entrainment using lagrangian particles. **Journal of the Atmospheric Sciences**, American Meteorological Society, Boston MA, USA, v. 70, n. 1, p. 266 – 277, 2013. Available at: https://journals.ametsoc.org/view/journals/atsc/70/1/jas-d-12-0144.1.xml.

ZENG, X. The relationship among precipitation, cloud-top temperature, and precipitable water over the tropics. **Journal of Climate**, American Meteorological Society, v. 12, n. 8, p. 2503–2514, ago. 1999. Available at: https://doi.org/10.1175/1520-0442(1999)012<2503:trapct>2.0.co;2.

ZHANG, C. *et al.* Cracking the MJO nut. **Geophysical Research Letters**, American Geophysical Union (AGU), v. 40, n. 6, p. 1223–1230, mar 2013.

ZHANG, M. H.; LIN, J. L. Constrained variational analysis of sounding data based on column-integrated budgets of mass, heat, moisture, and momentum: Approach and application to ARM measurements. **Journal of the Atmospheric Sciences**, American Meteorological Society, v. 54, n. 11, p. 1503–1524, jun. 1997. Available at: https://doi.org/10.1175/1520-0469(1997)054<1503:cvaosd>2.0.co;2.

ZHANG, M. H. *et al.* Objective analysis of ARM IOP data: Method and sensitivity. **Monthly Weather Review**, American Meteorological Society, v. 129, n. 2, p. 295–311, fev. 2001. Available at: https://doi.org/10.1175/1520-0493(2001)129<0295:oaoaid>2.0.co;2.

ZHUANG, Y. *et al.* Seasonal variation of shallow-to-deep convection transition and its link to the environmental conditions over the central amazon. **Journal of Geophysical Research: Atmospheres**, American Geophysical Union (AGU), v. 122, n. 5, p. 2649–2666, mar 2017.

# APPENDIX

# APPENDIX A – SUPPLEMENTARY RESULTS ON CONVECTIVE INDICES

Since the magnitude of convective indices depends on the idealization of the rising parcels, this Appendix is intended to provide supplemental results supporting our observational study of the boundary layer properties (section 5.3.3). Specifically, we show the results for the comparison of PBL, LCL, and LFC heights, where LCL and LFC are calculated using the most unstable parcel (Figure A.1), 50-hPa mixed-layer parcel (Figure A.2), 25-hPa mixed-layer parcel (Figure A.3), and 10-hPa mixed-layer parcel (Figure A.4). Furthermore, we also show results for CIN, CAPE, and $-\Delta$CAPE determined using the most unstable parcel (Figure A.5), 50-hPa mixed-layer parcel (Figure A.6), 25-hPa mixed-layer parcel (Figure A.7), and 10-hPa mixed-layer parcel (Figure A.8).

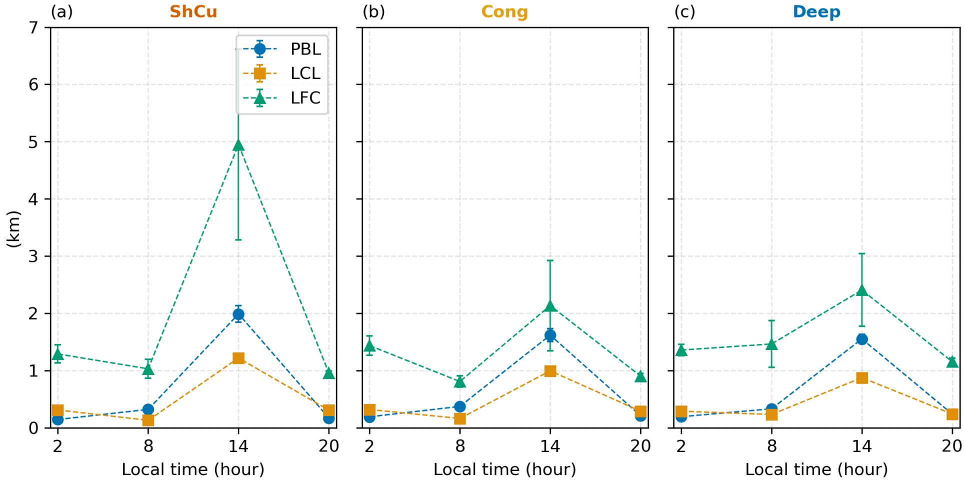

Figure A.1 – Comparison of PBL, LCL, and LFC heights for (a) ShCu regime, (b) Cong regime, and (c) Deep regime. LCL and LFC are determined using the most unstable parcel.

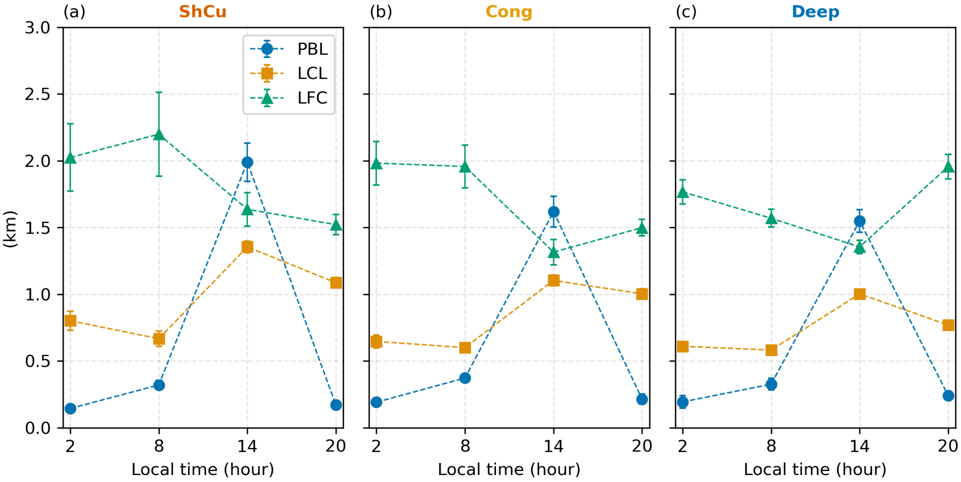

Figure A.2 – Comparison of PBL, LCL, and LFC heights for (a) ShCu regime, (b) Cong regime, and (c) Deep regime. LCL and LFC are determined using the 50-hPa mixed-layer parcel.

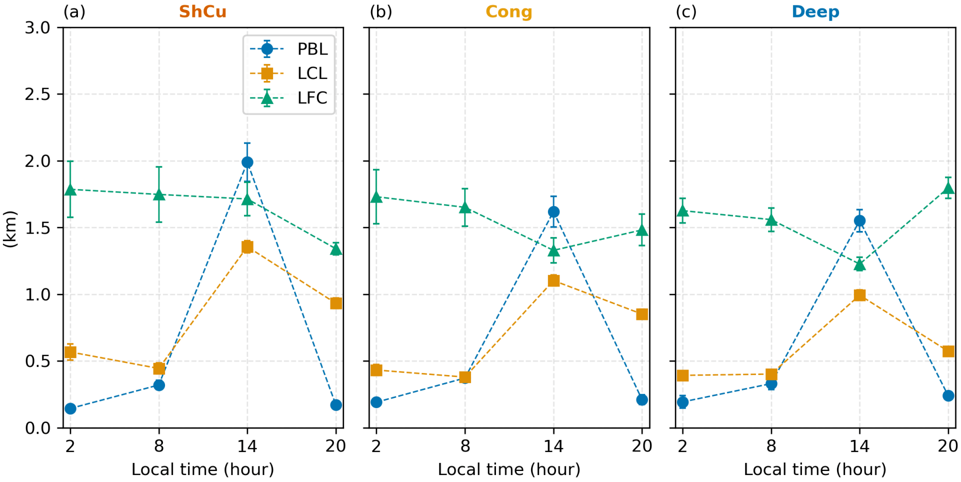

Figure A.3 – Comparison of PBL, LCL, and LFC heights for (a) ShCu regime, (b) Cong regime, and (c) Deep regime. LCL and LFC are determined using the 25-hPa mixed-layer parcel.

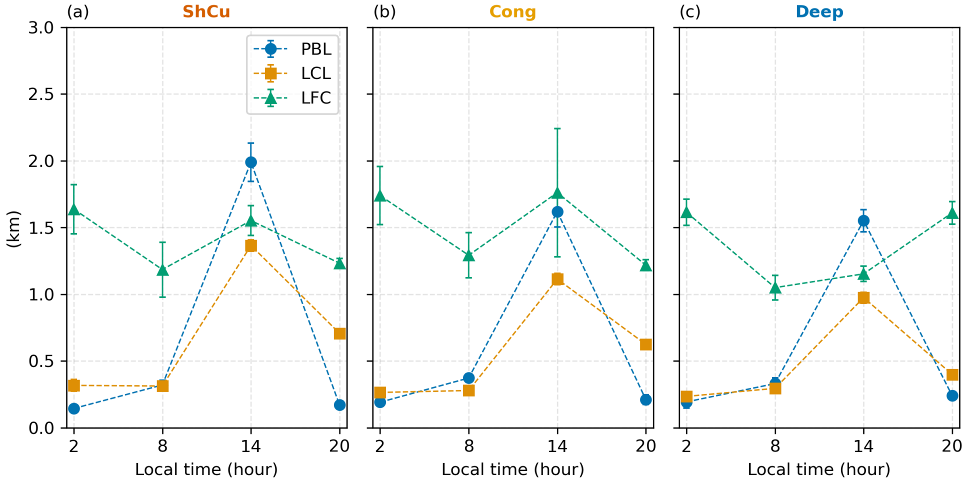

Figure A.4 – Comparison of PBL, LCL, and LFC heights for (a) ShCu regime, (b) Cong regime, and (c) Deep regime. LCL and LFC are determined using the 10-hPa mixed-layer parcel.

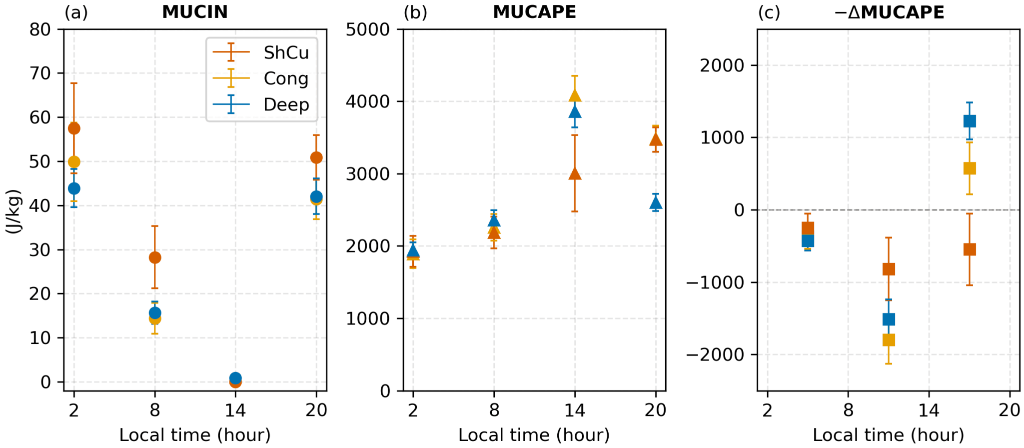

Figure A.5 – (a) most unstable (MU)CIN, (b) MUCAPE, and (c) and $-\Delta$MUCAPE. The circle marker shows MUCIN and MUCAPE available at the radiosonde launch times (02, 08, 14, and 20 LST), while the triangle marker describes $-\Delta$MUCAPE calculated as the difference in MUCAPE between two consecutive times.

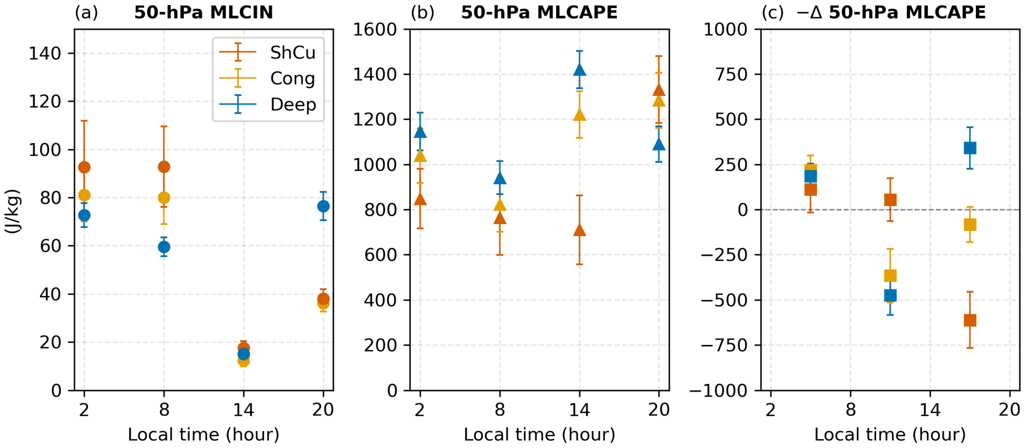

Figure A.6 – (a) 50-hPa mixed-layer MLCIN, (b) MLCAPE, and (c) and −ΔMLCAPE. The circle marker shows MLCIN and MLCAPE available at the radiosonde launch times (02, 08, 14, and 20 LST), while the triangle marker describes −ΔMLCAPE calculated as the difference in MLCAPE between two consecutive times.

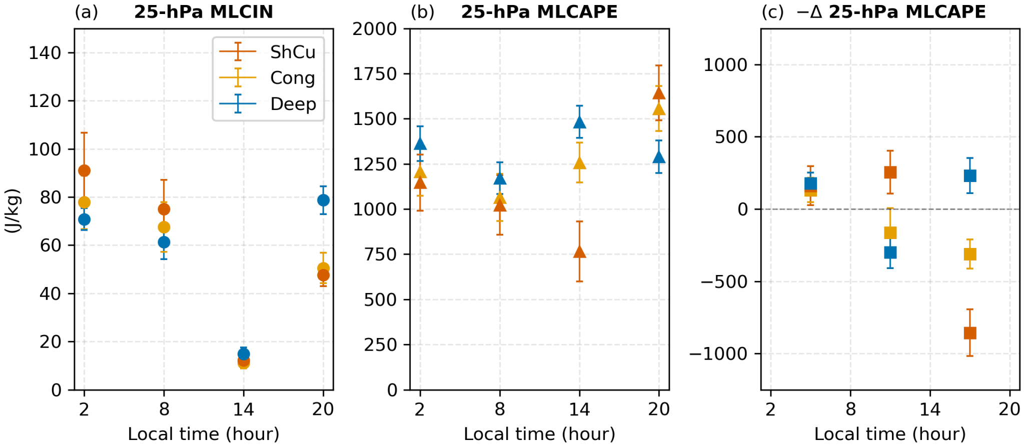

Figure A.7 – (a) 25-hPa mixed-layer (ML)CIN, (b) MLCAPE, and (c) and −ΔMLCAPE. The circle marker shows MLCIN and MLCAPE available at the radiosonde launch times (02, 08, 14, and 20 LST), while the triangle marker describes −ΔMLCAPE calculated as the difference in MLCAPE between two consecutive times.

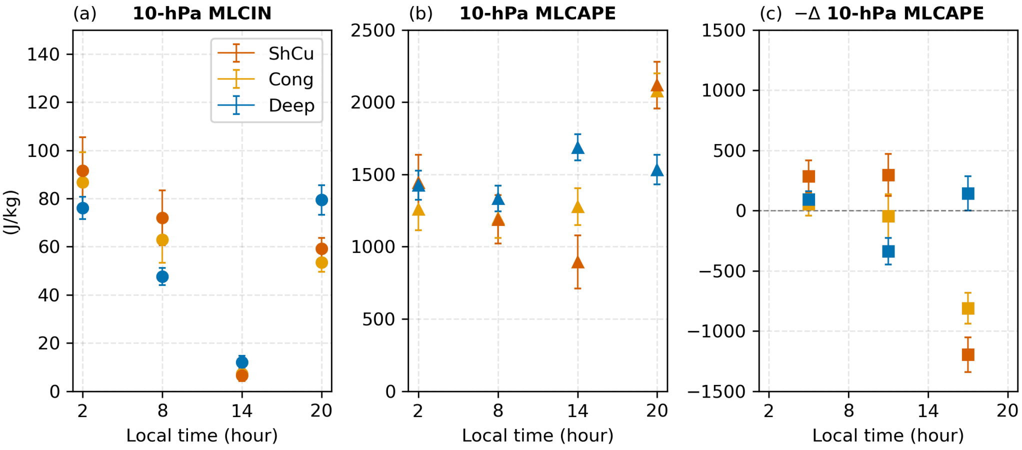

Figure A.8 – (a) 10-hPa mixed-layer (ML)CIN, (b) MLCAPE, and (c) and −ΔMLCAPE. The circle marker shows MLCIN and MLCAPE available at the radiosonde launch times (02, 08, 14, and 20 LST), while the triangle marker describes −ΔMLCAPE calculated as the difference in MLCAPE between two consecutive times.

# APPENDIX B – PRESENTATIONS AT SCIENTIFIC EVENTS

List of presentations at national and international scientific events:

1. VISCARDI, L. A. M.; TORRI, G.; ADAMS, D. K.; BARBOSA, H. M. J. *Observation of the diurnal cycles of shallow, congestus, and deep convective days in the Amazonian wet season*. In: AMS 103rd Annual Meeting - Third Symposium on Mesoscale Processes, Denver, USA (attended virtually), 2023.
2. VISCARDI, L. A. M.; TORRI, G.; ADAMS, D. K.; BARBOSA, H. M. J. *Observation of the diurnal cycles of shallow, congestus, and deep convective days in the Amazonian wet season*. In: AMS 103rd Annual Meeting - 22nd Annual Student Conference, Denver, USA (attended virtually), 2023.
3. VISCARDI, L. A. M.; BARBOSA, H. M. J. *Identification of convective regime in the Amazon rainforest using a combination of remote sensors*. In: XI Workshop on Lidar Measurements in Latin America - Remote sensing of clouds, Punta Arenas, Chile (attended virtually), 2021.
4. VISCARDI, L. A. M.; BARBOSA, H. M. J. *Transition of shallow to deep convection in the Amazon*. In: ATTO Meeting 2021, Manaus, Brazil (attended virtually), 2021.
5. BARBOSA, H. M. J. ; VISCARDI, L. A. M. *Observation of the Shallow-to-Deep Convection Transition in Amazonia*. In: International Conference on Clouds and Precipitation, Pune, India (attended virtually), 2021.
6. VISCARDI, L. A. M.; BARBOSA, H. M. J. *Transition of shallow to deep convection in the Amazon: a cloud resolving modeling study*. In: Land-Atmosphere Interactions 2021 Workshop, California, USA (attended virtually), 2021.